DESIGN, FABRICATION, AND OPTICAL ANALYSIS OF NANOMIRRORS FOR MASKLESS EUV LITHOGRAPHY

by

Yashesh Ajitbhai Shroff

Memorandum No. UCB/ERL M04/32

19 December 2003

DESIGN, FABRICATION, AND OPTICAL ANALYSIS OF NANOMIRRORS FOR MASKLESS EUV LITHOGRAPHY

by

Yashesh Ajitbhai Shroff

Memorandum No. UCB/ERL M04/32

19 December 2003

ELECTRONICS RESEARCH LABORATORY

College of Engineering
University of California, Berkeley
94720

Design, fabrication, and optical analysis of nanomirrors for maskless EUV lithography

by

Yashesh Ajitbhai Shroff

B.Sc. (University of Texas at Austin) 1997
M.Sc. (University of California, Berkeley) 1999

A dissertation submitted in partial satisfaction of the
requirements for the degree of

Doctor of Philosophy

in

Engineering - Electrical Engineering and Computer Sciences

in the

GRADUATE DIVISION

of the

UNIVERSITY OF CALIFORNIA, BERKELEY

Committee in charge:

Professor William G. Oldham, Chair
Professor Borivoje Nikolić
Professor Luke Lee

Fall 2003

The dissertation of Yashesh Ajitbhai Shroff is approved:

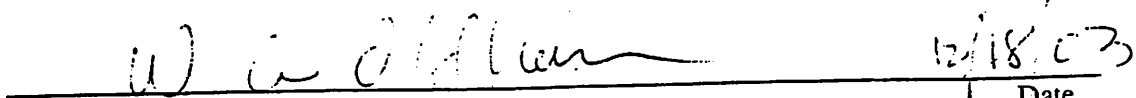

Chair 12/18/03
Date

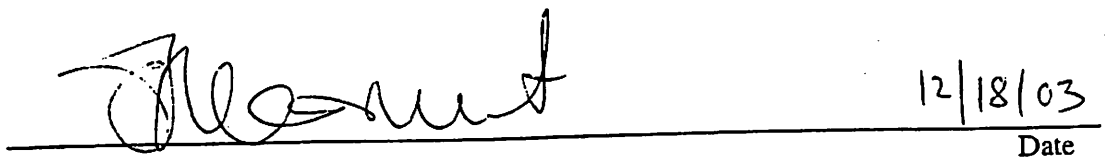

12/18/03
Date

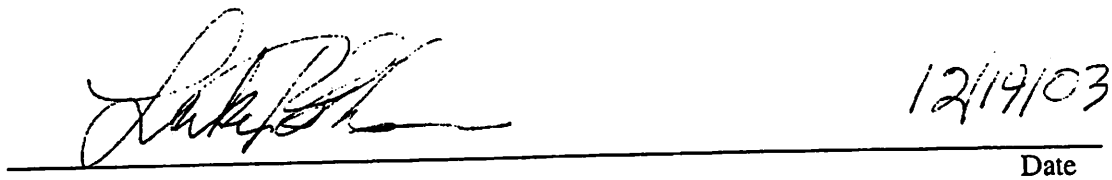

12/19/03
Date

University of California, Berkeley
Fall 2003

Abstract

Design, fabrication, and optical analysis of nanomirror for maskless EUV lithography

by

Yashesh Ajitbhai Shroff

Doctor of Philosophy in Engineering – Department of EECS

University of California at Berkeley

Professor William G. Oldham, Chair

This thesis explores the feasibility of substituting an array of modulatable mirrors for mask in optical lithography. We have concentrated particularly on EUV wavelengths and thus the use of very small mirrors, from 1 to several micrometers on an edge. Both tilting and piston motion has been studied as a means of modulation. We have fabricated arrays of mirrors 3-5um on an edge and <300nm gap. The structural material is amorphous-SiGe with ~55% Ge content allowing it to be conductive in a low thermal budget. The sacrificial layer is Ge. Highest temperature seen by the devices is 450deg C making the mirror array compatible with future integration with logic and memory on the same die.

Mirror based pattern generation is studied to provide an understanding of how they can be operated in an analog mode to meet the quasi-continuous sizing and placement requirements of optical lithography. A general model using only three parameters, light coherence, #spots/minimum feature, and k1 resolution parameter is developed to

understand parameter heavy nanomirror imaging. While a single mirror 'spot' is designed to not resolve, two or more spots with an optical path difference (*OPD*) between 0 and ½ lambda are shown to generate grayscaled patterns.

Normalized image log slope (NILS) of piston mirror edges is higher than tilt and marginally lower than attenuated PSM. Overtilted (*OPD*>1/2 lambda) mirrors and pseudo-tilt (aka double-piston) mirrors perform better than piston mirrors for isolated spaces. For isolated lines, attenuated PSM is marginally better than tilt and piston mirrors. Off-grid slope degradation is observed for both modulation schemes. Defocus related image shift is observed and attributed to asymmetric wavefront reflected from mirrors. Image shift, which can be a serious concern in optical lithography, is more prominent in piston than tilt mirrors. A 'double-piston' mirror design is proposed which reduces shift to tilting mirror level and also provides the large process-window of piston mirrors.

Under low k1 conditions (in which sub resolution features are added to conventional mask patterns to acheive "optical proximity correction") it is possible to perform an analogous OPC by adjusting the tilts of all the mirrors in the vicinity of the densely patterned region. In other words the image is optimized for some property, for example to achieve the target critical dimension at one or more points along a line. A simple optimization algorithm is been demonstrated based on the Newton-Raphson method. Aerial image of off-grid, minimum sized, orthogonal, and densely packed features with up to 7 target critical points is placed within CD/60 tolerance.

Normalized image log slope (NILS) of piston mirror edges is higher than tilt and marginally lower than attenuated PSM. Overtilted (*OPD*>1/2 lambda) mirrors and pseudo-tilt (aka double-piston) mirrors perform better than piston mirrors for isolated spaces. For isolated lines, attenuated PSM is marginally better than tilt and piston mirrors. Off-grid slope degradation is observed for both modulation schemes. Defocus related image shift is observed and attributed to asymmetric wavefront reflected from mirrors. Image shift, which can be a serious concern in optical lithography, is more prominent in piston than tilt mirrors. A 'double-piston' mirror design is proposed which reduces shift to tilting mirror level and also provides the large process-window of piston mirrors.

Under low k1 conditions (in which sub resolution features are added to conventional mask patterns to acheive "optical proximity correction") it is possible to perform an analogous OPC by adjusting the tilts of all the mirrors in the vicinity of the densely patterned region. In other words the image is optimized for some property, for example to achieve the target critical dimension at one or more points along a line. A simple optimization algorithm is been demonstrated based on the Newton-Raphson method. Aerial image of off-grid, minimum sized, orthogonal, and densely packed features with up to 7 target critical points is placed within CD/60 tolerance.

Prof. William G. Oldham

To my parents

Table of contents

List of figures

Chapter 1

Chapter 2

Chapter 3

Chapter 4

Chapter 5

List of tables

Acknowledgements

I would like to express my sincerest appreciation to my advisor, Prof. William G. Oldham. He gave me latitude in learning all I could at this great institute of knowledge. He guided me with patience. He taught me *science*. He carefully reviewed my write-ups, including this thesis. He did it all.

I would like to thank Prof. Bora Nikolic and Prof. Luke Lee for reading and critiquing this work. My deep gratitude to Prof. Andy Neureuther for many helpful discussions. Thanks to Prof. Bokor who introduced me to the world of optics.

Research can often lead to long solitary journeys; however, I am glad that whenever I have had a difficult problem, the great knowledge-base of Berkeley and EECS in particular has come to my rescue. In that vein, I would like to thank Fan Piao, Kostas Adam, Junwei Bao, Andrea Franke, and Ebo Croffe for many insightful discussions. In particular, I would like to thank Yijian Chen and Vito Dai for their shared enthusiasm (and frustrations!) during this "maskless" journey.

The Microlab has been instrumental in the experimental portion of this work. I would like to thank the Microlab staff, particularly Xiao Fan Meng for AFM measurements and Jimmy Chang for process flow related help.

I have made friends out of colleagues working in this group. I would like to thank Mike Shumway, Mike Williamson, Lei Yuan, Garth Robins, Frank Genneri, Scott, Yunfei Deng, Yan Weng, Greg McIntyre, and Mike Lam for enriching my grad school

experience. Thanks to Vivian Kim for keeping us on our toes with deadlines and being flexible all the same.

For the many laughs and short and long hikes on the Berkeley hills, thanks to Hitesh Barot. Thanks to Lilian for giving me a quiet home for many years. I have made great friends over the years - Ankur, Rahul, Gaurav (1&2), Abhay, Manu, Parag, and Sanjeev, Sudip, Riddhi, Sarju, and Rakhi. Thanks, folks! Without you my life would have been colorless.

I conclude with an expression of appreciation to my family. Without their love, sacrifice, and motivation, this thesis would not have been possible. Thanks to the parents, Arpita, Mona, and Unmeshbhai for all your support.

This research has been jointly sponsored by the Semiconductor Research Corporation and DARPA.

1 Introduction

1.1 Background

Major device manufacturers have geared extensive resources in the search of a next-generation lithography (NGL) technology that would enable smooth scaling of minimum feature size down-to and beyond 100nm critical dimension (CD) printing capability. Whether it is deep UV or extreme-UV (EUV) lithography, masks are the common denominator. However, it is increasingly believed that masks are a cumbersome part of the lithography system and it is much more desirable to have a maskless lithography system. The purpose of this research is to explore some of the critical problems facing maskless lithography. A brief overview of existing light modulation technologies is presented to establish the current state of mirror based light modulator fabrication. The apparent advantages of mirror based pattern generation are explored vis-à-vis existing mask based approach with an accompanying overview of optical lithography. This chapter concludes with a presentation of a schematic diagram of a conceptual maskless optical projection system and a content layout of topics dealt with in the subsequent chapters.

1.2 Optical MEMS based pattern generation

New and novel uses of microelectromechanical system (MEMS) based light modulators continue to appear since the early days of silicon micromachining. From analysing DNA

for gene sequencing to reducing atmospheric aberrations in telescopes gazing at far away galaxies, micromirrors have found many ways to keep the MEMS community occupied. Silicon light modulators can be of several types based on the mode of operation, such as elastomer, membranes, or cantilever. Figure 1-0 shows examples of micromirrors used for visible wavelength based display devices. Use of micromirrors for pattern generation is similar in concept to the deformable-mirror devices (DMD) of Texas Instruments (TI) which have an array of individually controlled mirrors (16μm on the side) that twist on a torsion bar, thus selectively deflecting light and creating a pattern on a view-screen [1,2]. The electrostatically actuated TI DMD array is built on top of a static random-access memory (SRAM) bank. The DMD process involves fabricating a superstructure consisting of electrode, spacer, hinge, and a beam on top of the SRAM array. Each pixel contains one transistor that acts as a swtich to sample and store the analog voltage from the line-address circuitry onto the pixel address electrode. For row/column addressing, all gates in a row are connected. Similarly, all drains in a column are connected and driven by a serial to parallel converter and by a drain driver amplifier. This is similar to the way DRAM logic is arranged.

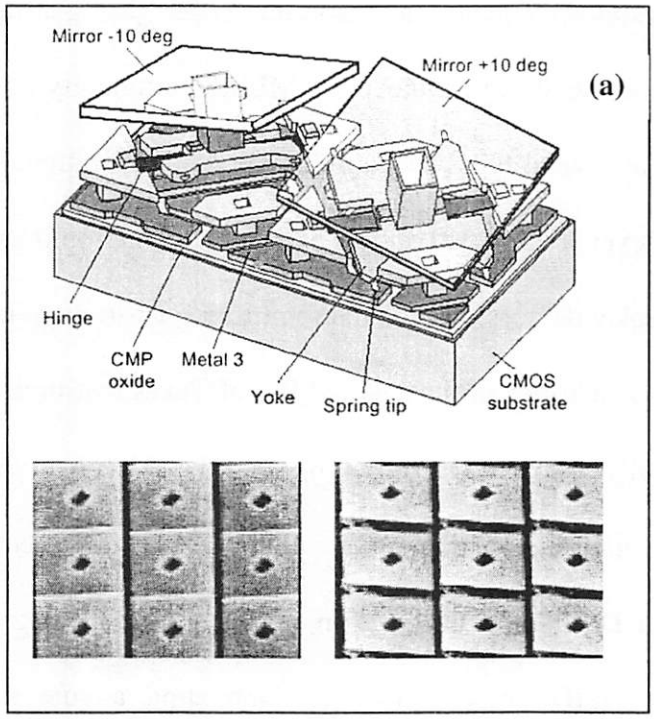

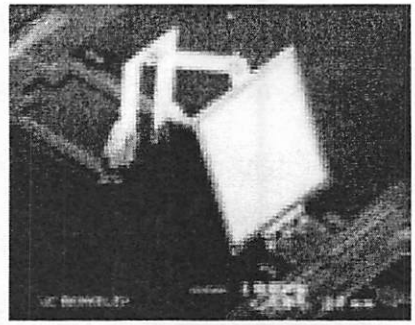

Figure 1-0: (a) Schematic diagram of Texas-Instrument's DMD with a view of a built-in SRAM underneath. SEM of an array of tilted mirrors is also shown [1]; (b) Fast and slow scanning mirrors for eye-glass micro-projector from Prof. Kam Lau's group at UC Berkeley [9].

Another mode of optical beam deflection with electrostatically driven MEMS mirrors is the grating light valve based silicon light modulator that depends on pure phase modulation. Piston like motion can be obtained, for instance, by having deformable viscoelastic layers [7] or with symmetrically arranged cantilever hinges that bend when an underlying address electrode is energized [4]. Unlike the torsional mirrors, in the pure-phase mode of operation, image formation occurs due to interference among several mirrors. Pattern fidelity of pure-phase modulation (due to piston like motion) and amplitude-phase modulation (as with the tilting mirrors) is discussed in at length in later chapters.

In the area of telecommunications, micromirrors play an increasingly prominent role due to the fact that they provide significant increase in bandwidth by allowing optical

switching. Companies like Lucent and Onyx have built large arrays of micromirrors but this is also an example where economic considerations have overtaken technological breakthroughs to slow down optical switching implementation in the wake of telecommunication industry's precipitous fall in 2000. In the area of astronomy, Sandia National Labs is building a large telescope that will involve millions of micromirrors collectively acting as a lens. The idea is that wavefront aberrations due to atmospheric changes can be quickly corrected with the individually addressable mirrors to get images nearly as good as ones obtained using space-based telescopes. At the other end of the spectrum is the fabrication and use of hexagonal micromirrors for identifying and correcting aberrations in the pupil of the eye.

Micromirrors can be differentiated using several criteria such as the number of mirrors in the array, size of the mirror itself, and its operating frequency. Conceptually, for pattern generation, all the work can be done by a single mirror, however, that does not allow for redundancy, nor does it effectively utilize silicon micromaching batch processing capability. High resonant frequency is generally good and mirror size mostly depends on the application at hand.

The effect of gap between mirrors is dependent on the projection system numerical aperture, light source coherence, and number of mirror elements used to create a minimum sized feature. A good mirror design tries to minimize the "dark" or non-reflective area of the mirror cell for high image fidelity. The optically active area in a mirror cell, also known as the *fill-factor*, of a continuous viscoelastic design is 100%

since there is a closed mirror layer for all the devices. The TI-DMD torsional mirror example above achieves a fill-factor slightly higher than 90%.

1.3 Optical lithography evolution

Over the last few years, research in EUVL has shown great promise and is a leading contender to be an NGL approach. While "conventional" optical systems employ refractive lenses, EUVL cannot do so because most materials absorb EUV wavelength light almost completely. A multi-layer stack composed of around 40 bi-layers of Si/Mo provides peak reflectivity of about 70% at λ=13.4nm wavelength light. Each layer has an approximate thickness of λ/4and is deposited using sputtering [5]. The top surface of an EUV mask is coated with an absorbing material to form a pattern. Rather than using absorbers to create dark and bright areas in the image, selected mirrors can be modulated using on-chip electronics. The pattern is demagnified and focused on the wafer to expose photo-resist as shown in Figure 1-1.

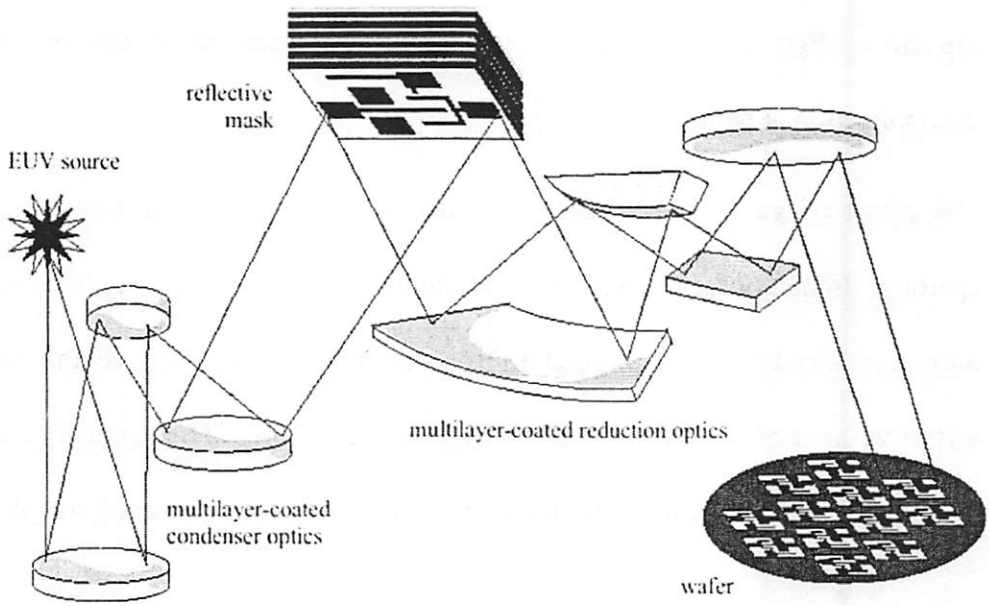

Figure 1-1: Schematic diagram of a reflective projection optical lithgraphy system based on EUV (13.4nm) wavelength illumination.

Resolution: Minimum feature size depends on the numerical aperture, *NA*, of the lens and the actinic wavelength, λ. It is described by the simple relationship:

$$S = k1 * l/NA \qquad \textit{Eq. 1-1}$$

where *S* is the minimum resolvable half-pitch, and k is an empirical constant in the range of 0.5 to 1.0 for EUVL [6]. The shorter wavelength of EUVL allows the fabrication of devices with much smaller feature size than feasible with deep-UV wavelength light source.

1.3.1 Issues with masks

At present, there are three critical issues facing conventional masks: cost of fabrication, pellicle (in case of EUV), and defects [3].

The mask cost of ownership (COO) continues to rise with each new technology generation. The following graph (Figure 1-) shows that EUV masks can cost anywhere between 35 to 160 thousand dollars for a *single* level. Many of the current applications require 20 to 30 masks, so the mask costs for a single application is enormous. For a typical CMOS process, this can be upwards of a million dollars for just one mask-set.

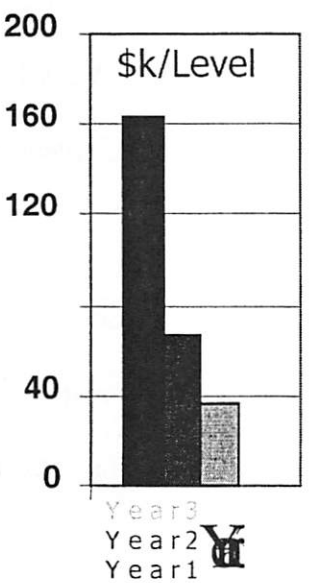

Figure 1-3: Cost of EUV reticles [8]

Secondly, there is the issue of mask handling. In order to prevent contamination of masks by unwanted particulates, a hard, yet transparent to

the actinic wavelength, pellicle is used. The idea is that if a particle falls on the mask, it will not actually deposit on the chrome but will rest a few hundred microns above the actual pattern, rendering itself out of focus. However, with EUV, it had been very difficult to find a suitably EUV transparent pellicle material. Repair of any multi-layer defect is impractical. Hence, mask-handling is very delicate.

Finally, assuring a defect-free EUV mask is a major challenge, adding to the overall cost of the system. Defects burried deep in the multi-layer are difficult to detect and harder still to correct. A robust pattern generator that has built-in redundancy can be phase and amplitude defect resistant.

Any form of a reusable mask, such as our active mirror array, can be an attractive solution to the mask problem.

1.3.2 The case for maskless lithography

A MEMS based maskless lithography system can obviate many mask related issues outlined earlier. By eliminating the need for multiple masks for each design, cost of pattern generation drops dramatically. Secondly, it can also offer some ancilliary benefits such as quick turn-around and better control over images. Any small or large design change can be relatively quickly and inexpensively accomodated. We will show in later chapter that mirrors can work as well and sometimes out perform conventional masks in terms of image fidelity.

It is possible to incorporate redundancy in the pattern generator to deal with defects. By employing many mirrors to print a spot on the wafer, each mirror is responsible for only a fraction of the total light falling on a given pixel on the wafer. As the image is

electronically scanned over the array every feature on the wafer receives multiple exposures, each exposure from different mirrors in the array. This built-in redundancy enables any defects on the array to get voted out during the scan, and therefore the defect pattern is not transferred from the mirror array to the wafer

However, we do not want to propose a system that would require overhauling the entire lithography know-how. Instead, we want to benefit from the accumulated knowledge of optical pattern generation and build on it. Unlike electron beam or ion-beam based system, the optical MEMS maskless approach is intended to be compatible with the current EUVL system to take advantage of the existing know-how in building optical scanning projection systems. The main difference is that the conventional EUVL mask is replaced with an array of individually addressable sub-micron sized mirrors.

1.4 Mirror based pattern generation

In conventional step-and-scan projection systems, both wafer and mask are scanned because of illuminator and projection optic field-size constraints. In our maskless system, the wafer is mechanically scanned while the pattern is electronically stepped across the stationary modulator array.

The schematic of a typical EUVL system using a conventional mask is shown in Figure 1-1(a). The same system is displayed in Figure 1-1(b); however, this time the mask is replaced by a light modulator mirror array consisting of millions of sub-micron sized mirrors. Both systems are based on the concept of scanning projection lithography. Light coming for a laser source goes through condenser optics and is focussed on the mask. Patterned light is reflected from the mask, as mirrors are selectively tilted "on/off". The

imaging optics demagnifies the patterned light and focuses the image on the wafer surface. Both the wafer and mask may move in opposite directions. The differential in their speed determines the degree of demagnification.

The mirror size is constrained by the critical dimension (CD) and magnification factor on the upper bound, and a practical mirror aspect ratio on the lower end.

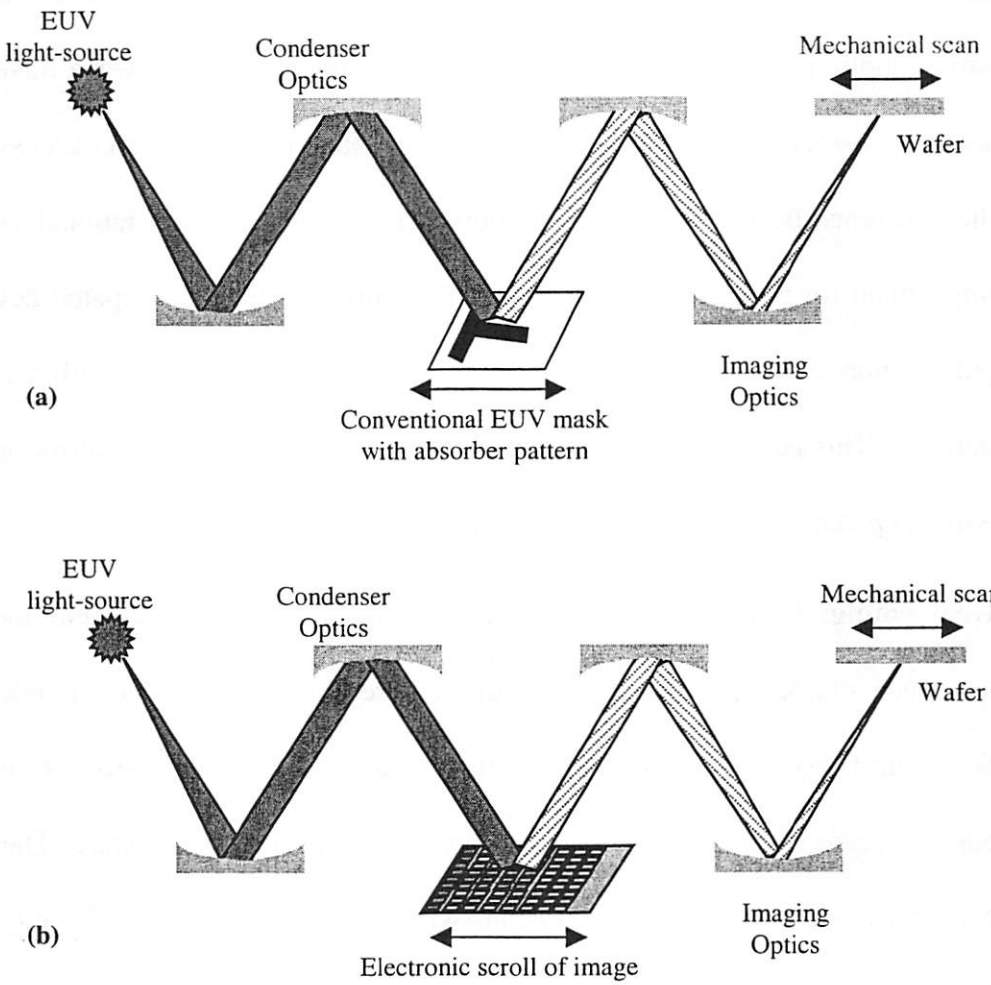

Figure 1-1: Schematic diagram of (a) conventional EUV lithography system, and (b) proposed maskless EUV lithography system. Both are based on scannning projection lithography.

1.5 Data throughput

To understand data throughput issues, it is important to realize the EUV light source contraint. High volume manufacturing makes the heavy capitol investment in technology worthwhile. To be in tune with economics of scale, next-generation EUV lithography needs to provide a throughput of 60 (300mm diameter) wafers per hour. However, the

absence of a viable high power EUV light source has proven a severe handicap in the early adoption of this technology. There is no viable continuous-wave (CW) EUV light source at present. For R&D purposes, the Advanced Light Source (ALS) synchrotron at the Lawrence-Berkeley Lab works, however, it's size and operational costs make it impractical for commercial applications. Currently, we have anticipated development of pulsed (non-CW) EUV light source that can operate up to 10kHz with a 5-10 ns pulse duration. This necessitates using a "flash" architecture wherein the mirror array is set-up with the pattern data before each short pulse of light.

Grayscaling: To accommodate fine CD adjustment and edge placement, the design grid has much smaller spots than a minimum feature. A one-to-one correspondence between design grid pixels and mirror spots vastly increases the modulator size. For instance, 1nm edge placement requires 50 mirrors to print a 50nm minimum feature. Therefore, using few spots (~2-3) per minimum feature with dose variation along the edge is a better strategy from a data point of view. If we want to adjust an edge position to a finer resolution we modulate the spot dose along that edge. The mirrors will have 5 to 6 bits of addressing to accommodate adjustment necessary for fine edge placement.

Nominal values for various parameters are used here. The idea is not to establish the precise system requirements but rather to be conservative in our estimate and provide an idea of minimum data throughput. Assuming the desired throughput is 5 wafers per hour, each wafer being 300nm in diameter, we have effectively $1cm^2$ area to write in 1 second.

Approximately two "spots" are needed to print a minimum feature size (MFS). For edge placement with MFS/50 accuracy, 5 to 6 bits ($2^5 < 50 < 2^6$) are required.

Data Throughput $= (throughput/spot\_area) * grayscaled\ bits$

$= (1cm^2/sec) / 16nm^2 * 5\text{-}bits = 1.9Tb/sec$

Alternatively, if 25nm effective spot size is used (for a 50nm node) for 60WPH, the raw data throughput to be transferred from data storage to the maskless writer chip turns out to be 9.4Tb/sec.

1.6 Thesis content layout

In the next chapter, I provide an overview of the mechanical analysis of a flexure spring based design of a parallel-plate micromirror. Issues related to architectural constraints playing into overal system design, operating frequency limits, and damping are covered.

The next chapter details fabrication of poly-silicon-germanium devices made at the UC Berekely Microlab. Release of micromirrors has been one of the most challenging aspects of this work because the inherently weak flexure (low k_{spring}) devices are susceptible to stiction. A discussion of issues particular to the fabrication process of mirrors and general issues relating to processing in the microlab form a bulk of this chapter. A complete fabrication process of the low thermal budget, low-stress, Si-Ge based micromirror devices is attached at the end of the thesis in the form of an appendix.

Chapter 4 switches gears by way of introducing the concept of pattern generation using micromirrors for the application at hand: realistic projection of layout data on the wafer. A closed form analytical understanding of image formation with mirror arrays is discussed. Pure-phase modulation based piston mirrors and amplitude-phase modulation

based tilting mirrors are studied for analog operating mode. This chapter has focus invariant study of image formation using micromirrors.

Chapter 5 develops maskless image generation further by looking at process lattitude and how various mirror technologies compare with conventional state of the art masks such as Alt. PSM and Att. PSM. Focus and dose variation, coupled with across grid printing (an issue with fixed mirrors) are used to obtain process lattitude for practical printing. Image robustness is compared across board with existing mask techniques. The way optical proximity corrections are applied to existing reticles is different from the way a maskless system would cope with proximity effects. The section on OPC presents a solution on how a mirror based system can iteratively solve for best mirror positions for high fidelity image generation.

Chapter 6 ends the work with a presentation on lessons learned, a summary of results, and a forward to many possible avenues of further research in this exciting area.

1.7 References

[1]. Larry Hornbeck, "Deformable-mirror spatial light modulators", *Proc. of SPIE,* vol. 1150, pp 86-102, 1989.

[2]. J. Younse, "Projection display systems based on the digital micromirror device (DMD)", *Proc. of SPIE,* vol. 2641, pp. 64, Austin, 1995.

[3]. Hawryluk, Sheldon, and Troccolo, "EUVL Reticle Factory Model and Reticle Cost Analysis", *Conference of OSA Trends in Optics and Photonics*, Vol. 4, page 54, 1996.

[4]. Bloom, D. M., " The Grating Light Valve: Revolutionizing Display Technology", SPIE – The International Society for Optical Engineering, 1997, Vol. 3013, page 165-171

[5]. D. Kim, H. W. Lee, et. al, "Mo-Si multi-layer as soft x-ray mirrors for the wavelengths around 20 nm region", *Journal of Vacuum Science & Technology A*, vol. 12, no. 1, Feb 1994. pp 148-52.

[6]. J. Bokor, A. Neureuther, W. Oldham, "Advanced Lithography for ULSI", *IEEE Circuits and Devices* magazine, Jan 1996, pp. 11-15.

[7]. H. Kuck, W. Doleschal, A. Gehner, et. al., "Deformable micromirror devices as phase-modulating high-resolution light valves", Sensors & Actuators A, vol. 54, pp. 536-541, 1996.

[8]. W. G. Oldham, Plenary Talk, SPIE, Santa Clara, 2000.

[9]. R. A. Conant, "A raster-scanning full-motion video display using polysilicon micromachined mirrors," Sensors & Actuators A, vol. 83, no. 1-3, 22 May 2000, pp 291-296.

2 Nanomirror light modulator array

2.1 Introduction

Nanomirror based pattern generation is feasible with the confluence of three key technologies: memory, CMOS, and electrostatic nanomirrors. A large memory bank is necessary to store the vast amount of data necessary to meet the throughput requirement. Integrated CMOS is also a must to accomplish on-chip data decompression. Finally, the nanomirror component is the "writer" portion of the chip that uses the decompressed data and converts incident light beam into a meaningful pattern at the image plane. The next section provides motivation for monolithic integration and shows one possible architecture of a pattern generator chip. We also look at an implemented example of hardware decompression. In subsequent sections, a top down design approach is used to determine the mechanical, optical, and electrostatic behavior of the nanomirror array based on high volume EUV optical projection lithography requirements.

2.2 Chip architecture

As discussed in the previous chapter, data throughput in the range of 1-10Tb/sec is necessary in order to print anywhere from 5 to 60 12" diameter wafers per hour for the 50 nm node. An architecture for delivering such a high data rate to a parallel array of mirrors can benefit from lossless compression. While not all layout layers are the same in terms

of density and repeatiblity, work done by V. Dai in Prof. Zakhor's group at UC Berkeley has shown that compression of >25 can be achieved in many cases [1]. The implementation of such a system requires the use of a fast decompression circuitry fabricated on the same chip as the mirrors, capable of decompressing around 400Gb/s of (compressed) input data into 10Tb/s stream of output data.

The basic design of a data processing system capable of delivering tera-pixel data rates necessary to achieve the required throughput for next generation maskless lithography is shown in Figure 2-0. This design consists of storage disks, a processor board with memory, and a decoder-writer chip with data-decoding circuitry fabricated together with a massive array of nanomirrors. Layout data for all the layers of a single chip are compressed off-line and stored on the disks. Before the writing process begins, only a single compressed layer is transferred from the disks to the processer board memory and stored there. As the writers write a stripe across the wafer, compressed data is streamed from the processor board to the decoder-writer chip in real-time as needed. The on-chip decoding circuitry, in real-time, expands the compressed data stream into the data signals necessary to control the writers.

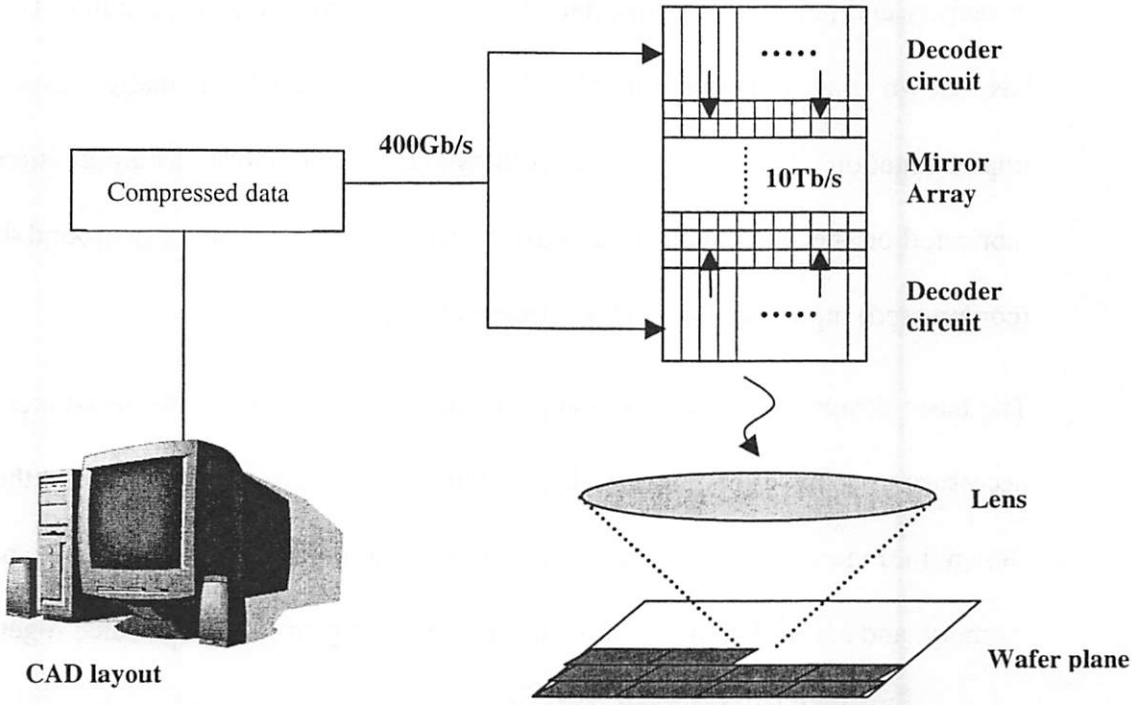

Figure 2-0: Data path to optical imaging

Handling 5-bit grayscale values requires analog control of mirror positions using analog memory. If a simple, binary interface to the writers using an SRAM array is utilized, then it is necessary to expand the grayscale data into a thermometer code, resulting in 6 times higher data throughput requirement [2].

Since the decompression algorithm is implemented in hardware some key architectural issues need to be kept in consideration. For instance, to meet the wafer throughput requirement, the decompression must be fast and the throughput constant. Because of the nature of layout data, the rate of compression may vary significantly. Therefore, the input data rate into the decoder will be variable. The output data rate will be constant.

2.2.1 Hardware decompression

Decompression represents a crucial piece of the pattern generation engine, helping gap the difference between the bandwidth required to meet the desired wafer throughput and the bandwidth available with limited throughput IC pins. Any choice of lossless compression algorithm must take into consideration that the decompression will need to be fast. The LZ77 variant of Lempel-Ziv coding scheme is a simple, yet one of the most powerful, lossless, and universal data compressor. It achieves compression by referencing sequence of source symbols to a limited memory history buffer using a pointer. In the decoding process the output rate is fixed while the input rate is variable [1].

The following exploratory work[1] shows how we can integrate decompression, memory, and pattern generation in a single module. Logic design and verification of the algorithm was done using MatLab's SIMULINK tool. Hardware design was done with ModuleCompiler. The hardware decompression path consisted of a Huffman decoder and a Lempel-Ziv decoder. A modular view of LZ77 implementation in hardware is shown in Figure 2-0. It consists of a run-length decoder and a systolic array. The run-length decoder translates the incoming bit-stream into <literal> or <offset, length> information, and uses this

[1] This study was implemented in conjuction with V. Dai and M. Freed under the guidance of Prof. Nikolić

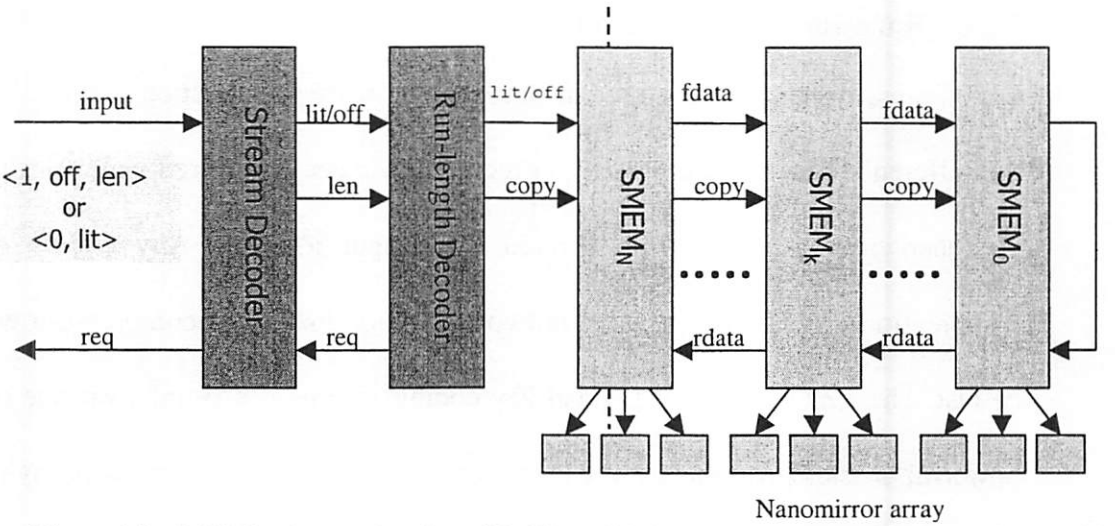

Figure 2-0: LZ77 hardware decoder with "Smart" MEMory based systolic array that could tie in directly with a nanomirror light modulator array.

information to repeat the output data as necessary. The systolic array is referred to as SMEM ("Smart"-MEMory) which can be connected directly to the nanomirror array.

To meet the throughput requirements for the application, many decompression paths must operate in parallel on the pattern generator chip. A prototype decoder chip using this decompression framework was fabricated by the Nikolić group at UC Berkeley with an SRAM array as a memory bank. The maximum throughput achieved was 32Gb/s using 8 parallel decompression paths [2]. Recent work [3] on compression has introduced better compression schemes geared specifically for layout which needs to be implemented in hardware. No one coding scheme works best for all types of layouts, therefore a combination of schemes need to be implemented for highest compression.

2.3 Nanomirror array: Design constraints

Figure 2-0 shows a conceptual view of the digital light modulator. The chip architecture has a MEMS layer on top of embedded logic. The MEMS part consists of an array of 1μm x 1μm or smaller mirrors that are fabricated on CMOS circuitry allowing selective

modulation of each mirror. The inset in Figure 2-0 shows an individual tilting mirror in detail. Mechanics of the tilting mirror operation are explained in detail in a subsequent section and its fabrication detailed in the next chapter. Electrostatic force, due to the built-in capacitor actuates the mirrors. There are several competing ideas on the type of modulation best suited for maskless lithography patterning. While this and next chapter discuss the tilting mirror approach, another interesting approach is the use of electrostatically actuated piston mirrors to provide pure phase modulation of light [10-12]. The only difference between tilting and piston mirrors is in the mode of light modulation. The other parts of the pattern generation system such as addressing and data transfer remain the same.

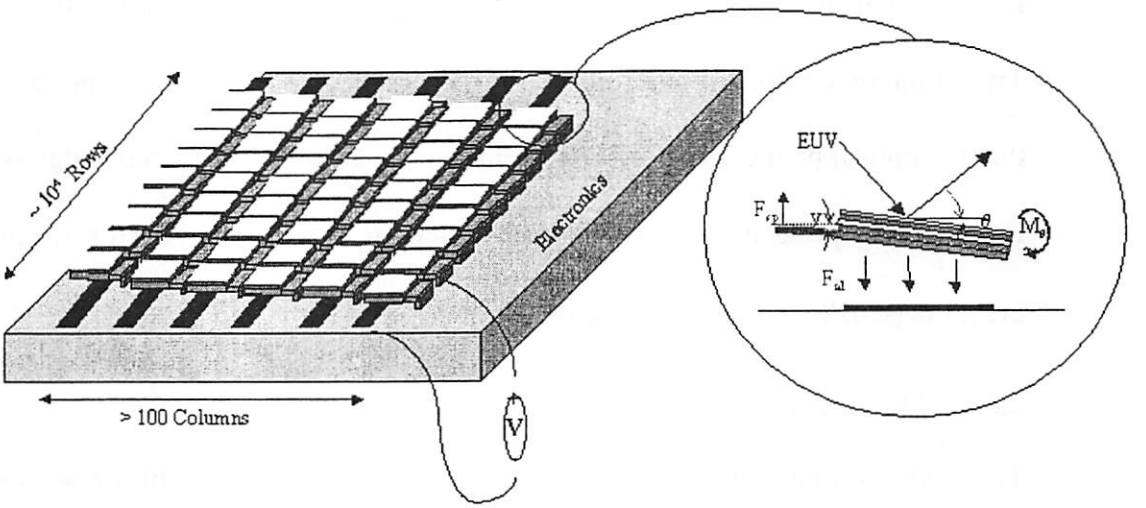

Figure 2-0: Tilting mirror based EUV light modulator (#rows and #columns are not to scale). Inset shows a single nanomirror in detail.

In this section we will discuss some of the architectural constraints that govern a projection optic based maskless lithography system described above.

2.3.1 Mirror ("spot") modulation

The unresolved image of a single nanomirror is referred to as a 'spot' on the wafer plane. The lens demagnification and required feature size on the wafer govern the size of our nanomirrors. Data throughput capability and requrements for image fidelity govern the number of mirrors used to resolve a minimum sized feature at the image plane. For instance, imaging results from Chapter 4 will show that about (2 x 2) mirror "spots" are sufficient to form a "square" contact at the image plane.

Analog modulation capability of the mirrors allows us to do grayscaling to meet the image sizing and placement requirement ($1/50^{th}$ of CD). If approximately 2 mirrors are used to print a minimum sized feature, each mirror needs to be placed within $1/25^{th}$ of its full on-off tilt range. Therefore, mirror control design needs to be robust. It is important to note that nanomirror imaging does not place requirements on the mirror tilt. Transitioning a mirror from a fully 'on' to an 'off' position requires a minimum tilt such that the optical path difference between the center of the mirror and its edge is lambda/2. For instance, using EUV wavelength illumination, and a nominal 1μm mirror size, the off-tilt is $(\lambda/4)/(d/2) = 6.7\text{mrad}$ (or 0.38^{o}).

2.3.2 Magnification factor

To determine what kind of magnification is adequate for our system, we need to compare the required mirror size and 'on' to 'off' angle for various magnification factors (M.F.).

For a given spot size at the wafer, the mirror size scales with maginification. The choice of magnification factor does not affect imaging[1]. However, higher M.F. demands greater

[1] At large *NA*, magnification starts to play an important role.

accuracy in pointing the mirror towards lens pupil. Also, a higher M.F. implies larger mirror size, which means we can fit fewer mirrors on the modulator chip. A lower M.F. allows better latitude in pointing the mirror towards the lens system. We cannot, however, arbitrarily shrink the mirror area for lower M.F. since the multi-layer requirements prevent us from similarly decreasing the mirror height in order to preserve a stable geometry.

2.3.3 Modulation frequency ("flash" architecture)

Mirror modulation frequency is dependent on laser frequency. EUV light source is a non-continuous wave laser. At present, the highest frequency of operation demonstrated by EUV source vendors is around 6kHz. Assuming that a 10kHz source will eventually come to market, the nanomirrors need to operate no faster than the frequency of light being patterned. It is important to note that while the pulse width is in the order of 5 to 20ns. This necessitates the use of a 'flash' architecture. Essentially, the pattern generator is required to load all the data into the memory bank and position the mirrors before each light pulse. For a 10kHz source, the data load time is <100μs accounting for the mirror settling time. The settling time is determined by damping (discussed later in this chapter), resonant frequency of the device, and the starting and ending grayscaled tilt positions.

Flash architecture

For a single chip solution:

- Wafer throughput: 5WPH or 1cm^2/sec (wafer diameter, 300mm)
- Spot-size: 16nm (for a 32nm node)
- If the wafer scan rate is 100cm/sec, the flash rectangle height is given by:

- *Flash_height* = *(AreaScanned/sec)/ScanSpeed*

  = *(1cm2/sec)/(100cm/sec) = 0.10mm*

- The area written per flash is given as:
  - *Flash_area = throughput/flash_frequency*
- The number of mirrors, N, in the modulator to meet the throughput requirement is given by
  - *N = Flash_area/node_area = throughput/(flash_frequency * node_area)*
- Plugging in 1cm2/sec for throughput, 10kHz for flash frequency, and $(32nm)^2$ for node_area:
  - $N = 38.3 \times 10^6$ *mirrors/chip*
- Area of the chip,
  - $Area_{chip} = Area_{mirr} * N * R$,

  where *R* is the built-in redundancy[1] in the chip. Assuming 2x redundancy
  - $Area_{chip} = (1\mu)2 * (40 \times 10^6) * 2 = 0.8cm^2$

[1] The concept of redundancy in micromirrors is similar to its usage in the DRAM world. Redundancy, in our case, refers to the use of multiple mirrors to "flash" light on a single wafer "spot". In this manner, if one mirror becomes defunct due to defect or goes out of specifications, the loss of light for a given wafer location is made up by remaining mirrors.

2.4 Power Dissipation

Since Si/Mo based EUV mirrors reflect about 70% of the light, it is important to get stock of the rate of energy dissipation by the light modulator to ensure that there is negligible rise in mirror temperature. According to the ITRS roadmap, EUV resist sensitivity is around 5mJ/cm^2. Assuming 1cm^2/sec scan rate (5 wafers/hour throughput), the power requirement *at* the wafer is 5mW. Based on nominal values for relevant parameters, we can determine the power density on the mirror chip.

Resist sensitivity: 5mJ/cm^2

Wafer throughput: 5WPH or 1cm^2/sec (wafer diameter, 300mm)

➔ power at wafer, P_{wfr} = 5mW

Assuming 1μm mirrors, for a single chip solution, we need 0.4cm2 chip area for 40mega mirror array. With about 2x redundancy, the chip size is around 1cm^2.

If the projection optic box (POB) has 5 reflective elements, each with an end of life reflectivity of 60%, the light incident on the mirrors, P_{mirr}, must be:

$$P_{mirr} = P_{wfr}/(0.6)^5 = 64\text{mW}$$

So power loss at the mirror is 0.3*64mW or 19mW.

The power density in mirror chip is given by:

$$P_d = 1/R * P_{mirr}/Area_{chip}$$

➔ $P_d = 19mW/0.4cm^2 = 47.5mW/cm^2$

where, again, R is the built-in redundancy in the chip.

2.5 Stress

Stress is critical at two places -- at the interface of Si and Mo layers, and between the polysilicon hinge layer and the last layer of the multi-layer, silicon. In the following analysis, the interface stress between silicon 'substrate' layer and hinge 'film' is studied. By way of terminology, we use *compressive* to indicate negative stress and *tensile* for positive stress.

Residual stress in a film can be measured by wafer curvature. Stress in thin films is determined by the Stoney equation [4]:

$$\sigma = \frac{E_s t_s^2}{6(1-\upsilon_s)t_f \rho}$$

where t_s and t_f depict thickness of the substrate and thickness of the film respectively. ν_s is Poisson's ratio for silicon, R is the radius of curvature, and E_s is the Young's modulus of polysilicon.

The Stoney equation is applicable to thin film stress measurements when the said film is deposited on a substrate where $t_s >> t_f$. We can use a modified form of the equation for flexure tip bending due to built-in stress gradient. The relation between cantilever beam curvature and stress gradient is determined as [13]:

$$\frac{\sigma}{t_f} = \frac{E}{(1-\nu)} \frac{1}{2\rho}$$

If the maximum deflection at the end of the cantilever beam is small compared to the beam length (l), the radius of curvature can be express as:

$$\rho \approx \frac{l^2}{2\delta}$$

and the stress gradient calculated from cantilever tip deflection follows as

$$\frac{d\sigma}{dt_f} = \frac{E}{(1-\nu)} \frac{\delta}{l^2}$$

The flexure length, l, in our design is 100nm. The various parameters are shown in the schematic of Figure 2-0. For the films deposited semi-amorphous at deposition temperature, $T_D \leq 600^{\circ}C$ the stress is highly tensile, owning to contraction of the film during crystallization [6]. The values of Young's modulus and the Poisson's ratio for silicon appear variously in literature, so we have used a nominal value of E_s=170GPa and ν_s=0.28 [5]. We can determine the bending in the hinge due to stress variation along hinge thickness as follows:

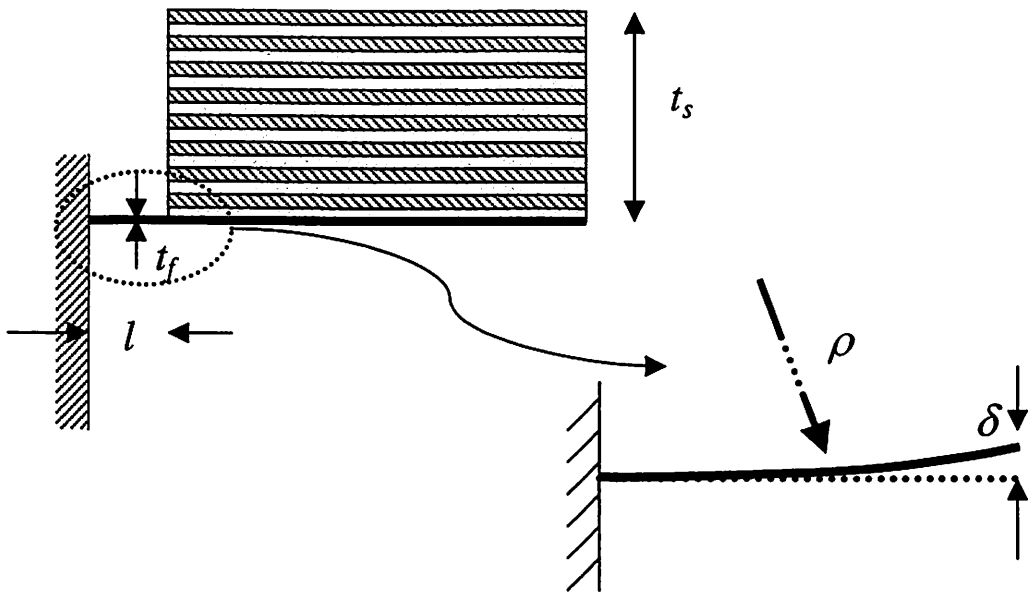

Figure 2-0: Flexure curvature due to residual stress gradient.

$$t_f = 10^{-8} m$$

The flexure tip bending as a result of stress gradient must be:

$$\delta = l^2 (\frac{d\sigma}{dt_f}) \frac{(1-\nu)}{E} = (10^{-8})^2 * \frac{(1-0.28)}{170 \cdot 10^9} \frac{d\sigma}{dt_f}$$

For 1000MPa/μm stress gradient, tip bending is:

$$\delta = 4.2pm \Rightarrow \textit{tip tilt angle} = 4.2\mu rad.$$

Assuming stress gradient can be kept lower than 1000MPa, tip bending due to stress can be considered negligible.

2.6 Nanomirror Mechanics

2.6.1 Non-contact behavior

Successful operation of the light modulator array depends on the robustness, similarity, and reliability of each individual pixel and the ability to control all the pixels over time.

Some of the problems that may cause deviation from ideal behavior of the micromirror are due to stiction and static surface charges. To avoid such stiction effects, a non-contact mode of operation is chosen.

2.6.2 Nanomirror model

Figure 2-0(a) shows an electromechanical model of a nanomirror as seen from the side. The mirror motion is governed by two forces acting against each other – a *mechanical* spring force, F_s, due to the bending of the flexure and an *electrostatic* force, F_e, due to the attraction between the underside of the nanomirror structure and the underlying electrode. Solving for the spring and electrostatic force allows us to calculate the mirror position for any applied voltage.

In the deflection model presented here, the fringing effects are ignored and only surface charges from the addressing electrode are taken into consideration. Another assumption is that the bending of the mirror is negligible, i.e. the only bending occurs in the hinge.

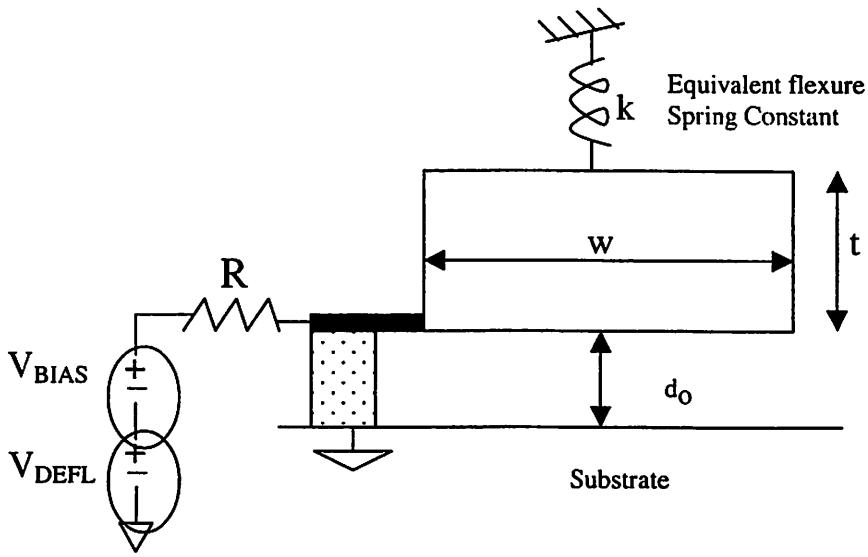

Figure 2-0 (a): Schematic of a nanomirror array. Resistor R is built into the flexure hinge.

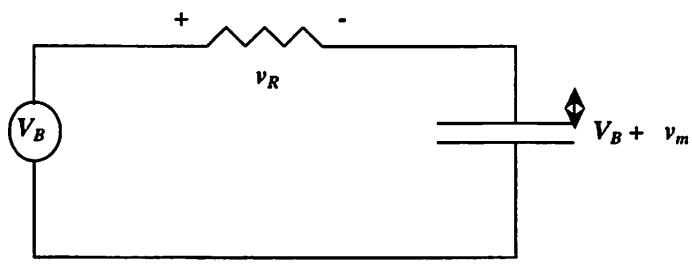

Figure 2-0 (b): Equivalent electrical circuit of the schematic in (a). In the parallel plate model, the capacitive gap modulates by δx.

The mirror tilts about the hinge axis. For a parallel plate capacitor, the electrostatic force between the two plates is simply the differential of the energy stored with respect to distance. Hence, we can write:

$$F_e = \frac{d}{dz}\left(\frac{1}{2}C(z)*V^2\right)$$

Using ε for permittivity, w as the width of the capacitor, and b as its thickness, we can rewrite the above equation as:

$$F_e = \frac{1}{2}V^2\frac{d}{dz}\left(\varepsilon\frac{wb}{z}\right) \rightarrow \quad F_e = -\frac{1}{2}V^2\varepsilon\frac{wb}{d_0^2}$$

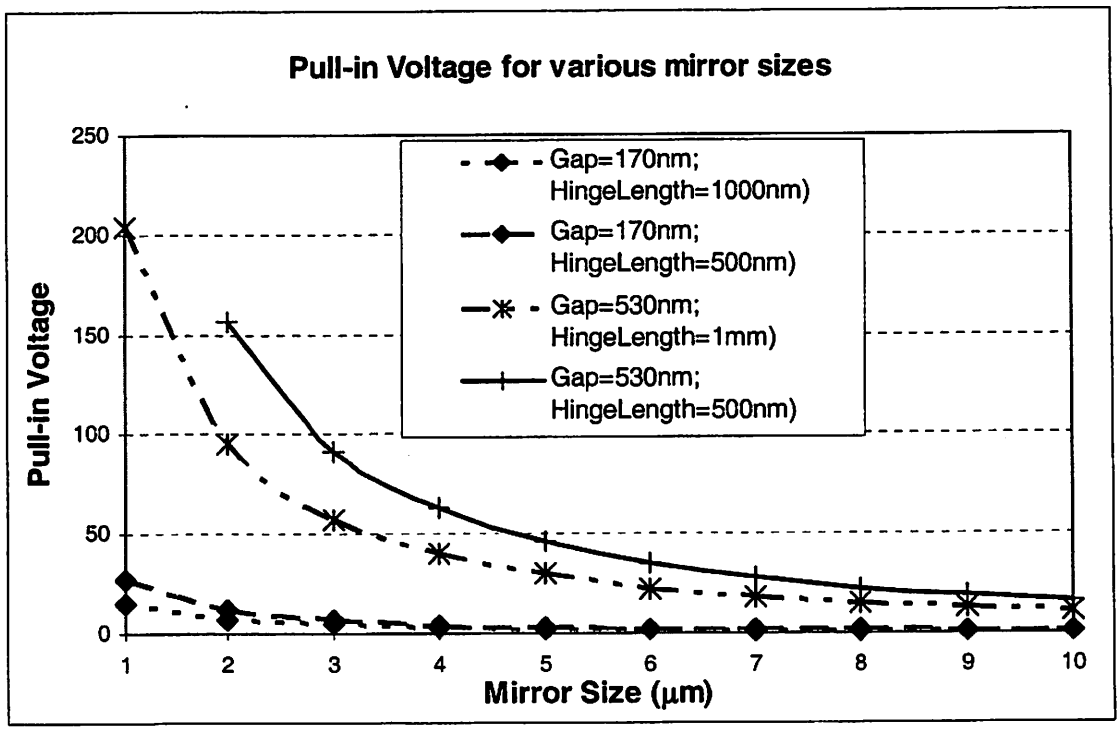

Figure 2-1: A comparison of numerical and analytical models for the parallel place capacitor design.

The mirror is tilted as a result of applied voltage across the gap. For such a non-parallel structure, the total electrostatic force on the mirror element is calculated by integrating the incremental force of the segment, which is directly in front of the address electrode:

$$F_e = \int_0^w dF_e(x) \qquad \textit{Eq. 2-1}$$

where w now is the width of the address electrode. For rotation of an angle θ (radians) the electrode gap can be expressed as $d(x) = d_o - x*\sin\theta$, where d_o is the initial gap between mirror and address electrode. For small angles, $\sin\theta \approx \theta$. Based on equation for electrostatic force, F_e, we can get an expression for the differential electrostatic force:

$$dF_e(x) = \frac{\varepsilon_o t V^2 dx}{2(d - y(x))^2} = \frac{\varepsilon_o t V^2 dx}{2(d - y_o - \theta \cdot x)^2} \qquad \textit{Eq. 2-2}$$

where t is the length of the mirror and y_o is the displacement of the hinge. Plugging the differential equation into the integrand and solving gives:

$$F_e = \frac{\varepsilon_o t V^2}{2\theta} Ln\left[\frac{d - y_o}{d - y_o - t\theta}\right] \qquad \textit{Eq. 2-3}$$

The total electrostatic force can be considered as a point force applied at the tip of the flexure. However, to calculate the total deflection of the flexure tip, we also need to account for the moment resulting from a distributed electrostatic force.

$$M_e = \frac{\varepsilon_o t V^2 (d - y_o)}{2\theta} Ln\left[\frac{d - y_o}{d - y_o - t\theta}\right] \qquad \textit{Eq. 2-4}$$

As the applied gap voltage increases, the mirror starts to tilt, thus applying a torque on one end of the hinge. The mechanical torque due to the bending hinge balances the electrostatic torque.

The electric force F_e has to be counteracted by the mechanical force F_m due to the suspension of the micromirror on the hinge. The hinge behaves like a spring with a

spring constant k and $F=kd$, where k is composed of two terms, a hinge cross-section term and a mechanical stress term (due to process related residual stress in the flexure). For first order approximation, the stress term is left out in this analysis. Using $k=\frac{4l^3}{a^3bE}$, the deflection y_o of a beam fixed at one end with a load F at the tip for a hinge of length L, thickness a, and width b is [14]:

$$y_o = y(l) = \frac{4l^3}{a^3bE}F + \frac{6l^3}{a^3bE}M \qquad \textit{Eq. 2-5}$$

where E is the Young's modulus for silicon. The tip angle is similarly extracted from the force and moment equations. Summarizing the deflection equations gives us the well-known bending matrix of beam theory:

$$\begin{bmatrix} y \\ \theta \end{bmatrix} = \frac{L}{EI}\begin{bmatrix} L^2/3 & L/2 \\ L/2 & 1 \end{bmatrix}\begin{bmatrix} F_y \\ M_\theta \end{bmatrix} \qquad \textit{Eq. 2-6}$$

Numerical analysis is required to solve for the tip deflection vs. applied voltage from the electrostatic and mechanical force equations. The following figure shows the bending angle and tip deflection for nominal device parameters.

In Figure 2-1, $\delta y(V_g)$ and $\theta(V_g)$ have been plotted for hinges of varying thickness. In each case, the length is kept constant at 100nm and the width also constant at 1μm.

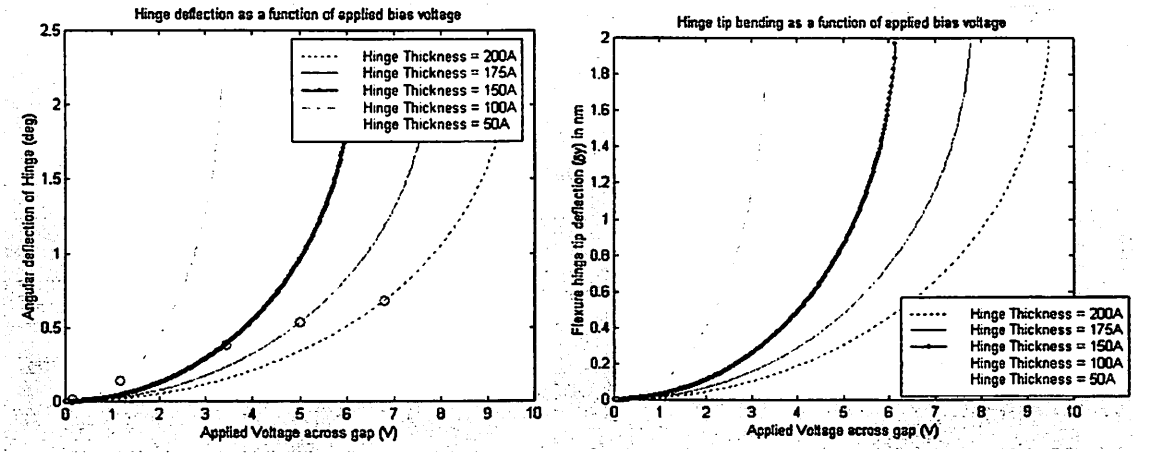

Figure 2-1: (a) Mirror tilt and (b) hinge deflection plotted as a function of applied voltage

Mirror gap is held constant at 100nm. Snap-down occurs when the mirror tilts sufficiently to cross 1/3rd gap.

To determine the natural frequency, we need a modification of the spring constant such that

$$k_\omega = k * \frac{l^2}{(l + \frac{w}{2})^2} \qquad \textit{Eq. 2-7}$$

to give the natural frequency,

$$\omega = \sqrt{\frac{k_\omega}{m}} \qquad \textit{Eq. 2-8}$$

using l=100nm, mirror width, w=1μm, mirror mass, m~10^{-15}kg. We need to have a very high resonant circuit since our operating frequency is very high. Figure 2-1 plots the resonant frequency as a function of bias voltage required to get 0.5° bending. We need a *weak* hinge to reach the desired bias angle for small electrostatic force; hence resonant

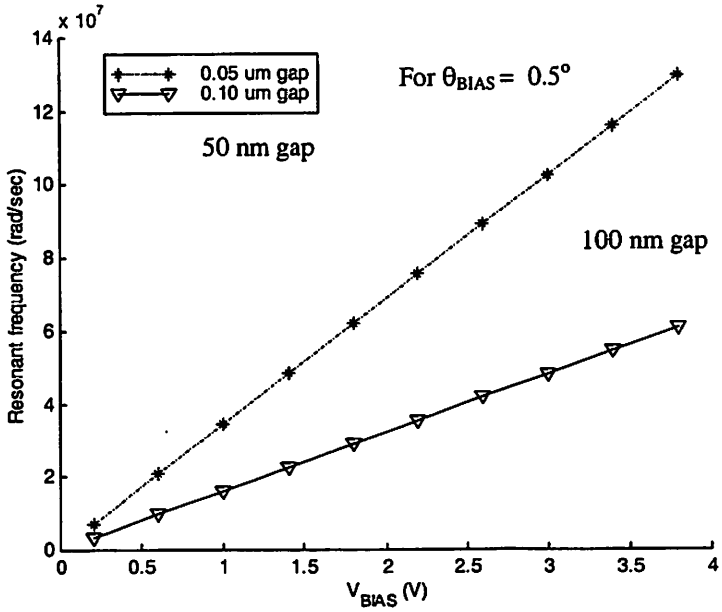

Figure 2-1: In order to meet the throughput requirements, a high resonant frequency is desirable. A small mirror gap coupled with high bias can provide a large resonant frequency.

frequency is low at low voltages and large gap width. Voltage constraints prevent us from achieving an arbitrarily large ω_o.

2.6.3 Summary

Presented below is a short table with all the parameters along with their nominal values.

Table 2-0: Summary of nanomirror properties

Mirror
Thickness, t ~ 400 nm
Area, w^2 ~ 1x1 μm^2
Gap, d_o ~ 100nm
Hinge
Thickness, a ~ 10nm
Width, b ≤ w
Length, l ~ 100nm
Resistance, R ~ 10^7 ohms
Spring constant, k ~ 40N/m

Unless otherwise stated, these values will be used in the simulation results of the next section.

2.7 Quality factor control

2.7.1 Introduction to damping

Damping is desired in order to achieve a flat response over a wide range of frequencies. Control over the quality factor is very crucial in order to quickly and accurately position the micromirror. The quality factor Q is defined as the total energy stored in the structure divided by the sum of energy losses from the vibrating element per cycle. Initial studies for damping mechanism focused on using squeeze-film damping caused by having a gaseous film in the mirror gap.

2.7.2 Gaseous – squeeze film damping

Mechanical energy from the mirror can be dissipated through viscous damping caused by the introduction of a viscous material in the mirror gap. This method of damping does have some challenges. EUV lithography is done in a high vacuum environment to prevent optic reflectivity degradation due to oxidation as well as reduce EUV light absorbtion. For instance, non-linear and incompressible behavior of gas films can lead to undesirable spring-force behavior from the gas. Also, we may reach the limits of continuous flow in very thin damping layers. This is called 'slip-flow' in lubrication terminology and is accounted by the squeeze number, σ. We have to ensure that $\sigma << 1$. Squeeze film damping can be achieved with either a gaseous or liquid film. Gaseous film is better since it is less temperature dependent than liquid damping because of the smaller relative change in viscosity of a gas as compared with a liquid. In addition, liquid in the mirror gap needs more design restrictions. Before delving into the particulars, it is necessary to establish some of the important parameters that characterize our system.

First, to use a linearized form of the Reynold's equation describing fluid pressure the cavity, we need to establish that the Reynold's number is much smaller than unity. Reynold's number is given as:

$$Re = \frac{\omega h^2 \rho}{\eta_{eff}} << 1$$

where: ω (10^8 rad/sec) is the oscillating frequency of the mirror plate,

h (10^{-7} m) is the cavity gap (see Figure 2-0),

ρ is the gas density, and

η_{eff} is the effective viscosity of the gas.

At small pressures, when the molecular mean free path λ is not negligible compared with the gap height, the gas flow can be modeled by a modified Reynolds equation represented by using effective viscosity:

$$\eta_{eff} = \frac{\eta}{1 + f \cdot K_n^{\gamma}}$$

where $K_n = \lambda/d_o$ is the Knudsen number and μ is the viscosity coefficient at the ambient pressure. f and γ are constants determined by the geometry of the cavity. For a rectangular parallel plate cavity, $f = 9.638$ and $\gamma = 1.159$ [7].

To determine the Knudsen number, we need to find out the mean free path, λ:

$$\lambda = \frac{1}{\sqrt{2}\pi \cdot N \cdot r^2}$$

where :

N is the number of gas molecules per unit volume (m^3), given by

$$N = P * Na / (R \cdot T)$$

Na is Avagadro's number (6.02e23);

P is pressure in Pascal;

T is ambient temperature (300 K), and

R is Rydberg's constant (8.3143).

r is the atomic radius of the damping gas ($1.3 \cdot 10^{-10} m$ for He)

For a given pressure of 5 Torr, using mean free path, $\lambda \sim 21.6\mu m$ and gap width, $h_o = 0.1\mu m$, we get the Knudsen number $K_n = 216$. The viscosity of Helium at T = 300K and 5 Torr pressure is experimentally found to be $\eta = 20\mu Pa$ sec. Thus, we can calculate the effective viscosity

$$\eta_{eff} = 4.1 nPa\ sec.$$

Now we are ready to check if we meet the criteria for using a linearized form of Reynold's equation:

$$Re = \frac{10^8\ rad/sec \cdot (10^{-7} m)^2 \cdot 10^{-4}\ kg/m^3}{4.1 \cdot 10^{-9}\ Pa \cdot sec} = 0.1 << 1$$

Squeeze number: Another parameter that defines whether or not we are operating in the slip-flow mode or continuum. In slip flow mode, the gaseous film acts essentially as a spring force and causes little damping. For a low squeeze number (< 1), we are in a continuum. The squeeze number is given as:

$$\sigma = \frac{12\omega \cdot \eta_{eff}^2 L^2}{h_o^2 \cdot P}$$

where, L: effective length of the cavity (1μm in our case) and other parameters are as defined earlier. When $\sigma = 1$, it defines the cut-off frequency ω_T. For mirror operating frequency below the cut-off frequency, the gas film has enough time to move away and dissipate energy (referred to as *continuum* mode). For a mirror oscillation frequency higher than the cut-off frequency, the gas film is incompressible and acts like a spring with low dissipation (also known as slip-flow in lubrication terminology). We can set $\sigma = 1$ and calculate the mirror cut-off frequency:

$$\sigma = \frac{12 \cdot (\omega_T \text{ rad/sec}) \cdot (4.1 \cdot 10^{-9} \text{ Pa} \cdot \text{sec})^2 \cdot (10^{-6} \text{ m})^2}{(10^{-7} \text{ m}) \cdot 1000 \text{ Pa}} = 1 \quad \Rightarrow \quad \omega_T = 5 \cdot 10^{16} \text{ rad/sec}$$

In our case, the mirror operating frequency is $\omega \sim 10^8$ rad/sec, so we are quite safely in the continuum mode.

Reynold's equation for pressure distribution

The pressure-variation in the mirror gap is given by Reynold's equation. We can utilize a linearized form of this equation by virtue of having a small modulation displacement [7]:

$$\frac{h_o^3}{\eta_{eff}}\left(\frac{\partial^2 P}{\partial x^2}+\frac{\partial^2 P}{\partial y^2}\right)=12\frac{\partial x}{\partial t}$$

where:

P is the pressure departure within the film from the ambient value;

ρ is the density;

η_{eff} is the effective viscosity;

h_o is the nominal gap distance, and

dx/dt is the time dependent small-signal mirror modulation.

The linearized Reynold's equation is solved to get a pressure profile under the structure. Integrating the pressure profile over the gap surface gives us the damping force equation. [8] has done this and shown that the damping force for a rectangular surface is given by:

$$F_d = 0.41 \cdot \mathrm{A}^2 \cdot \eta_{eff} / h_o^3 \cdot dx/dt$$

For a second order equation of motion, the total force is given as:

$$F = m \cdot \ddot{x} + b \cdot \dot{x} + kx$$

Comparing the second term of the total force equation to the squeeze-film damping force, we obtain the damping coefficient:

$$b = 0.41 \cdot \mathrm{A}^2 \cdot \eta_{eff} / h_o^3$$

Finally, the quality factor Q is given as:

$$Q = \frac{mass * \omega}{2 \cdot b}$$

For a given temperature T = 300 K, the coefficient of viscosity η is pretty much a constant. Keeping that in mind, we can calculate the effective viscosity for a range of pressures. Similarly, we can obtain the coefficient of damping and quality factor Q. Figure 2-1 shows achievable Q for varying pressures (keeping in mind that the conditions for continuum and low Reynold's number are not violated). For optimum damping, a quality factor Q ~ 1/2 is necessary. However, it is clear that gaseous damping does not permit such high degree of damping. As a result, another option of using electrical damping was explored.

2.7.3 Resistive damping (charge pumping)

In this section, we study resistive damping as a means of obtaining a low Q system. Initially, a bias voltage, V_B, is applied to introduce damping charge into the system. As we apply modulation voltage, v_m, over bias voltage V_B, charge pumping across the resistor leads to electrical dissipation of mechanical energy. The following damping analysis is based on a parallel-plate model depicted in Figure 2-0. The electrical equivalent of the model is shown in Figure 2-0. Various parameters used in this analysis are:

d': Biased height of the mirror plate

V_B: Bias voltage

v_m: Modulation voltage (<< V_B)

x: Capacitor top plate modulation

R: Built-in resistor

w: Side length of the mirror

A: Area of the mirror (capacitor); A = w^2

ε_o: Free-space permittivity

Current flowing through the system is given as:

$$i = \frac{d(C \cdot Vc_c)}{dt} = C \cdot \frac{\partial Vc}{\partial t} + Vc \cdot \frac{\partial C}{\partial t}$$

Capacitance, $C = \frac{A \cdot \varepsilon_o}{(d'-x)}$

$$\Rightarrow \frac{\partial C}{\partial x} = \frac{A \cdot \varepsilon_o}{(d'-x)^2} = \frac{A \cdot \varepsilon_o}{d'^2 - 2d'x + x^2}$$
$$\cong \frac{A \cdot \varepsilon_o}{d'(d'-2x)} = \frac{C}{d'(1-2a)} \quad \text{(using } a = x/D')$$

Applying the binomial expansion:

$$\frac{\partial C}{\partial x} \cong \frac{C}{d'} \cdot (1+2a)$$

Since, $\frac{\partial C}{\partial t} = \frac{\partial C}{\partial x} \cdot \frac{\partial x}{\partial t}$ we can describe the dynamic change in capacitance with time as

$$\frac{\partial C}{\partial t} = \frac{C}{d'} \cdot (1+2a) \cdot \frac{\partial x}{\partial t}$$

We can re-write the current equation in phasor notation for ease of calculation:

$$i = j\omega \cdot C \cdot v_m + (V_B + v_m) \cdot \frac{C}{d'}(1+2a) \cdot j\omega \cdot x$$

Applying Kirchoff's rule to the small-signal loop equation of the circuit in Figure 2-0:

$$v_R + v_m = 0$$

Since $v_R = i \cdot R$, we can use the current equation to get:

$$v_m \cdot (1 + j\omega \cdot RC) = -j\omega \cdot RC \cdot V_B \cdot a$$

Since $v_m = -v_R$, we can rewrite the above equation to get voltage across the resistor:

$$v_R = V_B a \cdot \frac{j\omega RC}{1 + j\omega RC} \text{ or } |v_R|_{avg} = \frac{1}{2\sqrt{2}} V_B a \cdot \frac{\omega RC}{1 + (\omega RC)^2}$$

Power dissipation can now be calculated as we have the average voltage drop across the resistor:

$$|P|_{avg} = \frac{|v_R|^2_{avg}}{R} \Rightarrow |P|_{avg} = \frac{1}{2}\frac{V_B^2}{R} \cdot \left(\frac{x}{d'}\right) \cdot \left(\frac{1}{\sqrt{2}}\right)^2$$

Hence, the average power dissipated is given:

$$Power_{average} = \frac{V_B^2}{R} \cdot \frac{a^2}{4}$$

Calculating the quality factor, Q

The quality factor can be calculated either by using differential equation representation of the motion of the spring or by using the definition of Q itself:

Q= 2 PI * Energy_Stored/Energy_Dissipated

We will try to derive Q using the differential equation method [9].

We start with the damping force, $F_d = b \cdot \frac{\partial x}{dt}$, and its mechanical counterpart:

$$F = m \cdot \frac{\partial^2 x}{dt^2} = kx + b\frac{\partial x}{\partial t}$$

Work done in one cycle must be:

$$F_d \cdot x = P_{avg} \cdot t_{cycle}$$

$$\text{So, } b \cdot \left.\frac{\partial x}{dt}\right|_{1cycle} \cdot x = \frac{1}{4}\frac{V_B^2}{R} \cdot \left(\frac{x}{d'}\right)^2 \cdot \left(\frac{2\pi}{\omega}\right)$$

$$b \cdot x^2 \cdot \left(\frac{\omega}{2\pi}\right) = \frac{1}{4}\frac{V_B^2}{R} \cdot \left(\frac{x}{d'}\right)^2 \cdot \left(\frac{2\pi}{\omega}\right)$$

$$b = \frac{1}{R} \cdot \left(\frac{\pi}{\omega}\right)^2 \left(\frac{V_B}{d'}\right)^2$$

Quality factor, as defined earlier:

$$Q = \omega_n \frac{m}{2 \cdot b}$$

Substituting the definition of b derived earlier, we get

$$Q = \omega_n \cdot \frac{mR}{2} \cdot \left(\frac{\omega_n}{\pi}\right)^2 \left(\frac{d'}{V_B}\right)^2 \rightarrow Q = \frac{\omega_n{}^3 mR}{2 \cdot \pi^2} \left(\frac{d'}{V_B}\right)^2$$

Figure 2-1 shows the relation of the quality factor for varying resistance values. The bias

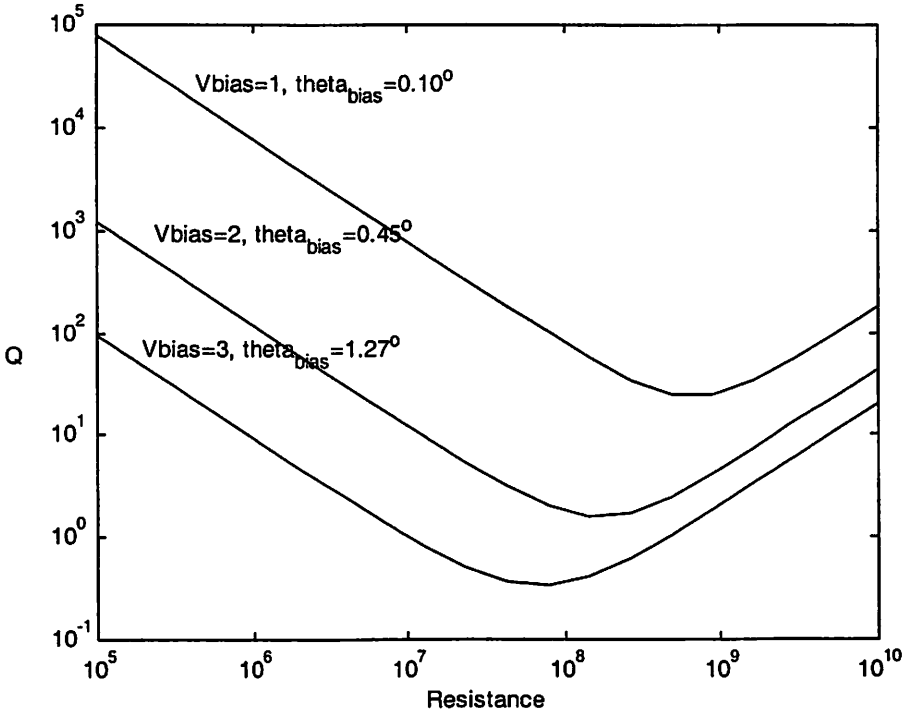

Figure 2-1: Minimum Q is achieved for an optimum resistance. Simulation was carried out for a nominally sized mirror described in the 'summary' of chapter 3.

voltage is changed to show that in order to get optimum Q, we need a minimum bias voltage. For the plot in Figure 2-1, we have chosen a mirror with nominal parameters described in the summary of chapter 3 -- hinge thickness 100A, hinge length 100nm, gap distance 100nm.

2.7.4 Design Issues

The geometry of the mirror is constrained by various factors based on the system requirements and damping issues. Nominal values of mirror flexure hinge spring constant, gap distance, modulation voltage, and bias voltage need to be determined. The inset in Figure 2-0 shows these parameters in a nanomirror schematic. Note that while

this is a horizontal flexure hinge, one could just as easily use a vertical flexure hinge to save area and achieve a higher fill-factor ratio.

Bias voltage: The mirror is activated using a small-signal modulation voltage superposed on a bias voltage, V_B. The bias voltage provides damping charge to the system and needs

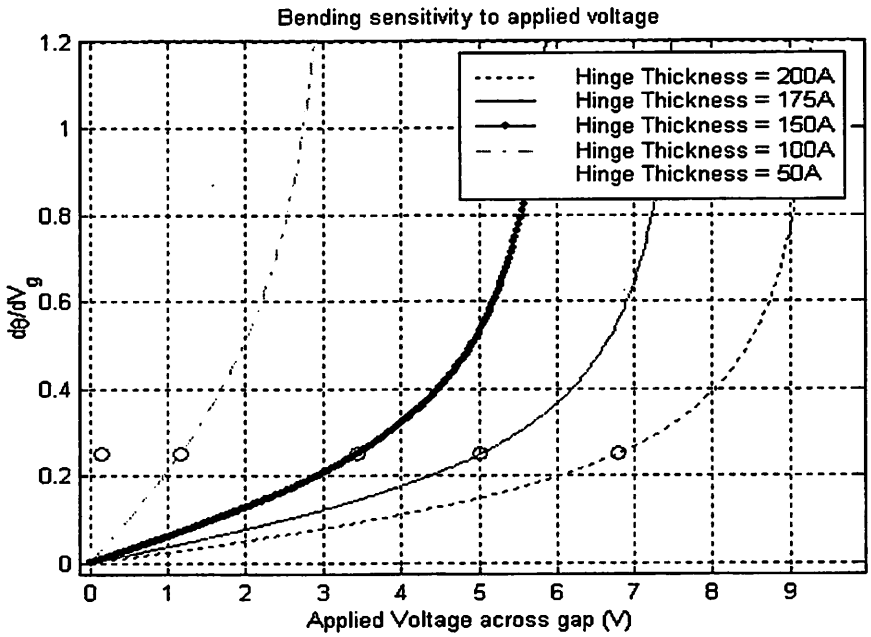

Figure 2-1: Mirror sensitivity as a function of applied voltage.

to be sufficiently larger than the modulation voltage for small-signal analysis to hold. The precise magnitude of the bias voltage is governed by bending sensitivity plotted in Figure 2-1. For a constant flexure hinge thickness (100nm), the plot of dθ/dVg shows that a higher bias voltage provides higher bending sensitivity.

Modulation voltage: Since the control electronics has to be embedded as a cell within each mirror, MOSFETs that have length in the deep sub-micron regime are required. For 0.1μm technology circuits, the supply voltage is around 1V, hence our modulation voltage is constrained to be less than a volt.

Spring Constant: The bending equations described in chapter 3 allow us to calculate the spring constant for a given gap voltage and gap distance using the following equation:

$$k = 3\frac{EI}{L^3}$$

where,

E (Young's modulus) = 170GPa (crystalline silicon [5])

I =moment of inertia, = $\frac{a^3 b}{12}$ [a: hinge thickness; b: hinge width]

L: Hinge length

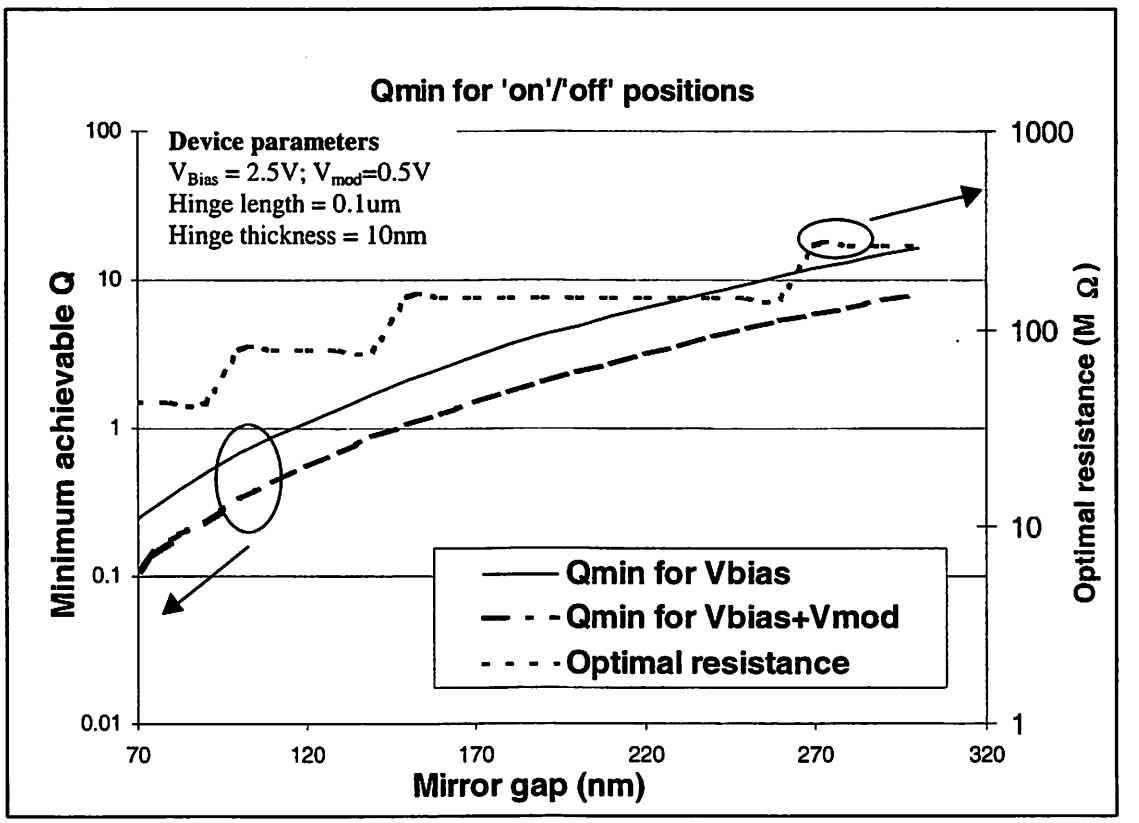

Figure 2-1: For a given gap, we plot the minimum achievable quality factor and the corresponding required resistance. Q is a function of applied voltage, hence, we have Qmin for both 'on' and 'off' positions.

For a mirror gap of 100nm and 1-degree bias with 2.75 volts, the flexure hinge spring constant is around 42.5N/m achieved with a hinge thickness of 10nm.

Mirror Gap: Based on simulations, we have realized that the smaller the gap, the better quality factor control we achieve. This makes sense, as we have better control over the mirror from larger electrostatic force across a smaller gap. Our system architecture constraints demand that the modulation angle be a minimum ½ λ optical path difference between the center and edge of the mirror.

Very small gaps will result in snap-down of mirrors before reaching bias or modulation angles. Figure 2-1 shows the achievable quality factor for various gaps. Using a gap of 100nm with a bias voltage of 2.50V we get Q_{min} = 0 69. Applying a modulation voltage of 0.5V gives a new Q_{min} of 0.34V (optimum resistance of R ~78MΩ in both cases).

2.8 Conclusions

A first order analysis of a nanomirror device has been completed and results of simulation done using MatLab have been presented. Various groups have fabricated micromirror arrays in the past, however, our application puts forth stringent demands on the size and response of the system. Since the mirrors are intended to be used for Next Generation Lithography, we have tried to set architectural constraints based on what we perceive the future to be according to current trends in the industry. We have tried to make knowledgeable assumptions regarding the size of the wafers, EUV resist sensitivity, and feasibility of getting 33x demagnification. The eventual numbers will not be too far away from what we have used in our first order feasibility analysis.

Throughput requirements place the mirror operating frequency in the range of kHz, however, the resonant frequency must be high for low settling time. Hence we need a high resonant frequency. Smaller gaps are better for high ω_n; however, we are constrained by snap-down in making the gaps arbitrarily small. Device release also becomes more difficult as sacrificial gap thickness decreases.

Though the mirrors absorb nearly 30% of incoming radiation, we have shown that conductivity through the hinge is large enough for the mirror temperature not to be of concern.

With high operating frequency comes the added task of critically damping the structure. Gaseous damping is inadequate. Electrical damping can be achieved by dissipating the mechanical energy of the spring into electrical heat loss by charge pumping. To get a low enough Q, we need to embed a 50-100MΩ resistor in the flexure hinge. An optimum value of the resistor has been found for different device structures.

Mirror modulation also places stringent requirements on the modulation voltage. To fit enough circuitry underneath each mirror to intelligently transfer data across the rows, we would require transistors with effective channel length in the deep sub-micron regime. The available supply voltage for a 0.1μm channel transistor would be around 1V. Hence, our modulation voltage is constrained to be below this value.

Data Memory requirement

Lastly, a word about the underlying memory bank that would drive the mirror array. Addressing each mirror is possible by embedding analog and digital logic circuits underneath the mirrors. SRAM cells are good for proof-of-concept type demonstration,

however, ultimately, to fully realize a maskless system, it is necessary to implement memory cells with a much smaller foot-print than 6-T SRAM design. Once the data is written to the memory bank it needs to be read only once in the flash architecture introduced in chapter one. 1-T DRAM cells with multi-value storage are necessary to accommodate grayscaling. On the other hand, these cells need not retain the data after one read. Efficient memory cell design is a challenging component of this modulator.

2.9 References

[1] V. Dai, A. Zakhor, "Lossless layout compression for maskless lithography systems", SPIE vol. 3997, pp. 467-77, 2000.

[2] B. Wild, "Data Handling Circuitry for Maskless Lithography Systems", Masters Report, Electronics Research Lab (ERL), Department of EECS, UC Berkeley, 2002.

[3] V. Dai, A. Zakhor, "Lossless compression techniques for maskless lithography data", Emerging Lithographic Techniques, SPIE vol. 4688, pp 583-594, 2002.

[4] P.A. Flinn, "Principles and application of wafer curvature techniques for stress measurement in thin films", Thin films: Stresses and Mechanical Properties Symp., Mater. Res. Soc., '89, pp. 41-51.

[5] S. C. Jain, et., al., "Edge-induced stress and strain in stripe films and substrates: A two dimentionsional finite element calculation," Journal of Applied Physics, vol. 78, no. 3, 8/95.

[6] H. Guckel, J. J. Sniegowski, et. al., "Fabrication of micromechanical devices from polysilicon films with smooth surfaces", *Sensors and Actuators, 20 ('89), pp 117-22.*

[7] T. Veijola, H. Kuisma, et. al. "Equivalent-circuit model of the squeezed gas film in a silicon accelerometer", Sensors and Actuators A, vol. 48, pp. 239-48.

[8] J. Starr, "Squeeze-film damping in solid-state accelerometers", Technical Digest. IEEE Solid-State Sensor and Actuator Workshop, Hilton Head Island, SC, USA, 4-7 June 1990, pp 44-47.

[9] G. Kovacs, "Micromachined Transducers Sourcebook", McGraw Hill publishers, '98.

[10] N. Chokshi, F. Pease, Y. Shroff, Y. Chen, W. Oldham, R. Pease, et. al, "Maskless EUV Lithography", Journal of Vacuum Science and Technology B, Nov. 1999.

[11] Y. Shroff, Y. Chen, W. Oldham, "Optical Analysis of Nanomirror based Pattern Generation", SPIE vol. 5037, Microlithography Conference, Santa Clara, Feb. 28, 2003.

[12] O. Solgaard, F. Sandejas, D. Bloom, "Deformable grating optical modulator," Optics Letters, vol.17, no.9, 1 May 1992, pp.688-90. USA.

[13] W. Fang, J. Micromech. Microeng. vol. **9**, pp 230, 1999.

[14] R. Roark, "Roark's formulas for stress and strain," McGraw-Hill, 7^{th} *Ed.*, Sept. 2001.

3 Fabrication process

3.1 Introduction

In this chapter, the process flow for a tilting mirror is presented. The process flow uses 5 masks which were fabricated at the UCB microlab. A 356nm g-line stepper was used for lithography which restricted the minimum feature size on the devices to about 0.8μm dark-line at best. Various mirror parameters, such as electrostatic gap, flexure thickness are modified to reflect the lithography limit, keeping the spring constant similar.

In this chapter, the materials aspect of fabrication is addressed first, followed by the process-flow of the parallel plate structure. Issues that most affected device fabrication, such as stress, silicon-germanium interaction, and the release process are addressed next. We conclude with a look at a collage of SEM devices fabricated in the results section.

3.2 Processing related considerations

Thermal budget: Unlike more conventional uses of digital light modulator schemes such as for LCD or video projection sytems, the resolution demanded by an EUV system is substantially more demanding. The use of a separate driving circuitry chip is not viable; we need embedded electronics in the nanomirror modulator as discussed in the previous chapter. From a design point of view, this translates into placing memory cells underneath the mirrors to provide decompression on the fly or to "intelligently" route gray-scaled data to the next column at each clock tick. From a fabrication point of view, having

embedded IC with mirrors on top constraints us to a tight thermal budget. This is in order to prevent excessive dopant diffusion or interconnect metal (Cu) seepage into surrounding dielectrics during micromirror processing.

Structural layer: EUV light is easily absorbed by most materials. Therefore, EUV lithography uses reflective optics and masks. The EUV mirrors are composed of approximately 40 bilayers of Silicon and Molybdenum that collectively reflect light. Each bilayer is about ½ λ thick. The Si/Mo stack is around 0.3μm. For the purpose of this research, it is not practical to work with Si/Mo stack. Instead, we can choose (amorphous or poly-crystalline) silicon as the structural material.

Sacrificial layer: Apart from observing a tight thermal budget, the mirror release process needs to accommodate the IC passivation layer, generally phosphosilicate glass or PSG. Thus, the use of well established oxide release process would not be suitable. In general, the sacrificial material of choice should have the following properties: etchant should be highly selective to not only the device structural material, but also PSG; gas or plasma etchant is preferred over wet-etchants to better avoid stiction; surface roughness and interlayer diffusion (between the sacrificial layer and structural material) should be non-existant.

Germanium is chosen as a sacrificial material primarily because hydrogen peroxide based etches provide high selectivity to both silicon and oxide [2]. Germanium interaction with polysilicon at high temperature (~600C) provided some interesting results that are discussed in a later section.

3.3 Process flow

The nanomirror fabrication process flow is depicted in Figure 3-0. The bottom electrode is not shown for clarity. We start with ~2000A thick oxide coated <100> Si wafers to ensure that the devices are isolated. LPCVD of diborane doped a-SiGe (450C, silane gas + germane) is carried out followed by MASK 1 patterning (not shown in Figure 3-0). It forms the bottom electrode and has a thickness of around 1000A. Sacrificial Ge is deposited next at 350C, using germane deposition gas and an initial few monolayers of silicon nucleation (necessary to provide deposition sites on oxide). Ge determines the separation distance between two electrodes. Since the electrostatic force is inversely proportional to the square of the electrode gap, it is very crucial to have a precise thickness of Ge. Using 88sccm GeH_4 flow, 600mT pressure, and at 350C temperature, Ge roughness of Ra=10nm was achieved. Ge is patterned (MASK2) to create trenches, followed by a thin (~500A) of doped a-SiGe deposition making up the flexure hinge. The flexure hinge has a dual purpose – mechanically, it acts as a spring that pulls back the mirror to its bias position when turned 'OFF' and electrically, it acts as a resistor that induces damping. As with the sacrificial layer, thickness of the hinge also needs to be carefully controlled since the beam spring constant is proportional to the cube of the hinge thickness; hence, a slight variation in beam thickness can significantly alter the voltage transfer function.

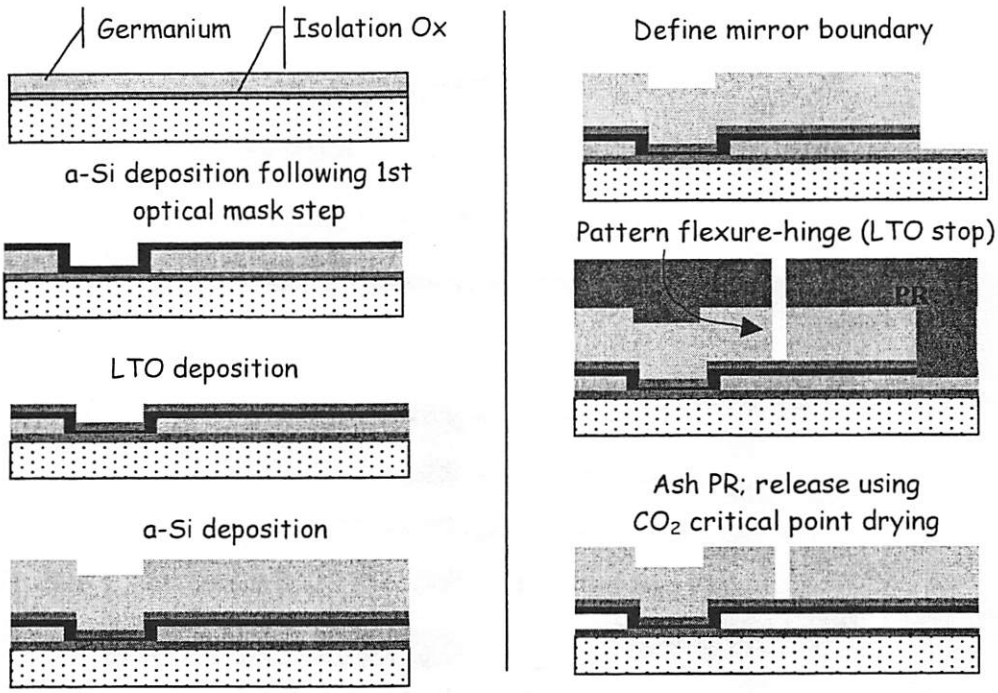

Figure 3-0: Parallel-plate nanomirror array process flow (bottom electrode not shown for clarity).

Flexure hinge deposition is followed by 500A of LTO patterned (again with MASK2) to create contact between the hinge layer and subsequently deposited mirror layer. The last layer is again diborane doped α-SiGe, (3000A) which acts as a mirror and upper electrode. Thickness of the mirror layer is determined by EUV ML stack thickness which is 40 bi-layers of approximately quarter-wavelength (λ = 13nm) thick Si/Mo.

A chemical-mechanical-polish of the mirror layer is carried out to reduce the surface roughness of the devices. Next, we pattern (MASK3) and etch the mirror from three sides, stopping on sacrificial Ge layer. A final lithography step is performed to create the hinge, etching through the mirror silicon to stop on LTO. A final release step, involving Ge etch, is performed to get free-standing mirrors.

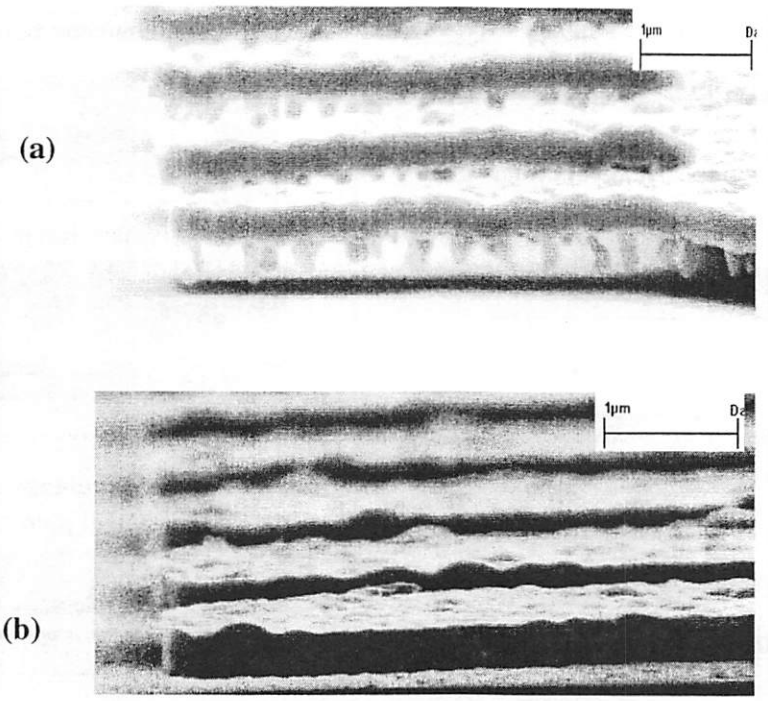

Figure 3-0: (a) High temperature (600C) process induces Si/Ge interaction; (b) a-Si deposition on Ge at 450C prevents formation of SiGe compounds.

3.3.1 Deep sub-micron sacrificial release

During release, the wafers are first dipped in HF to remove etch stop LTO layer from top of the flexure hinge. Ge etch is performed in 90°C water bath containing 30%-hydrogen-peroxide; this method of etch was developed by the BSAC group at UC Berkeley. Without exposure to air (to prevent stiction), we transfer the wafers to methanol and then perform critical point drying (CPD) [3]. The CPD chamber introduces liquid CO_2 that is completely miscible with methanol. Keeping the chamber above 1200psi and below 30°C, we gradually substitute methanol with CO_2. Once this is accomplished, the chamber is closed to heat liquid CO_2 to a supercritical fluid at 35°C (there is no liquid-vapor interface formed during this transition). We vent the chamber above the critical temperature so that the CO_2 continues to exist in gaseous form, thus releasing the mirror.

3.3.2 Germane and poly-silicon diffusion

We have achieved a breakthrough in understanding the cause of structural formations in the mirror gap. Apparently, at polysilicon deposition temperature (around 600C), silicon diffuses in Ge. We have observed "stalactite" structures buried in the Ge film that are not etched in Ge etchant. We interpret these as Ge-Si mixtures caused by diffusion of Si in defective areas (grain boundaries?) in the Ge sacrificial layer. We end up with stalactites like structures protruding from the mirror underside (please see Figure 3-0 (a)). Using an LTO layer to separate the Ge and Si layers prevents the Si diffusion into Ge, and the structures are released cleanly, as seen in Figure 3-0 (b). Having understood this phenomenon that had been plaguing our devices for nearly a year, we wanted to find a low temperature Si deposition method. This is necessary because in the full mirror fabrication process, Ge is sandwiched between α-Si hinge and poly-Si bottom electrode layers; hence, diffusion of Si atoms into Ge is detrimental to successful device fabrication. Depositing silicon at a lower temperature is an obvious choice. To achieve a reasonable deposition rate at lower temperature we have switched deposition gas, from silane (SiH_4) to disilane (Si_2H_6). Eventually the disilane process was set aside for reasons explained next.

3.4 Process issues

Conductive layer: In choosing a process flow, we are guided by the twin principles of achieving low sheet resistance at a low thermal budget. The structural layer is connected to the flexure through an anchor. Both need to have low resistivity. We can deposit polysilicon at 600C with a dopant, however, that is above our target temperature of 450C

and it adversely interfaces with germanium, as seen above. Low temperature silicon deposition can be accomplished with a disilane gas, however, because of its amorphous nature, it is not suitable.

We found that a gas flow of 50sccm germane with 100sccm silane, 60sccm diborane at 800mTorr and 450°C gives us about 55% germanium content a-SiGe layer. It is both conductive and has an acceptable deposition temperature. Film resistivity was found to be between 0.2-0.3 ohm-cm.

Bonding: In order to actuate the mirrors, we need to drive the mirror electrodes from an external source. Wire bonding was probably the most cumbersom aspect of the fabrication. Because the structures are fragile, exposing them to the wirebonding process inevitably caused snap-down. It helped if an HF clean of the devices was done just prior to the post-release critical point drying step.

Ge roughness: Germanium deposition is highly rough. It was eventually discovered that a recipe using higher pressure can lower the deposited film rougness.

3.5 Stress measurement

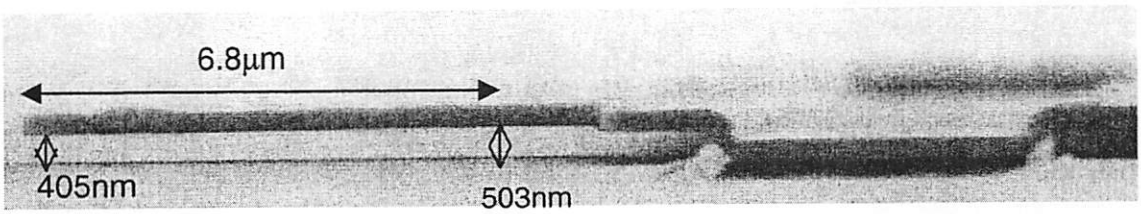

Figure 3-0: Cantilever beam to study stress

Stress of flexure determines the initial mirror tilt and is also responsible for variation in mirror positions across the chip. Stress induced tilt should be minimized. In-plane stress measurements of the as-deposited films were made using the wafer curvature technique, with Flexus. With this technique, the film stress, s, is determined from the measured change in radius of curvature, R, of the thin substrate using Stoney's equation [4]:

$$\sigma = \frac{1}{R}\frac{E}{6(1-\nu)}\frac{T^2}{t}$$

where t is the film thickness, T is the substrate thickness, and $E/(1-\nu)$ is the biaxial elastic modulus of the substrate (which is related by $Ys=E/(1-\nu)$ to Young's modulus, E, and Poisson's ratio, ν, for the substrate.) Substrate thicknesses were measured with a micrometer, and film thicknesses were determined using an ellipsometer. With the wafer-curvature apparatus, the deflection of a HeNe laser beam is measured as it is scanned along the substrate surface, and the deflection is used to compute the substrate radius. Measurements made on the substrate before film depositions are used to determine figure errors and thickness variations in the substrate which are then subtracted from subsequent measurements to improve the measurement accuracy. The net precision of the film stress

measurements is estimated to be approximately ±5% largely due to variation in wafer thickness measurement.

Thickness dependent stress variations in thin films such as hinge layer can be detrimental to mirror functionality. Study of stress evolution with thickness did not reveal a stress gradient. Bulk stress for polysilicon film thickness of 210nm, 150nm, and 83nm gave stress values of (-279), (-253), and (-251) MPa (compressive). Bulk stress for a-Si deposited with disilane gas in an LPCVD furnace was compressive at –170MPa for 2kA and 3kA thick films, indicating lack of a stress gradient. LTO stress was also compressive at –175MPa. Figure 3-3 shows a sideview of a released 7um long cantilever beam that is composed of a triple layer stack with 300nm a-Si mirror on top, 80nm LTO layer in the middle, and a 55nm a-Si hinge layer at the bottom. The beam shows only a slight tilt (0.8^{o}) confirming that stress gradient is indeed minimal.

3.6 Results (SEMs of working mirrors)

Figure 3-0 (a-c) show SEMs of released structures with mirror surface area ranging from $400\mu m^2$ to $1\mu m^2$ and the gap varying from 900nm down to 340nm. Use of CO_2 based critical point drying is crucial in getting functional devices. Surface roughness of germanium leaves mirrors non-smooth; therefore, a chemical-mechanical-polish (CMP) step is necessary after mirror deposition. EUV lithography imposes stringent requirements on the reflective masks' surface roughness [5]. Chemical-mechanical polish (CMP) of the polysilicon mirror surface (on which EUV layers would be sputtered) can help meet this requirement. Surface characterization using AFM technique shows mirror

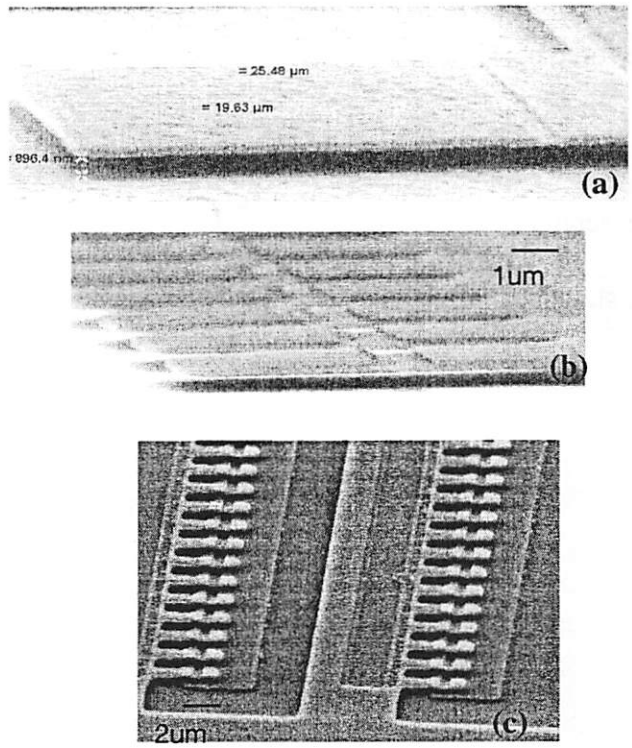

Figure 3-0: Released mirrors (a) 20x20µm mirror, 900nm gap (unpolished); (b) 5x5µm array, 340nm gap; (c) 1x1µm array, 340nm gap.

roughness has been reduced from 11nm to 1.79nm ra. Post-release, the mirror roughness remains virtually unchanged at 1.66nm rms.

In the fabrication process, we have been limited by the optical resolution offered by the I-line stepper at the UCB microlab. Static and dynamic mirror characterization of these mirrors has not been carried out but a more stable mirror design is currently being fabricated in the recently operational high resolution DUV stepper at the UCB microlab.

This design uses a hidden hinge for high fill-factor ratio and a vertical comb-drive for higher drive force per area[1].

In the next few figures, SEM images of fully released micromirrors are shown. Mirror deflection is seen, despite the fact that no deflection voltage is applied. The deflection is attributed to static charge, deposited by the SEM beam.

[1] Yijian Chen, personal comments.

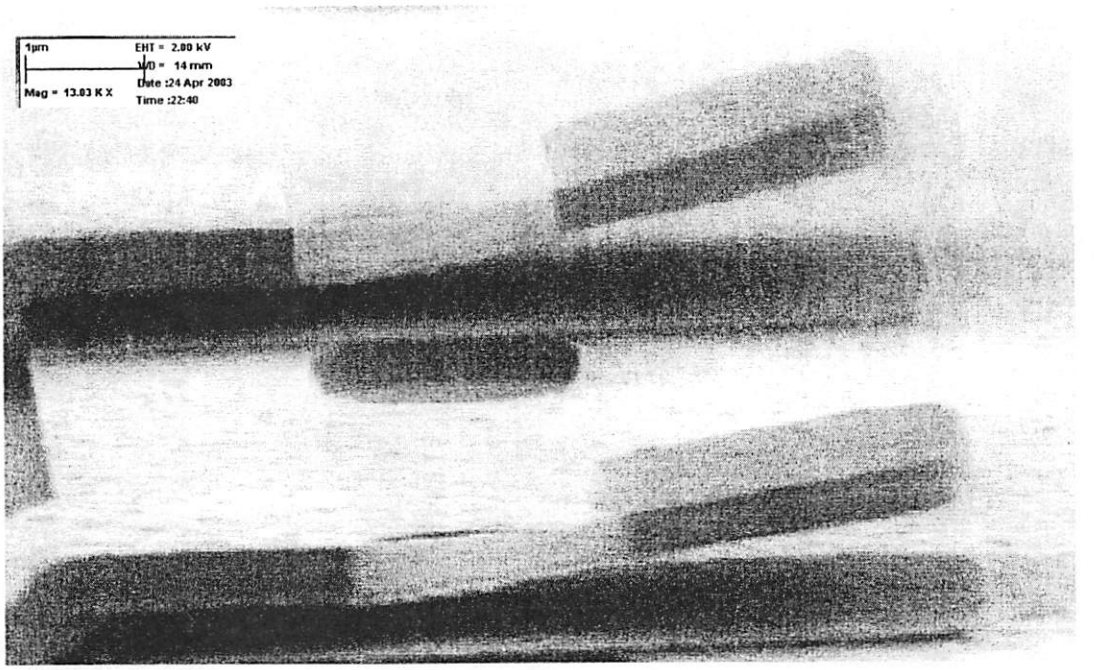

(a) Semi-dense 3x3µm^2 mirror array. Mirrors began to rise due to charging from e-beam of the SEM.

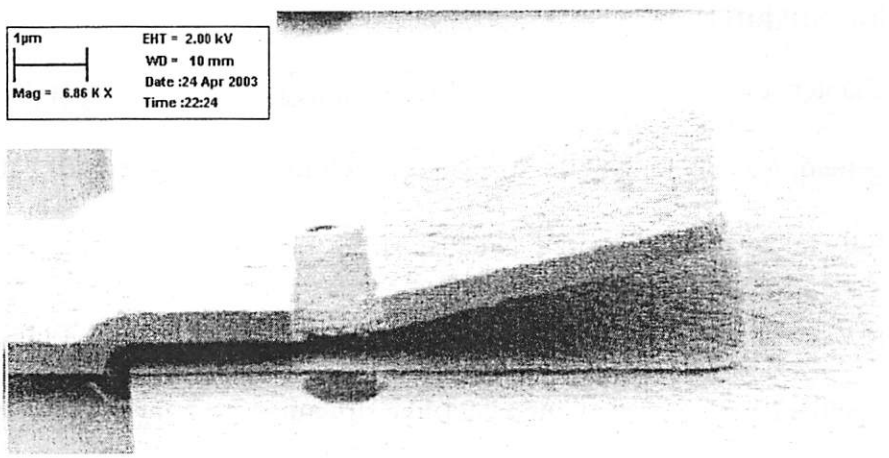

(b) An isolated 3x3µm^2 mirror

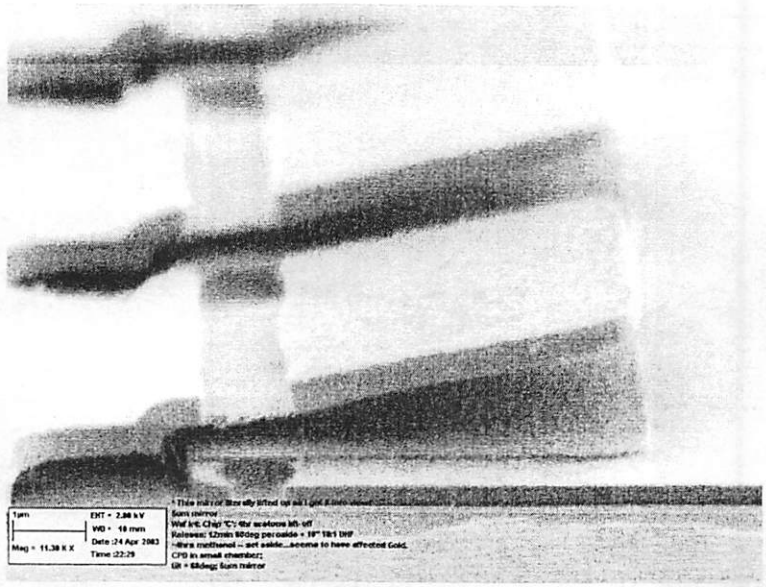

(c) A 5x5 μm^2 dense mirror array released.

Figure 3-0: SEM of structures lifted due to e-beam charging

3.7 Conclusions

In this chapter, the fabrication methodology of mirrors based on a parallel-plate design was presented. Mirrors ranging in size from 3 to 5 μm on an edge with 250nm gap were successfully released and observed under SEM.

Interaction between sacrificial Ge and structural poly-Si was shown at high temperature, resulting in the creation of dangling wafer like structures from the released beam. Moving to a low temperature process with disilane allowed full release of the structure. However, because of the new temperature/pressure conditions, the silicon mirror and flexure were amorphous, and hence, non-conductive. Introduction of Germane gas with diborane helped achieve reasonable deposition rate and also conductive films. Since the Ge content

in the resulting film is less than 60% preventing it from getting etched by Ge etchant, we have been able to continue using Ge as a sacrificial layer.

Ge deposits as a relatively rough layer, which might affect final device reflectivity. Therefore, a CMP step was added at the end. AFM measurements indicate that CMP could be used to meet the mirror roughness requirements and the release process is benign to SiGe mirror smoothness.

In conclusion, we have a low thermal budget process that provides conductive structural films for mirrors and the release process is proved to work. Electrostatic characterization of the mirrors has not been carried out because of metal bonding issues with the top film. Metal (Al or Au) sputtering on the existing wafers can allow bonding. Existing interferometry tools can be used to determine mirror tilt as a function of applied voltage, however, because of the small lateral geometry involved, characterization may yet be a formidable task.

3.8 References

[1] N. Choksi, Y. Shroff, et. al, "EUV maskless Lithography", JVST, Nov. 1999.

[2] Franke, A. E.; Bilic, D.; T-S. King, et. al., "Post-CMOS integration of germanium microstructures," MEMS99, Orlando, CA, January 1999, pp. 630-7.

[3] Michael Houston, "Sacrificial release of MEMS devices", PhD thesis, UC Berkeley, 1996.

[4] G. G. Stoney, *Proc. Roy. Soc. Londo*n, A82, 172-175 (1909).

[5] M. Wedowski, J.H. Underwood, E. Gullikson, et. al., "High-precision reflectometry of multilayer coatings for extreme ultraviolet lithography", SPIE, vol. 3397, 83-93 (2000).

4 Pattern generation using nanomirror arrays

4.1 Analytical waveform representation

There are two motives for this study: to understand how analog light modulation works at different *NA* and to determine how we can use each design in a diffraction limited optical system. Primarily, micromirrors modulate reflected light using two different mechanisms accomplished by tilting mirrors and phase-shift mirrors. In this section, our goal is to develop an intuitive feel for the way mirror based pattern generation works using analytical representation of the way these images are formed. This analysis is best done in frequency space, hence, the first section will look at developing a Fourier Transformation of the object plane using tilting and piston mirrors. For throughput reasons, we need to modulate the intensity of every pixel in every light flash.

In the second half of this chapter, we cover actual pattern generation with nanomirrors. Grayscaling requirements and linewidth resolution dictate the interplay between various parameters of optical lithography. Maskless adds a few more, such as grayscaling bits and spot resolution. We use image slope as a primary method of quantifying images and all images are generated at best focus in this chapter.

4.1.1 Diffraction grating: Tilt mirrors

The coherent field distribution of a Fraunhofer diffraction pattern produced by a mask is essentially the Fourier transform of the mask function. If we let $U(x,y)$ be a two-dimensional mask function or electric field distribution across the x-y mirror plane and let $G(fx,fy)$ be the coherent field distribution across the (fx,fy) Fraunhofer diffraction plane, then [6]

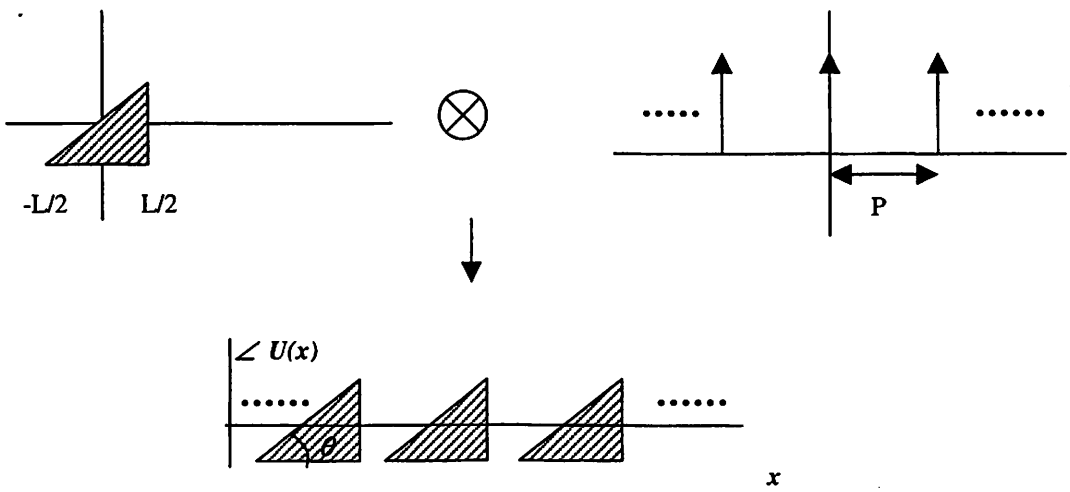

Figure 4-0: Sawtooth waveform is created by convolving a unit mirror element of length L with a comb function of pitch P.

$$G(f_x,f_y)=F\{U(x,y)\}$$

We need to obtain an analytical representation of a tilted mirror array where all the mirrors are tilted at the same angle given by θ. Consider a mirror of dimension (a,b) at origin in (x_o,y_o) plane with light incident at normal. Suppose that a monochromatic light source is illuminating an array of tilted mirrors. The incident wave is a plane wave coming in at normal incidence. The mirror array reflects a complex field represented by U(x). For simplicity, we can consider a one-dimensional array of mirrors, tilted in the x direction. Our ultimate objective is to calculate the resulting field $U(x')$ that appears across a second, parallel plane, at the focal plane of the imaging lens.

A mirror element can have a certain thickness function $\Delta(x,y)$ where (x,y) are the transverse coordinates on the face of the mirror. A plane wave reflecting from a surface at an angle θ is given as by the following equation:

$$p(x) = \exp(j*k*x*\sin\theta) \qquad \textit{Eq. 4-1}$$

As shown here, since it is infinite in either direction, we need to prune it using the well-known *rect* and *comb* functions as described below:

$$\text{rect(x)} = \begin{cases} 1 & |x| < ½ \\ ½ & |x| = ½ \\ 0 & \text{otherwise} \end{cases} \quad \textbf{\textit{and}} \quad \text{comb(x)} = \sum_{n=-\infty}^{\infty} \delta(x-n)$$

E-field due to a single mirror element positioned at the origin can now be described as:

$$U_{mirror} = p(x) * \text{rect(x)}$$

$$\Rightarrow U(x) = e^{jkx\sin\theta} \cdot \text{rect(x)} \qquad \textit{Eq. 4-2}$$

Now consider a whole set of mirrors (1-D array) given by convolving the mirror function with a comb function:

$$U_{array} = U_{mirror} \otimes \text{comb(x/P)} \qquad \textit{Eq. 4-3}$$

Let $G(f_x;0) = F\{U_{array}\}$. The function U_{array} has a Fourier Transform given by

$$G_{array}(f_x;0) = F\{U_m\} \cdot F\{\text{comb(x/P)}\} \qquad \textit{Eq. 4-4}$$

Concentrating on the first half of the above tranform and using $G_m(f_x;0) = F\{U_m(x)\}$, we have:

$$G_m(f_x;0) = \int_{-L/2}^{L/2} U_m(x)\exp[-j2\pi(f_x x)]dx$$

$$\Rightarrow G_m(f_x;0) = \int_{-L/2}^{L/2} \exp[jkx\sin\theta]\cdot\exp[-j2\pi(f_x x)]dx$$

$$\Rightarrow G_m(f_x;0) = \int_{-L/2}^{L/2} \exp[j(k\sin\theta - 2\pi f_x)x]dx$$

$$\Rightarrow G_m(f_x;0) = \frac{1}{j(k\sin\theta - 2\pi f_x)} \cdot 2j\sin\left[\tfrac{L}{2}(k\sin\theta - 2\pi f_x)\right]$$

After several additional steps, we can obtain the following representation of a tilted mirror in frequency space:

$$G_m(f_x;0) = L \cdot \mathrm{sinc}\left[\frac{L}{2}\left(\frac{k\sin\theta}{\pi} - 2f_x\right)\right] \qquad \textit{Eq. 4-5}$$

The Fourier Transform of a comb(x) function is simply a comb function. However, if we look at only a set of N mirrors, we have the following transform, using a delta-function representation of the comb function:

$$G_{comb}(f_x;0) = F\left\{\sum_{n=-(N-1)/2}^{(N-1)/2}\delta(x_o - nP)\right\}$$

The *shift-theorem* states that translation in space domain introduces a linear phase shift in the frequency domain. Using this property of Fourier Transforms, we can simplify the above equation as:

$$G_{comb}(f_x;0) = \sum_{n=-(N-1)/2}^{(N-1)/2}\exp[-j2\pi(f_x \cdot n \cdot P)]$$

Again, we can simplify the above equation by using various transcendental function identities:

$$G_{comb}(f_x;0) = \frac{\sin[f_x \cdot N \cdot P \cdot \pi]}{\sin[f_x \cdot P \cdot \pi]} \qquad \textit{Eq. 4-6}$$

The complete Fourier Transform of an N mirror array, $G_{array}(f_x;0)$, is represented as:

$$G_{array}(f_x;0) = G_m(f_x;0) \cdot G_{comb}(f_x;0)$$

$$\Rightarrow G_{array}(f_x;0) = L \cdot \mathrm{sinc}\left[\frac{L}{2}\left(\frac{k\sin\theta}{\pi} - 2f_x\right)\right] \cdot \frac{\sin[f_x \cdot N \cdot P \cdot \pi]}{\sin[f_x \cdot P \cdot \pi]} \qquad \textit{Eq. 4-7}$$

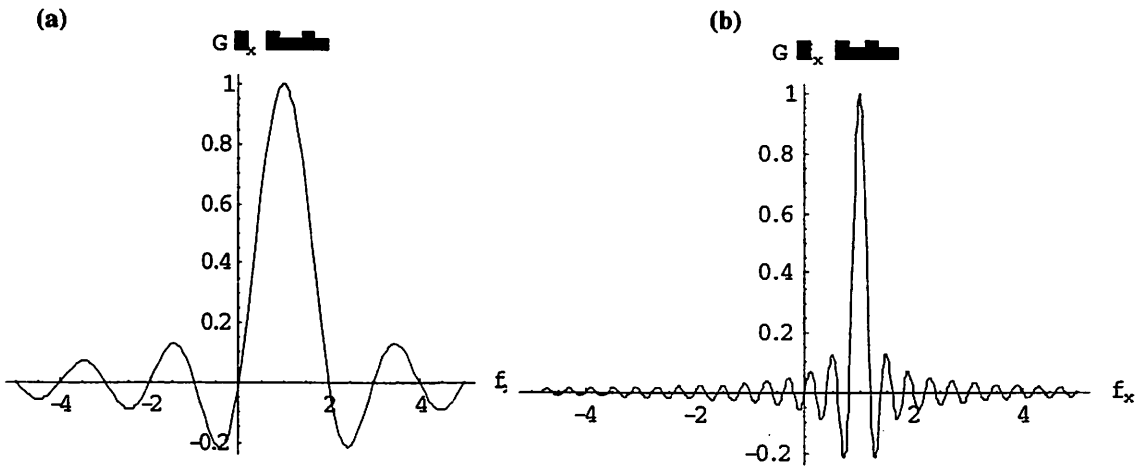

Figure 4-0: (a) Frequency space representation of a centrally tilted single mirror to an angle corresponding to ½ λ OPD, (b) and 5 mirrors tilted to the same angle. Frequency, f_x, is normalized to (NA/λ).

The peak of a single mirror diffraction coincides with a delta point of the comb function for certain angles of reflection. Apart from the dull case of zero tilt (where all the energy is simply reflected into the 0th order), peak intensity of the above figure (a) moves to the left or right depending on the tilt direction and angle. If the *NA* at the mask side is designed to be small enough and 2 or more mirrors are tilted, we could deflect light completely out of the pupil, creating a dark spot at the wafer. In Figure 4-0 (a), diffraction due to a single mirror is shown. Figure 4-0 (b) shows the frequency spectrum representation of N=5 mirrors tilted such that all the energy is deposited in the first order. In the extreme that N approaches infinity, the FWHM of the pulse will approach zero as

the array of tilted mirrors (akin to a diffraction grating) redirect all energy into a single frequency component that is not captured by the pupil.

We will, in general, choose (*NA*, *L*) combinations where the width of the central lobe exceeds the pupil diameter. In other words, $L*NA/\lambda \leq 0.25$, and therefore a single mirror is not resolved. However, when a few mirrors are similarly tilted (as seen in Figure 4-0 (b)), larger fraction of light is re-directed to the (NA/λ) order which leads to better contrast. We now have an analytical understanding to answer why using more mirrors per minimum feature is better for image fidelity, however, we are constrained by data throughput limitations.

Figure 4-0 shows that as the mirrors are tilted, energy from the DC component of the frequency spectrum is shifted to the first order. As a result, the amount of light captured by the limited *NA* optic is reduced to null for tilt corresponding to an optical path difference of $\lambda/2$ between the center and edge of the mirrors.

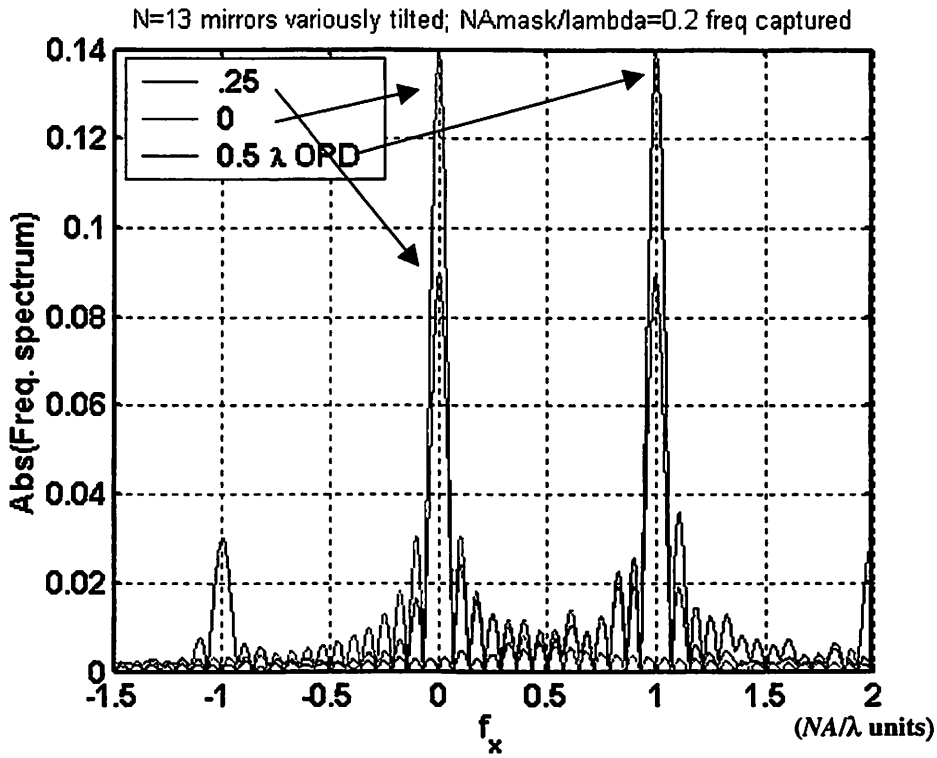

Figure 4-0: The arrows point to the peak for each curve. For 0lambda tilt, most of the light is directed to the center of the pupil (DC). As the OPD increases to 0.5lambda, the central lobe shift to 1NA/lambda (outside the pupil capture range); for an intermediate tilt, the mirror is "half-on, half-off' with e-field distributed between the zeroth and first orders.

4.1.2 Diffraction grating: Piston mirrors

A step function in phase will redirect light at an angle as shown in the following series of expressions.

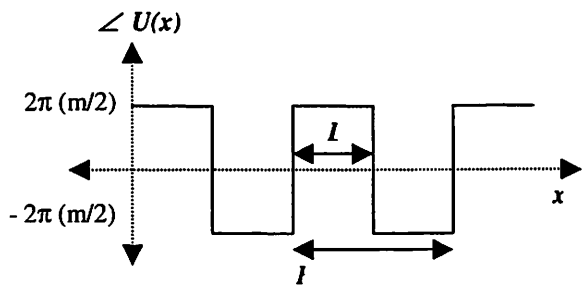

Figure 4-0: Phase representation of alternatively shifted phase

Let U(x) represent a 1-D unit amplitude transmission plane with a phase step as seen in the above figure.

The special case of zeroth-order diffraction efficiency is given by

$$\eta_0 = \left[\frac{L}{P}\right]^2 \cdot 4\cos^2(m\pi)$$

The q^{th}-order diffraction efficiency is given by:

$$\eta_q = \frac{1}{(n\pi)^2} 4\sin^2\left[\frac{L}{P}q\pi\right] \cdot \sin^2(m\pi)$$

If $L=P/2$ (50% duty-cycle), then null intensity in zeroth-order is received for

$$\eta_0 = \left(\frac{1}{2}\right)^2 4\cos^2(m\pi) = 0 \text{ for } m = 1/2$$

Thus, for optical path difference to correspond to m=1/2, we need alternating mirrors phase shifted by λ/2 to achieve null intensity in the zeroth-order. As the section on optical imaging will make it clear, it is also important that the numerical aperture of the system is small enough to cut off higher frequency components.

An arrangement of alternating up and down piston mirrors can mathematically be represented by a convolution of a unit mirror function and comb function, similar to the analysis presented in the tilt mirror section. A plane wave reflecting from the surface of two half piston-mirrors at phase (+/- θ) from normal is given by:

$$p(x) = \begin{cases} \exp[-i\theta] & ;-L/2 < x < 0 \\ \exp[i\theta] & ;0 < x < L/2 \end{cases} \qquad \textit{Eq. 4-8}$$

Mask spectrum of a unit element described in the above formulation is given as:

$$G_{piston} = \int_0^{L/2} \exp(i\theta)\cdot\exp(-i2\pi fx)dx + \int_{-L/2}^{0} \exp(-i\theta)\cdot\exp(-i2\pi fx)dx \qquad \textit{Eq. 4-9}$$

This integral is easy to calculate and can be simplified to the following form:

$$G_{piston} = \frac{1}{\pi f} 2\cos(L\pi f/2 - \theta)\sin(L\pi f/2) \qquad \textit{Eq. 4-10}$$

An array of such mirrors can be represented as

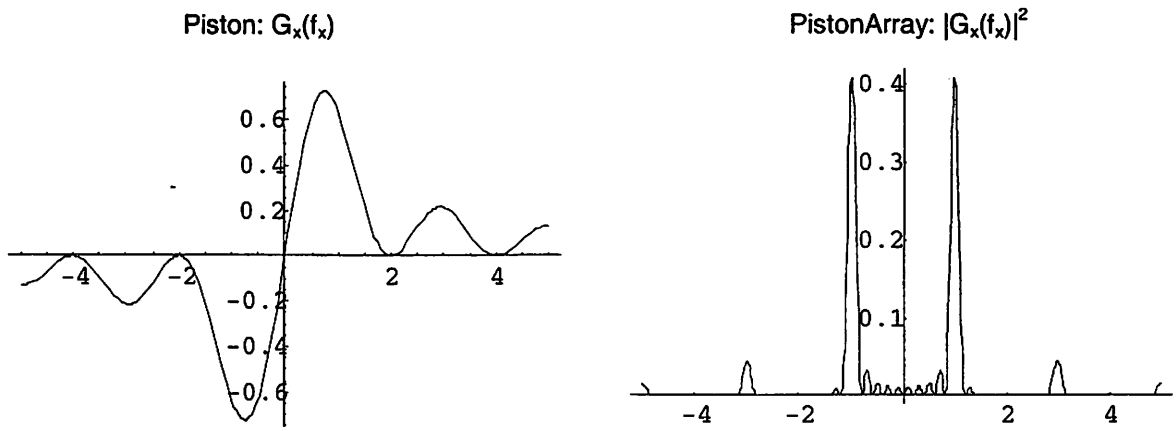

Figure 4-0: (a) Normalized spectrum of a two piston mirrors phase displaced by (+Pi, -Pi); (b)Amplitude spectrum of N=5 array of alternating piston mirrors.

$$G_{PistonArray} = \frac{2N}{\pi f}\cos(L\pi f/2 - \theta)\cdot\sin(L\pi f/2)\cdot\frac{\sin(fNP\pi)}{\sin(fP\pi)} \qquad \textit{Eq. 4-11}$$

Figure 4-0 (a) shows the spectrum of two piston mirrors of width L/2 displaced by (+θ, -θ) from normal. (b) shows an array of 5 such mirror pairs.

4.1.3 Lens

The information to be Fourier-transformed is introduced into the optical system by the spatial light modulator that controls the amplitude transmittance in response to externally supplied electrical information. In practical systems, the image will be demagnified by the optics (for e.g., the mirror size is ~1μm, and the pixel size is ~10-20nm in the EUV). We characterize the optical system by two key parameters: degree of demagnification (M) and numerical aperture (*NA*).

The total e-field is calculated by summing all the frequencies reaching a given point in the image plane (x_i,y_i).

$$U_i(x) = \iint_{(-\infty,\infty)} P(f)\cdot G(f)\cdot \exp[-j2\pi(f\cdot x)]df$$

For a circularly symmetric aberration-free optical system typical in photolithgraphy, the

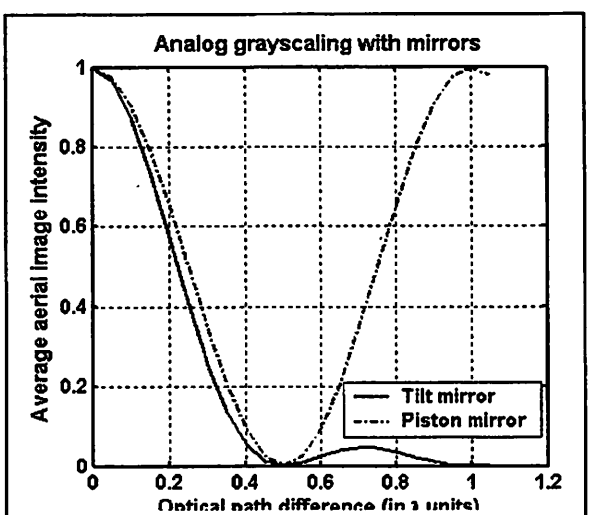

Figure 4-0:Analytically derived grayscale chart for tilt and piston mirrors.

pupil function, P(fx,fy), is similar to a low pass filter that allows only lower frequency components to go through to the imaging plane:

$$P(f)=\begin{cases}1 & \text{if } \sqrt{f_x^{\,2}+f_y^{\,2}}=\nu\le\frac{NA}{\lambda}\\ 0 & \text{otherwise}\end{cases}$$

Using the pupil function restriction in the e-field summation, we can write the e-field and intensity distributions as:

$$U_i(x)=\iint\limits_{\nu<NA/\lambda} G(f)\exp[-j2\pi(f\cdot x)]df$$

$$I_i(x)=\left|\iint\limits_{\nu<NA/\lambda} G(f)\exp[-j2\pi(f\cdot x)]df\right|^2$$

Using the above formulation, we can rewrite the tilt and piston mirror spectrum by using the appropriate mask spectrum, *G(f)*. The adjacent figure shows that the aerial image intensity for varying degrees of tilt will be null for angle corresponding to optical path difference (*OPD*) of λ/2 between the center and edge of mirrors, in case of tilting mirrors. For piston mirrors, we get null intensity when the *OPD* between two adjacent mirrors is λ/2.

4.2 Implementation

In this section, we present a preliminary study of the pattern generation capabilities of both types of light modulators. The two mirror architectures are compared with each other and with images generated from a simple binary mask under varying conditions of illumination, numerical aperture (*NA*), and feature density. In the piston modulation method, the mirrors move normal to the modulator plane with the resulting diffraction

creating the desired aerial image at the wafer plane [1]. With tilting mirrors, the image intensity is varied with tilt angle and has a null when the edge of the mirror is dephased from the center by a quarter wave (reflected light Optical Path Difference or *OPD* of half wave) [2]. Phase modulation (achieved for example by overtilting adjacent mirrors) is studied in the next chapter to further improve the aerial image quality.

In the next section, we describe the principle of operation of these electrostatically actuated mirror devices in terms of grayscaling. Concepts such as number of spots per minimum feature, grayscaling, and measurement metrics necessary for pattern generation are also reviewed. Several types of 1-D patterns, such as wide and narrow features, edge placement, dense lines are generated using both mirror designs and the results are compared with binary mask images. Finally, we discuss the merits of each light modulation scheme with respect to optical system wide parameters and arbitrary edge placement constraints.

4.3 Arbitrary pattern placement

Substitution of an array of mirrors for a mask leads to discrete placement of pattern edges on a grid at the wafer plane. However, the desired printed pattern is usually based on a virtually gridless design. To print arbitrary patterns, that is, with edges that fall anywhere within the mirror grid, we need to use grayscaling, which allows sub-pixel increment of feature width. Increasing the number of spots per minimum feature (i.e. a finer grid) increases the volume of pattern data we need to handle as the inverse square of the mirror size. Previous studies by designers of maskless writing systems have shown that two to

three spots are adequate to print a minimum feature and to permit fine-scale edge placement with grayscaling.

Grayscaling can potentially be achieved by digital or analog mirror modulation. In the former case, mirrors are fully turned 'ON' or 'OFF' and the *on-state* duty cycle is varied to modulate the light intensity at a given wafer spot. In the analog mode of operation, the mirrors are turned 'ON' partially so that the flux hitting a given spot is a function of mirror position. Both approaches are valid; however, for operation with a pulsed light source such as an eximer laser, analog mode of operation is required. Five or more bits of positioning information are typically needed.

4.4 Mirror Architectures: Principles of operation

To eliminate the magnification variable, mirror size is given in wafer-plane dimensions. We call this the *"spot"-sizes.* While the mirrors are not necessarily resolved at the wafer-plane, thinking of patterns in terms of the spot-size, *s*, allows us to think in terms of a *grid* and the related pattern displacement issues at the wafer plane.

Tilt: In the *tilt* architecture, light reflected from a mirror in the *fully*-'ON' state goes through the pupil and essentially lights up a spot as it is focused at the wafer plane[1]. Tilting the mirror attenuates the light intensity at that spot, eventually resulting in a null-intensity at the corresponding spot on the wafer. The tilt of the mirrors is specified in terms of the optical path difference (measured in units of wavelength, or λ). For the tilting case, *OPD* is twice the displacement from the center to the edge of the mirror, as shown in Figure 4-0(a).

$$OPD \equiv s * \sin(\theta)$$

Figure 4-0(b) is a plot of average aerial image intensity as a function of *OPD* for an array of mirrors tilted simultaneously to varying angles. A practical implementation of this architecture for laser-based mask writing has been demonstrated with data by Micronic [2]. It can be generalized to show that for sub-resolution mirrors, we have optimum "null" intensity with $OPD = \lambda/2$. Mirror tilt with intermediate *OPD* allows grayscaling.

Piston: In this architecture, the mirror array operation is analogous to patterning with a pure chromeless phase-shift mask, with the added advantage that we have the capability to achieve any phase between 0 and 180 degrees due to analog translational motion of the mirrors. This architecture is similar to that used by Silicon Light Machines, whose Grating Light Valves are based on interference effects [3] although with CW light sources in a scanning mode.

[1] Of course, for a typical structure where $s<0.25\lambda/NA$ a single spot is not resolved.

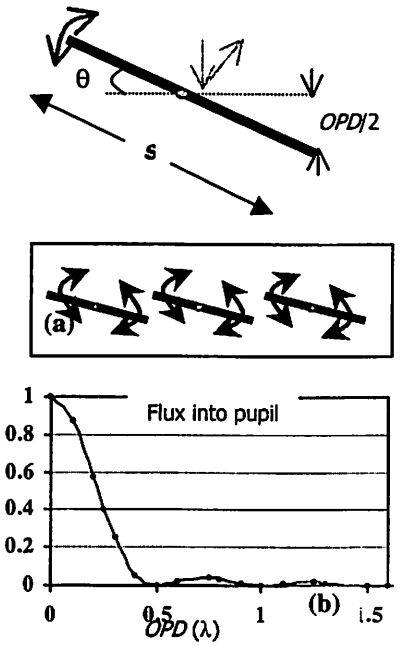

Figure 4-0: (a) Cross-section of a tilted mirror of size s; (b) flux at the wafer-plane as a function of OPD of a mirror array.

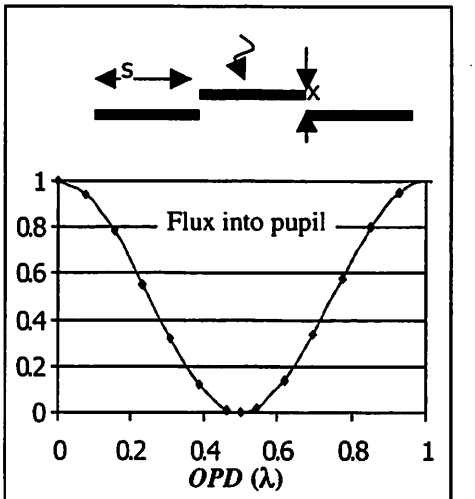

Figure 4-0 (b): Flux into the wafer plane as a function of the OPD of alternating piston-mirrors.

Figure 4-0(b) shows an array of reflective piston mirrors. As with tilt, the position of piston mirrors is measured in terms of *OPD*. For reflective mirrors,

$$OPD \equiv 2x,$$

where x is the displacement of the mirror normal to the modulator plane. Again, at the bottom of Figure 4-0(b) we plot the average intensity produced by varying the optical path difference of alternating mirrors. If set-up correctly, an *OPD* of $\lambda/2$, i.e, mirror displacement of $\lambda/4$ provides null reflection in the zeroth order. As with tilt, we control the dose by choosing an *OPD* between 0 and $\lambda/2$. Dose control naturally leads to grayscaling of spot-intensity at the wafer plane.

a. Optical system parameters

For a given illumination coherence, σ, the results are generalized to two simple parameters: the familiar lithography metric, k1, and a new parameter specific to pixel based imaging, k1spot. The parameter k1spot essentially describes the capability of our imaging system to resolve an individual mirror and is defined by:

$$k1_{spot} \equiv s/(\lambda/NA)$$

Here s is the spot size and it refers to the *mirror* size demagnified to the wafer plane. *NA* is the numerical aperture and λ is the wavelength of illumination. For large $k1_{spot}$, the mirrors are resolved. To guarantee that the individual mirrors are not resolved requires $k1_{spot} < 0.5/(1+\sigma)$, where σ is the pupil fill. If we operate in the neighborhood of 2 spots per minimum feature, then we want to resolve 2 spots but not one. Thus $0.15 \tilde{<} k1_{spot} \tilde{<} 0.35$ for σ in the range of 0.3 to 0.6.

Choosing #spots/MFS: Image fidelity improves with the number of spots used for printing a minimum feature. On the other hand, the amount of data the system needs to handle increases rapidly too. For instance, in order to print a 12" wafer per minute with a CD of 100nm and 2 spots/MFS with 5-bit grayscaling the maskless system requires a throughput of 10Tb/sec. With 4 spots per minimum feature, this number quadruples. The actual number of spots used to resolve a minimum feature is calculated as

$$\#spots/MFS \equiv k1/k1_{spot}$$

Here k1 is a measured quantity defined as:

$$k1 \equiv FeatureSize_{measured} / (\lambda / NA)$$

The feature width is measured at an intensity threshold, I_{th}, *of 30%.*

Quantifying image quality: Normalized image log slope (NILS) is used to determine the "quality" of the aerial image. NILS is given as:

$$NILS \equiv \frac{FeatureSize_{measured}}{I_{th}} \times \frac{\partial I}{\partial x}$$

As before, $I_{th} = 0.3$ is the intensity threshold at which NILS is calculated for a normalized aerial image.

Critical parameters: A maskless lithography system has several parameters that have been discussed so far, such as: *NA*, wavelength (λ), mirror size, magnification, number of mirrors used to print a minimum feature, and coherence of illumination (sigma). Using the above simplifications, these factors can be collapsed into just three parameters: k1, $k1_{spot}$, and sigma.

b. Imaging performance

The gamut of 1-D patterns that are conventionally printed on a mask is potentially infinite. However, we can judiciously select key patterns to achieve some insight into the printing capability of mirror designs. The aerial images are generated using a combination of MatLab™ , SPLAT [4] and JLith[1].

[1] Panoramic Technologies: www.panoramictech.com

4.5 Basic CD adjustment

Figure 4-0 demonstrates grayscaling for CD control of a narrow feature such as a polysilicon line. Two mirrors are set to *OPD* of $\lambda/2$, and the adjacent mirrors are tilted in analog fashion to the *OPD* values given. The simulations are carried out with $k1_{spot}$ = 0.25. Clearly the image quality is not significantly degraded as the CD is increased.

Ideally, we might prefer like a linear relationship between mirror tilt and linewidth modulation, but can deal with any smooth function by means of appropriate modification of the actuation voltage. But it is crucial that there is negligible degradation in line-edge slope.

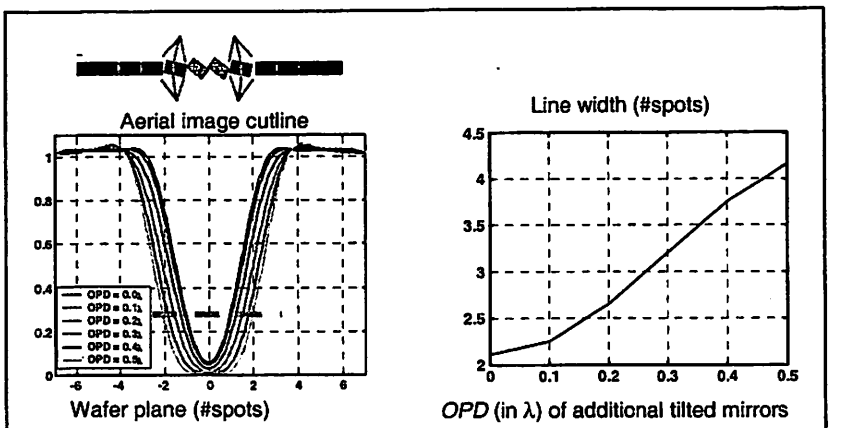

Figure 4-0: Grayscaling for high CD control; ($k1_{spot}$=0.25, σ=0.7)

4.6 Variation with coherence

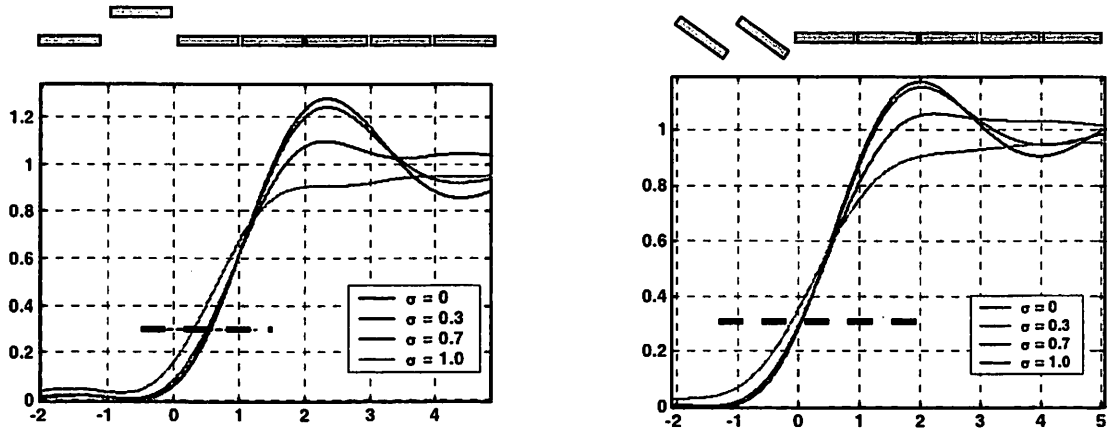

Coherence	0.00	0.30	0.70	1.00
Piston NILS*	4.10	4.04	3.80	3.46
Tilt NILS*	3.50	3.46	3.16	2.62

Figure 4-0: Wide feature -- mirror positions leading to the image are depicted above the charts. Illumination coherence is varied; $k1_{spot}$=0.25

Figure 4-0 shows an aerial image from edge patterns printed with a number of tilted and flat mirrors that are imaged for several sigma values. The edge of the feature is defined by the 30% intensity level where the normalized image log slope, NILS, is computed. Similarly, for the piston case, the flat mirrors fully reflect light while the alternating up/down mirrors define dark regions on the wafer.

We can visualize from this figure the relationship between the feature edges (30% intensity levels) and the mirror edges. The NILS are computed at the measured feature edge. Up to a coherence of 0.7, the line slope is nearly constant in each case, as is evidenced in the adjacent table*. Because we are dealing with a wide feature, the strict

* For a wide feature, an effective NILS is calculated from line slope by defining the effective feature size to be 2 spots.

definition of *normalized* image log slope does not apply. Therefore, we use effective minimum feature size as two spots for calculating NILS for wide feature cases.

4.7 Edge positioning with grayscaling (wide lines)

The preceding chart is ostensibly for feature edge falling on the mirror array imposed grid and may be construed as a best-case scenario. Feature edges can be moved *sub-grid* by modulating the edge mirror from a fully 'ON' to a fully 'OFF' state.

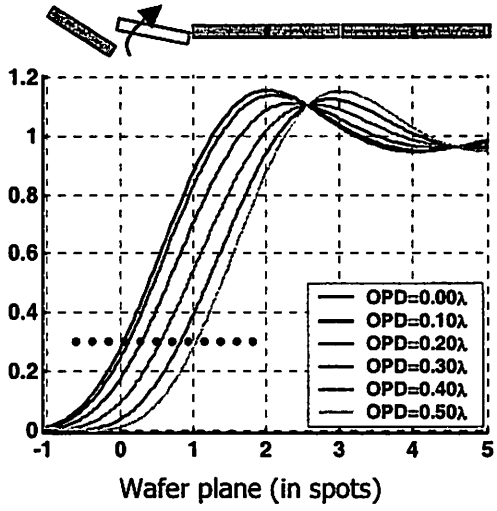

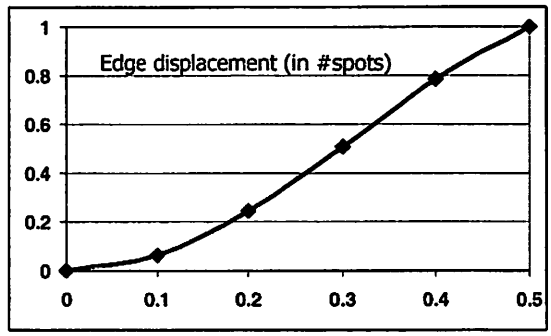

OPD (λ)	0.00	0.20	0.30	0.40	0.50
NILS*	3.46	3.26	3.20	3.28	3.46
Edge Pos	0.00	0.24	0.50	0.78	1.00

Figure 4-0 Edge positioning with grayscaling using tilt approach. $k1_{spot}$ = 0.25; sigma = 0.3

Figure 4-0 shows a family of aerial image cutlines as the edge mirror *OPD* is varied. Notice that the line slope is nearly constant as the feature is displaced. Also, the progression of edge measured in units of spots at the wafer-plane is a smooth function of the mirror *OPD*. In Figure 4-0, we plot a similar edge displacement achieved with piston-mirrors. Again, the image slope is consistent and edge displacement is also a smooth function of mirror *OPD*.

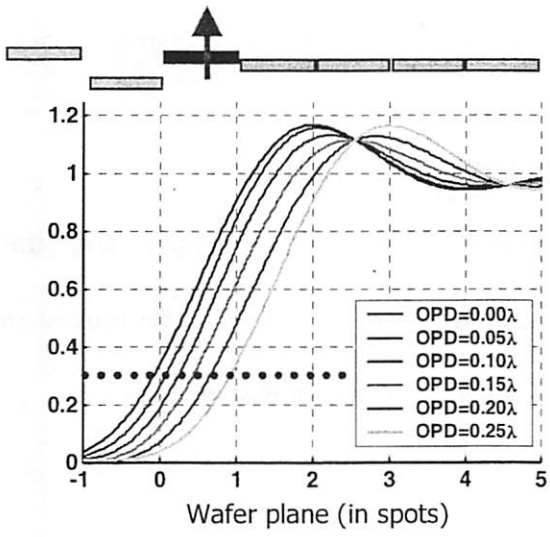

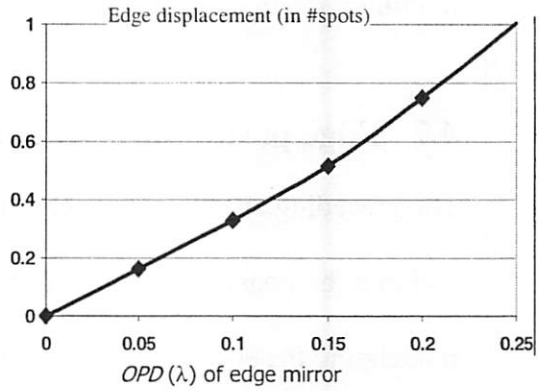

OPD (λ)	0.00	0.10	0.15	0.20	0.25
NILS*	3.16	3.38	3.34	3.30	3.16
Edge Pos.	0.00	0.33	0.52	0.75	1.00

Figure 4-0: Edge positioning with grayscaling: Piston-mirror approach with $k1_{spot} = 0.25$; $\sigma = 0.3$

4.8 Minimum features (isolated)

In this section, we consider imaging arbitrarily placed minimum features (dark features in clear field). The minimum features are composed with two spots. In the simple case of tilt, we move from one grid position to next by adjusting feature end mirrors, as shown inFigure 4-0. In the piston-mirror case, the line moves from one grid position to another as the two active mirrors are vertically displaced. Our measured k1 is close to $2*k1_{spot}$ and $k1_{spot}$ remains sub-resolution.

Using the strategy outlined in Figure 4-0, we can compare the imaging quality of arbitrarily placed minimum features constructed with tilt and piston architectures[1].

[1] Non-optimized since overtilt (the subject of next chapter) is not used.

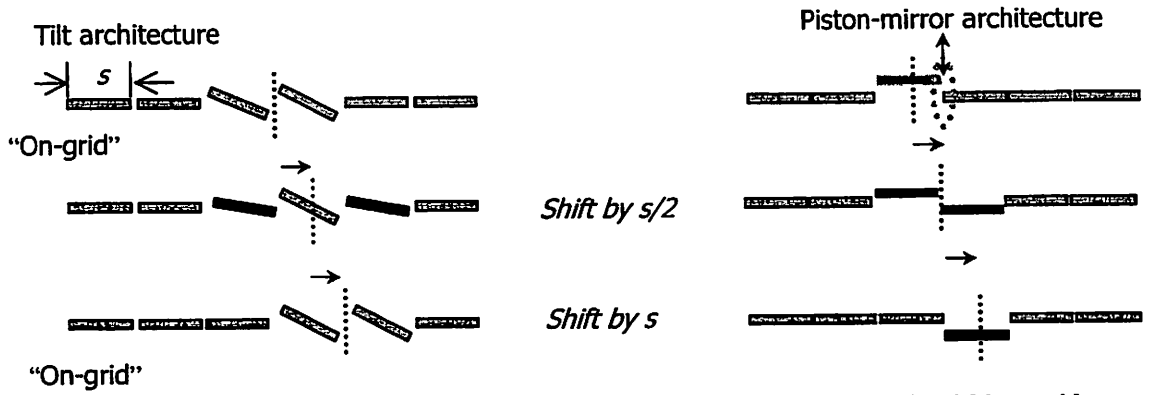

Figure 4-0: Generating a minimum feature and moving it within a grid

Piston: As shown on the left side of Figure 4-0, piston-mirror based minimum features can be moved about the grid with very little change in NILS, which is encouraging. However, there is a slight change in the measured linewidth as the feature is moved off-grid. Fortunately, linewidth compensation is conceptually easy to fix: instead of constant *OPD* between active mirrors, we actually vary the *OPD* slightly to achieve better linewidth control. The result is not only a constant linewidth, but also improved NILS (albeit with a smaller value) with better conformity between the left and right edge slopes of the feature.

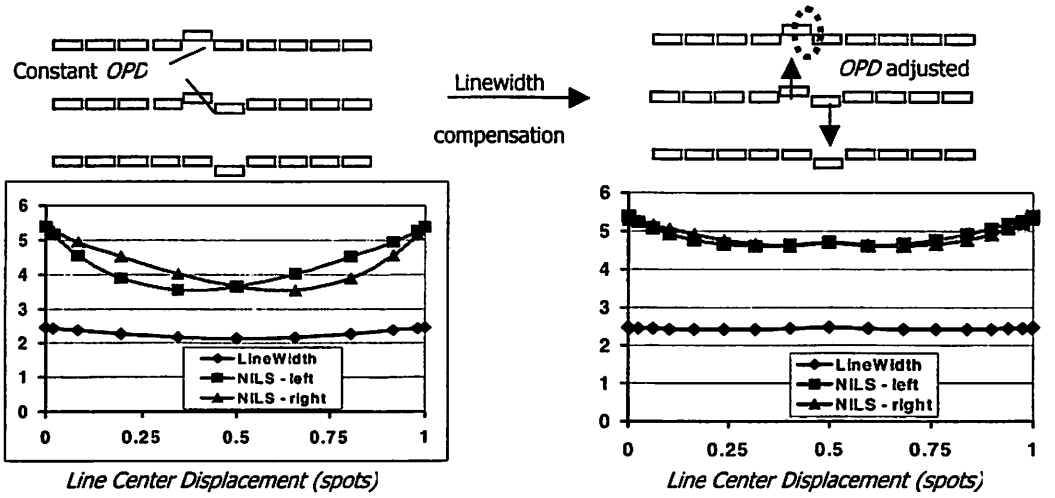

Figure 4-0: Linewidth can be maintained with OPD adjustment, as minimum feature is shifted sub-grid. Optical conditions: $k1_{spot} = 0.25$; $\sigma = 0.3$

Tilt: As with the pure-phase approach, minimum feature displacement using tilting mirrors can be accomplished by modulating two mirrors on either side of a fully OFF spot. The two mirrors move in coordination to place the feature and we 'tweak' the mirror angles to adjust the CD. As seen in the adjacent figure, the image slope is constant within 13%.We find only very slight difference in left and right edge slopes and modest dependence of edge slope on line position.

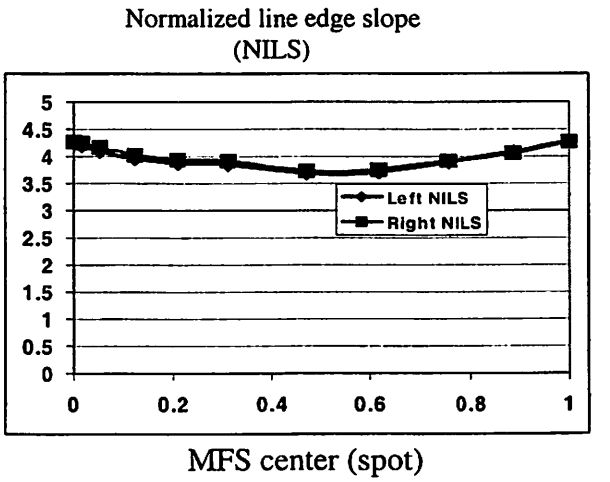

Figure 4-0: Tilt case -- Linewidth control as minimum feature is shifted off-grid; $k1_{spot}$ = 0.25;

σ =0.3; k1=0.6; linewidth constant at 2.4spots.

4.9 Comparing maskless lithography with binary mask imaging

Here we study the image quality of an isolated line, varying *NA* and illumination. The 'image quality' is measured by plotting the normalized image slope of an isolated line as a function of k1. On the top left side of Figure 4-0, we show a cut-line of a minimum feature created with conventional binary mask, and piston and tilt mirrors. By varying $k1_{spot}$ ("printability" of a spot), we can change both the image slope of the resulting line as well as the k1 ("printability" of a minimum feature). A plot of image slope as a function of k1 allows a rough comparison of each patterning methodology. From the above figure, it is clear that for varying coherence of illumination, pattern generation by piston (pure-phase) mirrors can provide better images than binary masks at a given operating k1-factor. Tilt mirrors, on the other hand, perform similarly to binary masks (again, no overtilt is used).

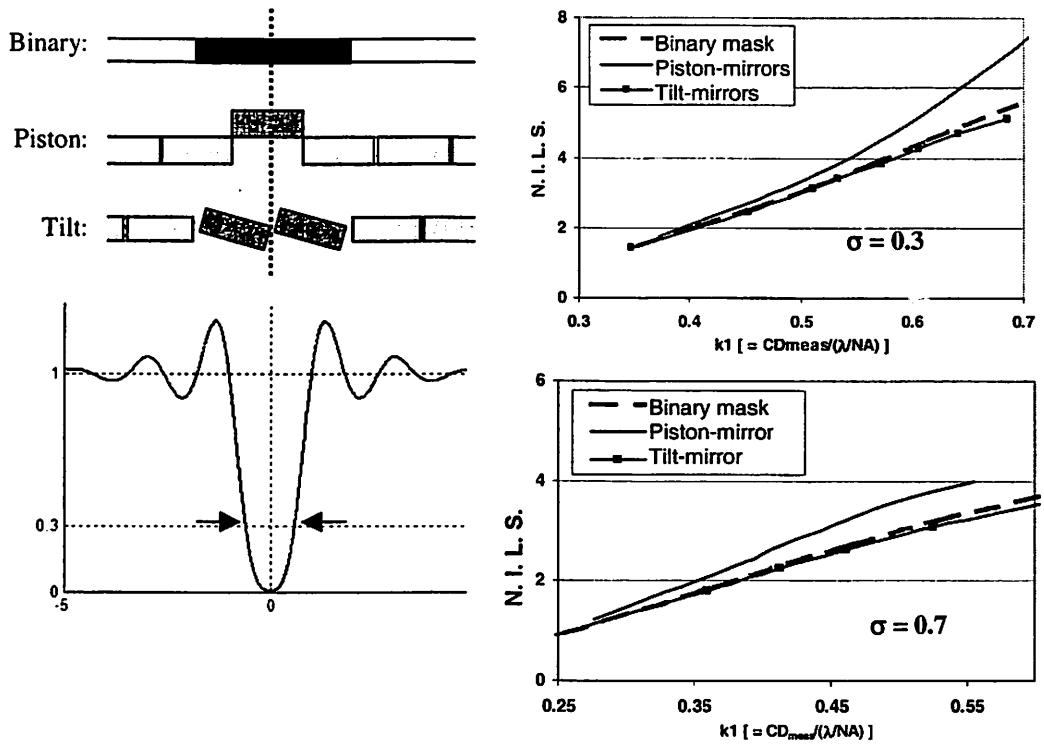

Figure 4-0: Varying optical system parameters for best operating conditions; k1spot varied for sigma = 0.3 and sigma = 0.7 with NILS plotted against measured k1.

However, these minimum features are generated 'on-grid'; for fair comparison, we need to compare NILS and k1 for worst-case 'off-grid' minimum features. Figure 4-0 shows image slope and k1 comparison for a minimum feature at various positions on the grid generated by piston mirrors. Figure 12 compares NILS v/s. k1 for tilt mirrors. We notice that in both cases, 'off-grid' image quality degrades, however, for the piston case, the worst-case line positioning (approximately mid-way between the two symmetric cases shown to the left of Figure 4-0) is somewhat better than binary masks. The NILS of tilt mirror generated features is somewhat lower than for binary masks for minimum features printed 50% 'off-grid'. We will see in Chapter 5 that the use of image optimization,

including overtilt, changes this result. In fact, tilt mirrors can outperform binary and provide comparable process window as alt. PSM or piston mirrors.

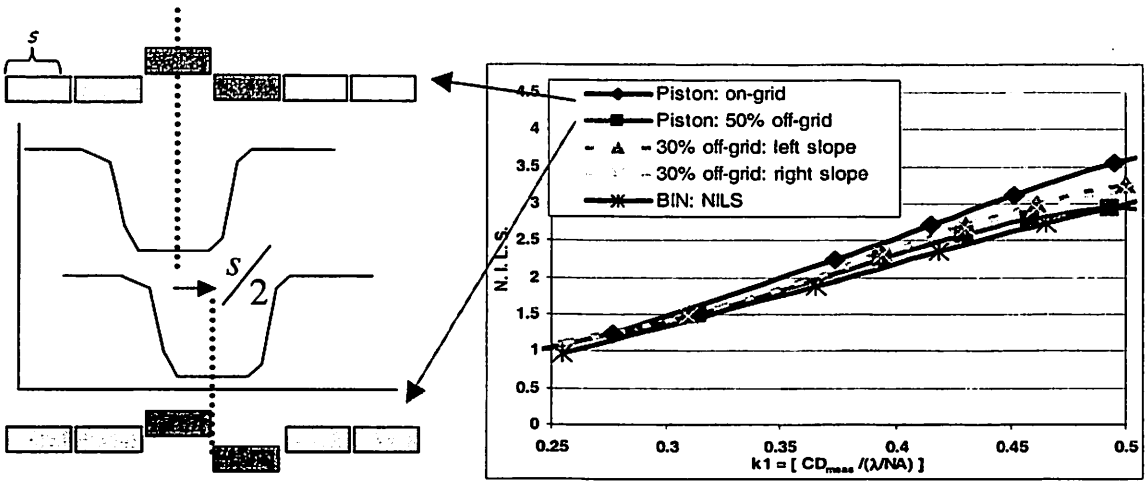

Figure 4-0: Line position effect on image quality – Piston (pure-phase) mirror & binary mask; $\sigma = 0.7$

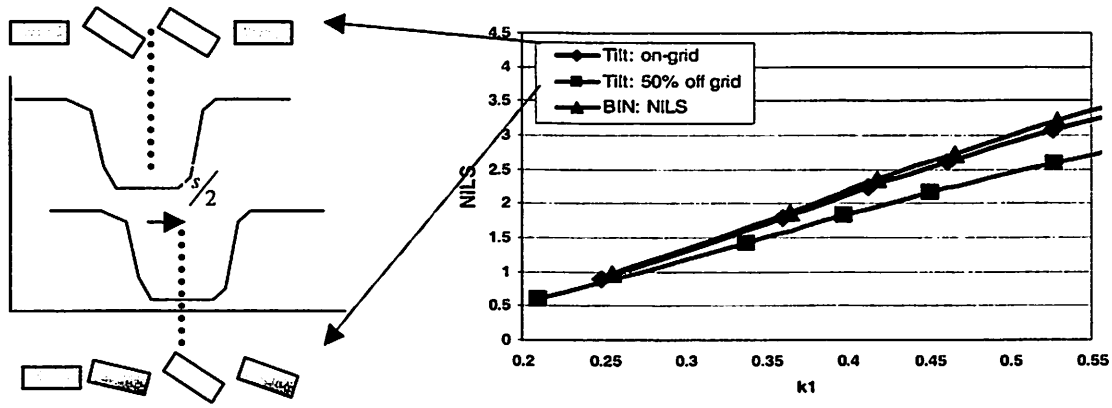

Figure 4-0: Line position effect on image quality -- Tilt case & binary mask; $\sigma = 0.7$

4.10 Bringing minimum features together

Thus far, edge-placement and linewidth modulation of an isolated feature have been used for comparing pattern generation architectures. Choosing a partially coherent sigma of 0.7 and a slightly sub-resolution spot with $k1_{spot}$=0.2, we examine the image slope of an isolated line-pair as the center-to-center separation is increased.

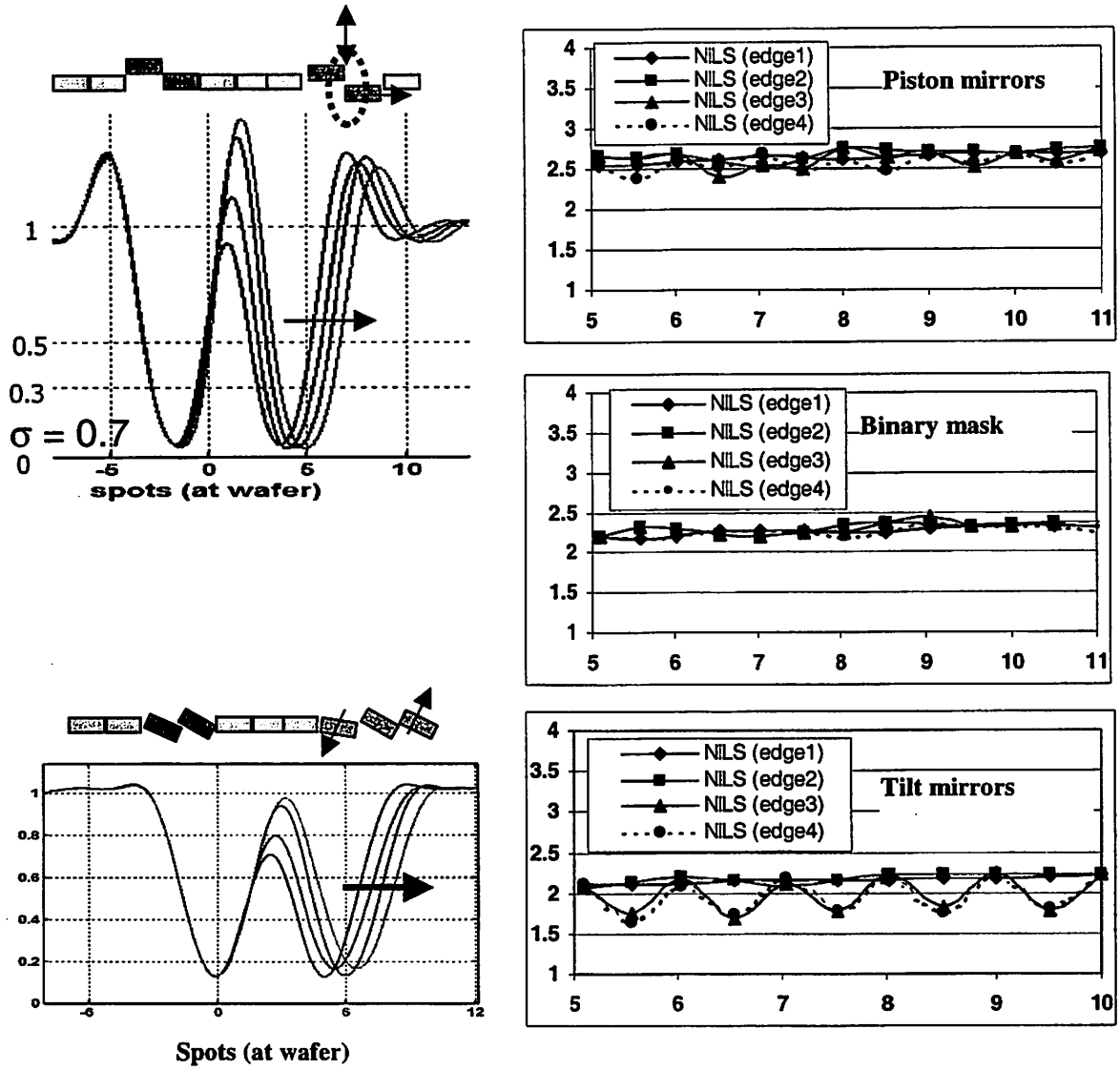

Figure 4-0: As the second line is shifted away from a fixed minimum feature, image slope of all four edges are only slightly affected. $k1_{spot} = 0.2$; $\sigma = 0.7$.

Figure 4-0 compares binary mask generated aerial images with both maskless architectures, tilt and piston modulators. Based on line slope measurements, the quality of images synthesized for piston mirrors are better than those generated by binary masks or tilt mirrors. In Figure 4-0, we look at a dense line/space pattern with varying $k1_{spot}$ of

piston-mirrors. Since an isolated minimum feature has a linewidth slightly over 2 spots/MFS, in order to print minimum pitch line/space pattern, we choose about 5spots/pitch. The right side of the same figure is a comparative plot of NILS as a function of k1 for each architecture. Again, it is clear that under the circumstances examined here piston based phase mirrors perform better than binary masks and tilt mirrors.

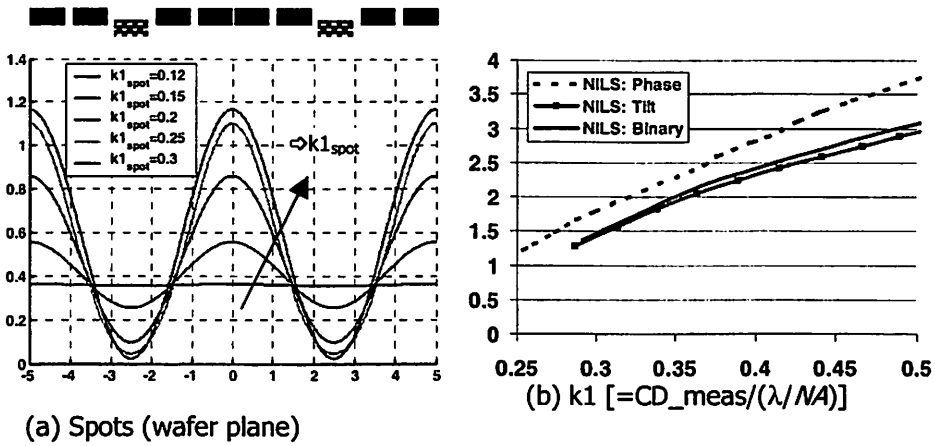

Figure 4-0: Dense L/S (5spots/MFS) (a) depicts an aerial images generated with piston mirrors as $k1_{spot}$ is varied, (b) shows the NILS as a function of k1 for each architecture; sigma = 0.7.

If an appropriate mirror motion algorithm is followed, we find that the NILS of several example features hold up well with grayscale modulation of edge position. Secondly, even though the mirrors are "tweaked" to maintain a desired CD and geometrically the mirror positions may not be symmetric, the image slope of right and left edges is very close for all cases considered. Finally, the normalized slope of piston-mirrors is found to be somewhat better than not only tilt mirrors but also binary masks..

In SPIE 2003 [5], T. Sandstrom has shown that over-tilting adjacent mirrors adjacent mirrors to get opposite phase can be used to provide steeper edge slopes. We have included this strategy in the next chapter where we study the effect of mirror architectures on process window.

4.11 Conclusion

A fixed mirror array introduces a grid in the object plane that is about one-half of a minimum feature (with $k_1 \sim 2\ k_{1spot}$). Compared with best e-beam and laser mask patterning schemes which allow CD/10 to CD/50 edge positioning, the nanomirror array grid is much larger, and grayscaling must be used to achieve fine positioning of edges.

Thus we compare with different types of masks such as alternating phase-shift masks (alt. PSM), attenuating PSM, or even simple chrome based binary image mask (BIM). The previous chapter discussed mostly tilt and piston mirrors; however, in this chapter, I will also introduce another mirror modulation scheme that is a hybrid of the tilt and piston approaches. It is referred to as 'pseudo-tilt' or 'dual-piston' design and is described in detail in a later section.

4.12 References

[1] N. Chokshi, F. Pease, Y. Shroff, Y. Chen, W. Oldham, R. Pease, et. al, "*Maskless EUV Lithography*", Journal of Vacuum Science and Technology B, Nov. 1999.

[2] U. Ljungbald, T. Sandstrom, H. Buhre, P. Durr, H. Lakner, "*New architecture for laser pattern generators for 130nm and beyond,*" 20th Annual BACUS sym. on Photomask Technology, SPIE vol. 4186, pp 16-21.

[3] O. Solgaard, F. Sandejas, D. Bloom, "*Deformable grating optical modulator*," Optics Letters, vol.17, no.9, 1 May 1992, pp.688-90. USA.

[4] Derek Lee, Dave Newmark, Kenny Toh, Phil Flanner, A. R. Neureuther, "*SPLAT v. 5.0 user's guide*," Memorandum No. UCB/ERL M95/13, 1 March 1995.

[5] T. Sandstrom, J. Backlund, N. Eriksson, J. Bengtsson, "*SLM lithography: how well can a stepper without masks and one with masks be matched?*", Microlithography Conference, SPIE, Santa Clara, 2003.

[6] J. F. Goodman, "Introduction to Fourier Optics," McGraw Hill, pp. 66-68, 1996.

5 Image optimization

5.1 Introduction

In this chapter quantification of image quality using exposure latitude and depth-of-focus based process window is used to compare piston and tilt mirrors with attenuated phase-shift masks (att. PSM). A comparison with other conventional masks such as pure PSM and binary masks is not provided. In an att. PSM, phase information is modified by either subtracting or adding material from the mask substrate at a thickness that corresponds to a π phase shift. The cost of these masks goes up with the number of allowed phases (limited to about four: 0, 90, 180, 270 degrees). Our goal of this chapter is to use the added phase and amplitude degrees of freedom to enhance nanomirror imaging [5].

During the course of this study, it was discovered that defocus related image shift with tilting and piston mirrors can be a significant problem. The next section gives details on how the image shift can be eliminated in most cases and minimized in the rest. The concept of 'overtilting' mirrors is covered next to demonstrate that we can get even better images than shown in the previous chapter. Examples from knife-edges to contacts are covered. Reticle enhancement techniques such as OPC and ATT-PSM are restricted in their effectiveness with conventional masks because of very limited number of phase and amplitude values. Use of tilt and piston micromirrors allows finer control over amplitude and phase (albeit over a set mirror grid) that can be gainfully used to create sophisticated

images pre-compensated for complex lithographic effects. This chapter addresses the image optimization challenge of maskless lithography in the last section.

5.2 Defocus related image shift

It is well known that an off-axis point source results in image shift. Since the center image forming ray arrives at the image plane at an angle, moving away from best focus concurrently leads to drifting of image. Therefore, illumination sources are generally balanced to maintain a high degree of telecentricity. However, in case of micromirror based printing, even with balanced source, image drift is possible. This section deals with this important issue because, if left uncorrected, it can severely reduce the process latitude of mirror based imaging systems.

Tilting mirrors inherently have a continuous phase variation across the mirror length. The frequency spectrum of a tilted mirror is shifted in the positive or negative direction based on the direction of tilt. If we have a large array of equally tilted mirrors, energy from the 0^{th} order is transferred to the higher +1 or -1 orders as was discussed in chapter 4. In terms of imaging, this situation is analogous to having an off-axis point source deflecting the 0^{th} order. The effect of having an unbalanced +1 and -1 order with tilting mirrors is that the center of the image starts to become focus sensitive.

Piston mirror images behave similarly. If a single mirror is displaced, the phase map is symmetric and no defocus related image shift will be observed. However, to move a feature edge across the grid, we need to concurrently move two mirrors up and down as discussed in chapter 4 leading to asymmetry in phase distribution. Asymmetric mask results in positive and negative components of the frequency spectrum not balancing as a

result of which telecentricity is lost and image starts to drift with defocus. The angular spectrum of Figure 5-0 shows the schematic diagram of the image formation method to graphically explain this image drift issue.

As with off-axis illumination related image drift, the solution to mirror based image centering is in balancing phase differences. One way to achieve this is by alternating the direction of mirror position across rows and down the columns. The average effect of this scheme is that the frequency spectrum is symmetric around DC and defocus related image drift is largely eliminated. At any focus level, image shift corresponding to one mirror position is compensated by that of the adjacent opposite tilt mirrors so that the final image has no net displacement. We can expect the composite image to blur with defocus at a faster rate than the individual images because of this addition. Depth of focus decreases as a result.

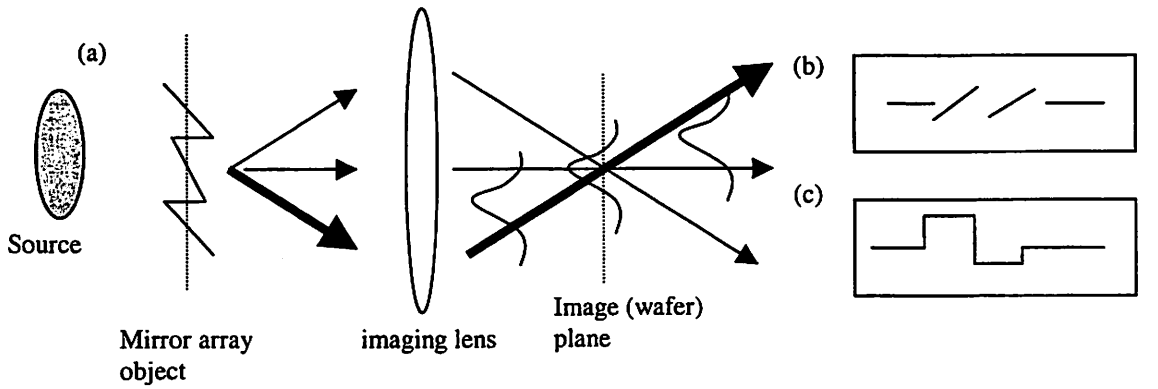

Figure 5-0: Graphical interpreation of defocus related shift with mirrors; (b) tilt, (c) piston mirror cross-sections whose asymmetric phase leads to image drift.

By way of an example, we will study a simple case of an isolated line wherein active mirrors are not symmetric with respect to a feature center and the feature edges are

printed off-grid. Using nominal parameters such as $k_{1spot} = 0.2$, sigma = 0.3, and $k_1 = 0.5$, we want to print an isolated minimum sized line using both types of mirrors. Figure 5-0 shows a layout of the line and the adjacent figures show cut-lines of aerial images created with piston and tilt mirrors. In each case, two mirrors are active to create a minimum sized dark line. In the tilt case, both mirrors are tilted such that there is a ½ λ optical path difference between the center and edge of the active mirrors. In case of piston mirrors, two mirrors are pulled ¼ λ *OPD* away from nominal to create a strong ½ λ *OPD* phase edge at the center. For a 1-D line, this pattern is repeated down the column of mirrors as shown in the top portion of the figure. Asymmetric phase in the object plane with respect to the center of the line causes the pattern to shift with defocus. It is clearly observed that this implementation of mirror positioning strongly hurts the process latitude.

One possible way of correcting drift is by alternating mirror position. Tilt mirrors modulate in the opposite direction in alternate rows by the same amount. Similarly, piston mirrors modulate above or below nominal position. In this arrangement, the sub-resolution mirrors are still not symmetric across a row; however, the asymmetry is reversed down a column, thereby eliminating image drift. Image drift for off-grid patterns is also eliminated. This example is important for two reasons. One, it shows that drift is of significant concern, and, two, tilting mirrors need to be designed for bi-directional modulation.

This example works well for 1-D features such as lines and spaces where there are sufficient mirrors to average the frequency spectrum imbalance to symmetry; however,

asymmetry at line-ends and corners is not compensated. We can expect some defocus related shifting of corner edges but the effect is buried in the blurring of images.

By way of example, Figure 5-0 shows two orthogonal line-ends printed with and without the alternating phase mechanism to qualitatively demonstrate this effect for piston mirrors. For either orientation, phase mismatch at the edge is not compensated, which leads to the slight twist of line-ends. Tilting mirror based images have similar profile. It can be inferred that center of contacts would also drift with defocus for the same reasons, thereby impacting the process latitude. This will be further discussed in the section on contacts towards the end of the chapter.

In Figure 5-5, we show that image drift is eliminated for across the grid. Various defocus curves are overlapping, indicating the the center does not shift.

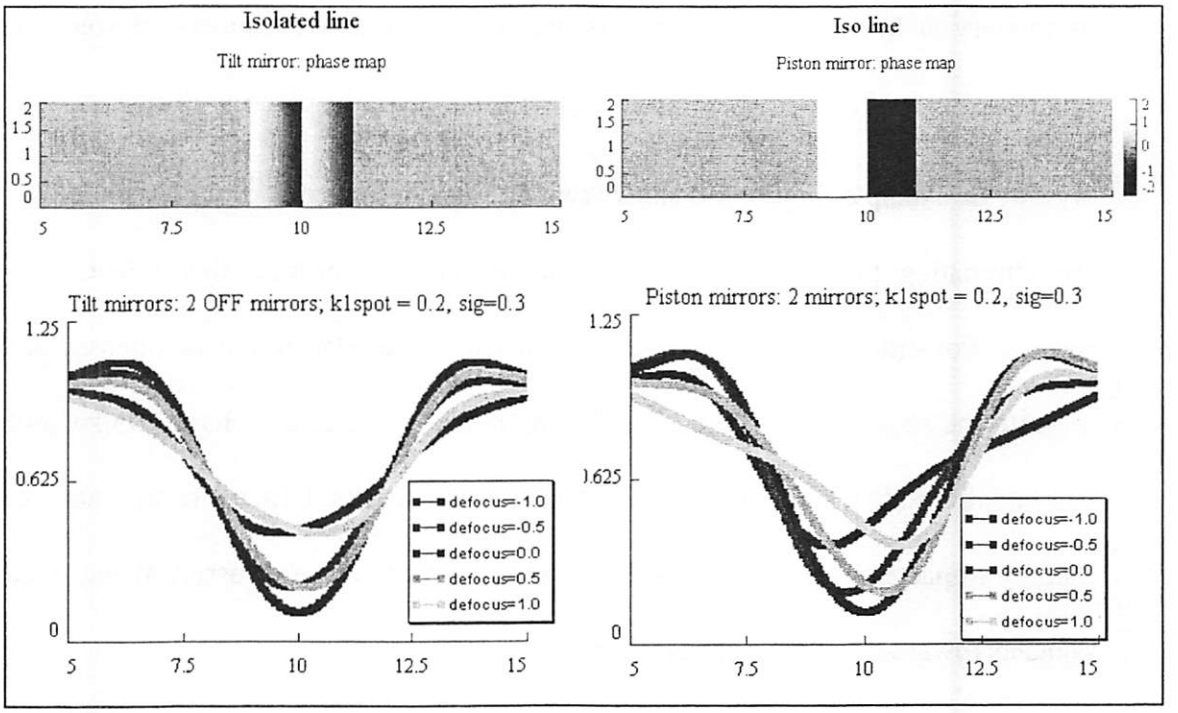

Figure 5-0: Image drift due to asymmetric mirror position seen for tilt and piston mirrors; monopole illumination.

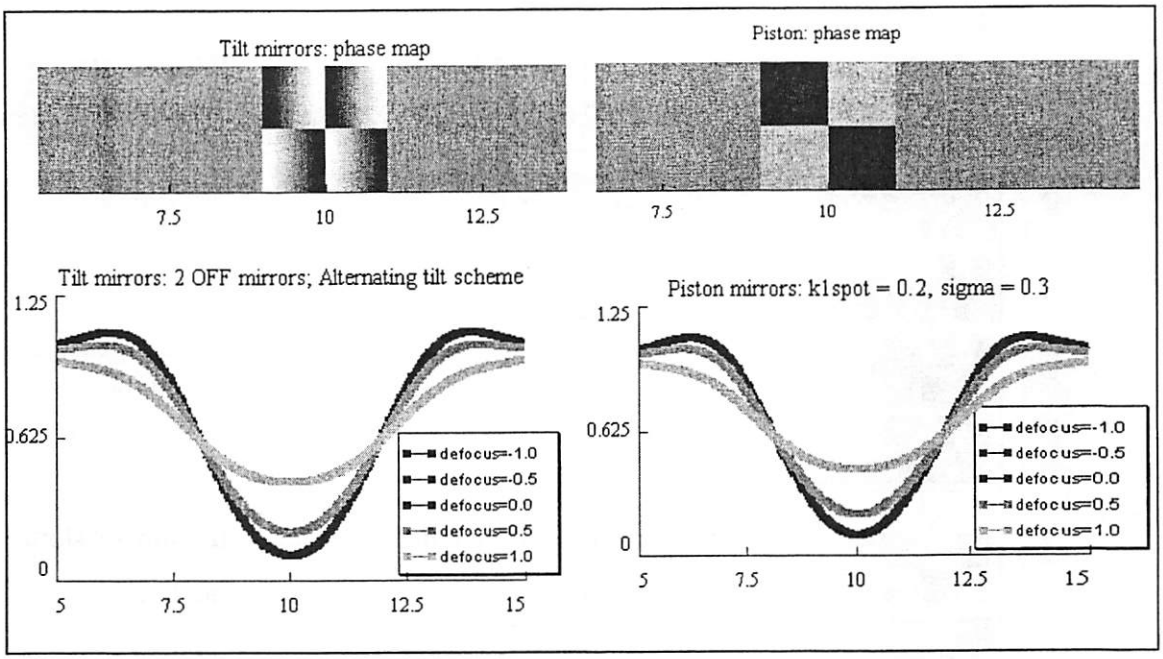

Figure 5-0: Image drift eliminated for 1-D lines with alternating mirror arrangement seen above.

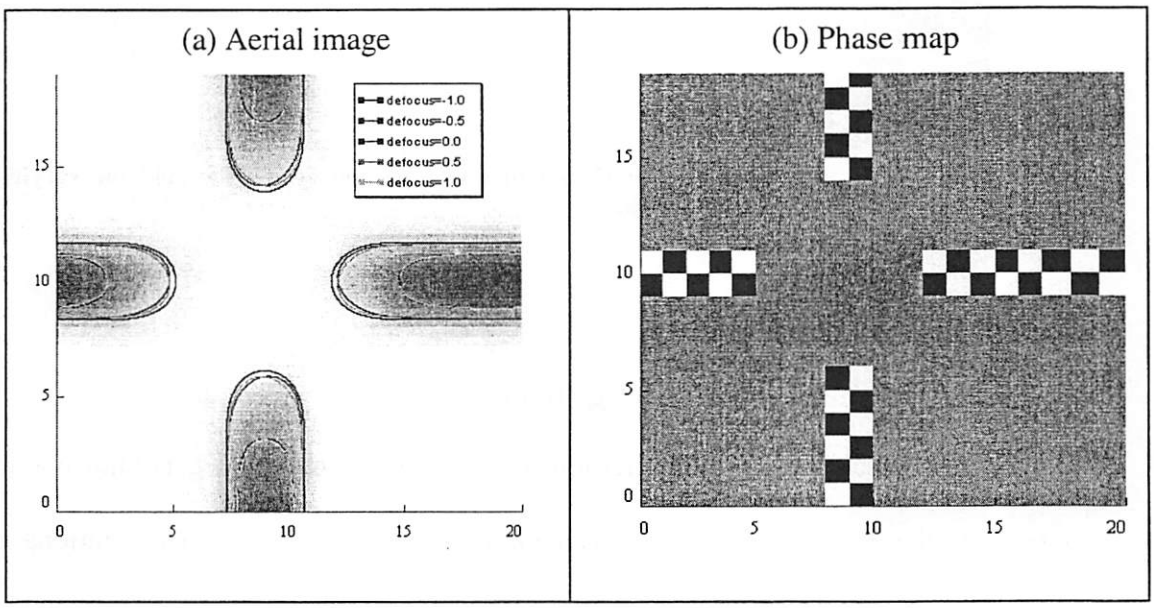

Figure 5-0: Effect on line-end due to defocus for piston mirrors.

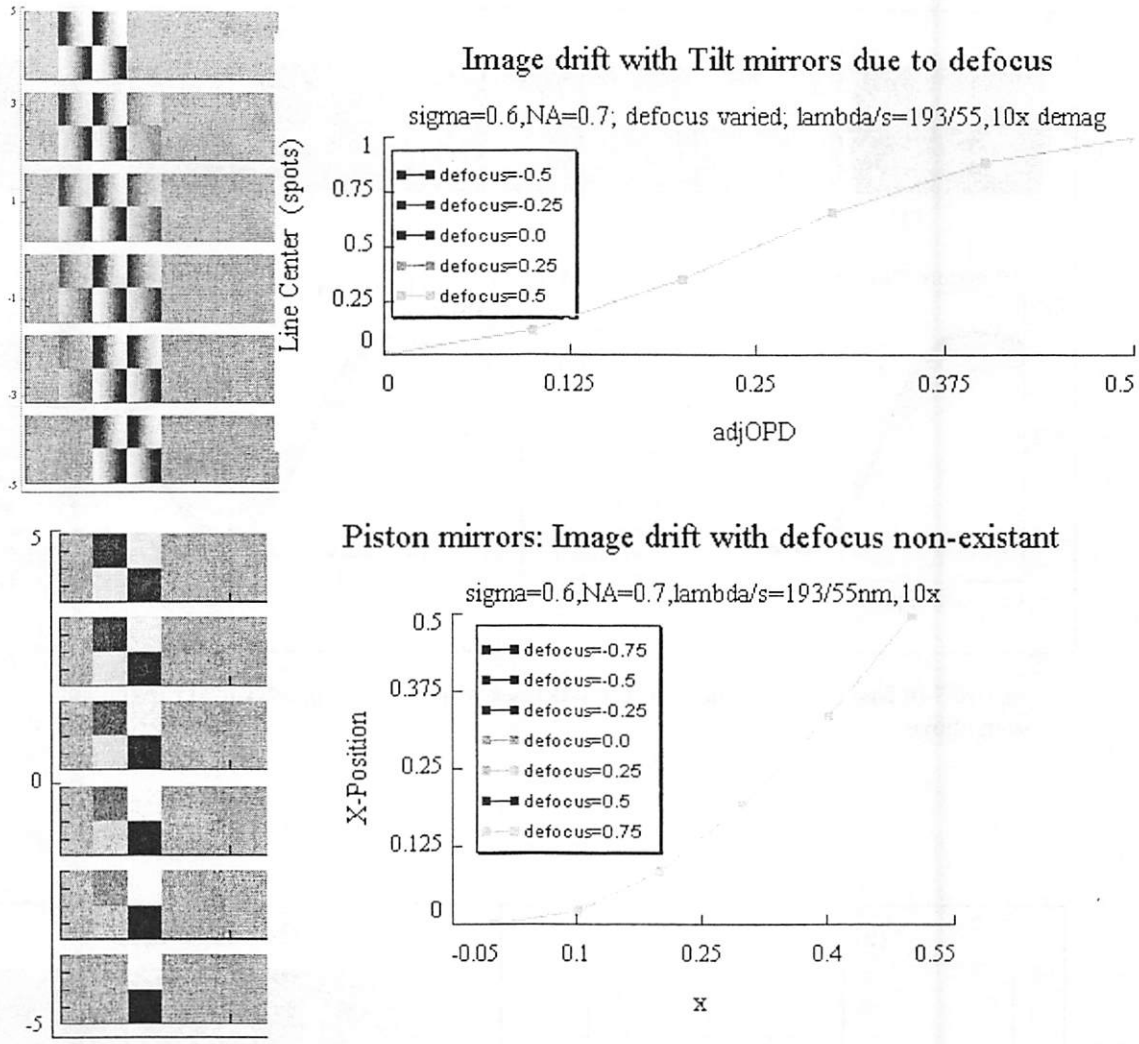

Figure 5-0: Center of image plotted across the grid for varying defocus values.

5.3 Image enhancement using 'overtilt'

The use of grayscale positioned micromirrors as a dynamic pattern generator is immense in terms of the flexibility afforded in generating high fidelity images. Conventional masks are limited in scope by virtue of having comparatively fewer phases. On the other hand, tilt and piston mirrors provide a larger dynamic range of amplitude and phase values but are limited by their pixelated layout. Thus far, we have discussed the capability of

analogously modulated mirrors in generating grayscaled images (edge placement with 5-bit accuracy within a grid defined by the mirror spots at the wafer plane). The high phase and amplitude resolution of mirrors can also be used to improve the quality of images by increasing not just the contrast or slope of the edges and corners but also increasing the overall process latitude. In this section, we will first re-visit the frequency spectrum of tilting and piston mirrors to gain an intuitive understanding of how image fidelity can be improved and follow up with relevant examples. In a subsequent section much of what we cover here will be implemented in the form of rules to write efficient mirror based OPC algorithms.

Frequency spectrum: An optical projection lithography system is essentially a low-pass filter, allowing only the DC and nearby frequency components through the lens pupil for imaging. When the mirror tilts to an angle corresponding to $\lambda/2$ optical path difference (*OPD*) between its center and edge, the optic allows a near linear portion of the mirror frequency spectrum to pass through. At the image plane this results in a near null e-field by virtue of the positive and negative frequency components nearly canceling each other. As the mirror continues to tilt, the first side lobe of the mirror spectrum goes through the imaging optic. For 0.75λ *OPD*, complete phase reversal results in maximum negative amplitude at the wafer plane. By choosing to place an overtilted mirror next-to-near an edge, we can expect the image log slope to improve since the peak intensity of the bright area is effectively "pushed" up [4]. Higher ILS should increase the process latitude.

5.3.1 Knife-edge: tilting mirrors

One of the simplest demonstrations of the advantage of overtilt can be made with a knife-edge feature. We want to improve the ILS of the edge by appropriately overtilting neighboring mirrors. Based on the shift in the frequency spectrum with tilt, it appears that highest slope might be achieved with overtilt of next to nearest edge pixels since the first side-lobe of the 0.75λ *OPD* mirror is 3.5spots away from the center of the overtilted mirror. In Figure 5-0 the mirrors are identified as M_n where n is an integer representing the location of the mirror with respect to the edge. In the following table, Case A is the nominal layout of mirror for an on-grid edge placement. The mirrors to the left of the edge are all fully 'on' (no tilt, *OPD* = 0λ) and the ones to the right are fully off (tilt corresponding to *OPD* = 0.5λ). Cases B-K examine the changing ILS as a result of overtilting mirrors according to the scheme of Table 3.

Table 1: Unoptimized tilts for knife-edge feature

Mirror spot	M_{-4}	M_{-3}	M_{-2}	M_{-1}	M_1	M_2	M_3	M_4	M_5
Nominal *OPD*	0	0	0	0	0.5	0.5	0.5	0.5	0.5

Table 2: Modified mirror tilts

	M_{-4}	M_{-3}	M_{-2}	M_{-1}	M_1	M_2	M_3	M_4	M_5
Case A	0	0	0	0	0.5λ	0.5λ	0.5λ	0.5λ	0.5λ
Case B	0	0	0	0	0.75λ	0.5λ	0.5λ	0.5λ	0.5λ
Case C	0	0	0	0	0.5λ	0.75λ	0.5λ	0.5λ	0.5λ
Case D	0	0	0	0	0.5λ	0.5λ	0.75λ	0.5λ	0.5λ
Case E	0	0	0	0	0.5λ	0.5λ	0.5λ	0.75λ	0.5λ
Case F	0	0	0	0	0.75λ	0.75λ	0.5λ	0.5λ	0.5λ

Case G	0	0	0	0	0.5λ	0.75λ	0.75λ	0.5λ	0.5λ
Case H	0	0	0	0	0.5λ	0.5λ	0.75λ	0.75λ	0.5λ
Case I ☺	**0**	**0**	**0**	**0**	**0.75λ**	**0.75λ**	**0.75λ**	0.5λ	0.5λ
Case J	0	0	0	0	0.5λ	0.75λ	0.75λ	0.75λ	0.5λ
Case K	0	0	0	0	***All 'off' mirr. set to overtilt: OPD=0.75λ***				

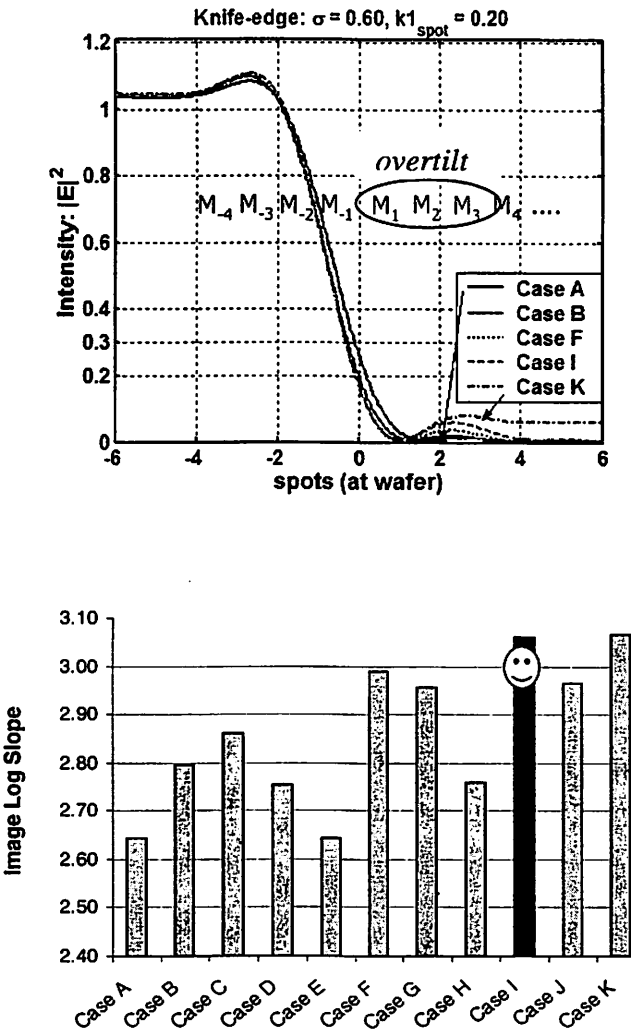

Figure 5-0: Optimizing slope by overtilting selected number of mirrors closer to the edge. Mirror location with respect to an on-grid edge is identified by Mn. Image log slope is normalized by using a linewidth of 2 spots.

The question of optimum tilt conditions for various mirrors adjacent to edge can be answered as follows. For a wide dark feature, overtilting 'off' mirrors improves ILS, as evidenced by *cases* {*B, F, I, K*}. Overtilting all the off mirrors, as in *case K*, leads to diminishing returns in ILS while introducing a background intensity (compare the above figure with the grayscaled intensity vs. *OPD* figure of section 4.2; *OPD* = 0.75λ

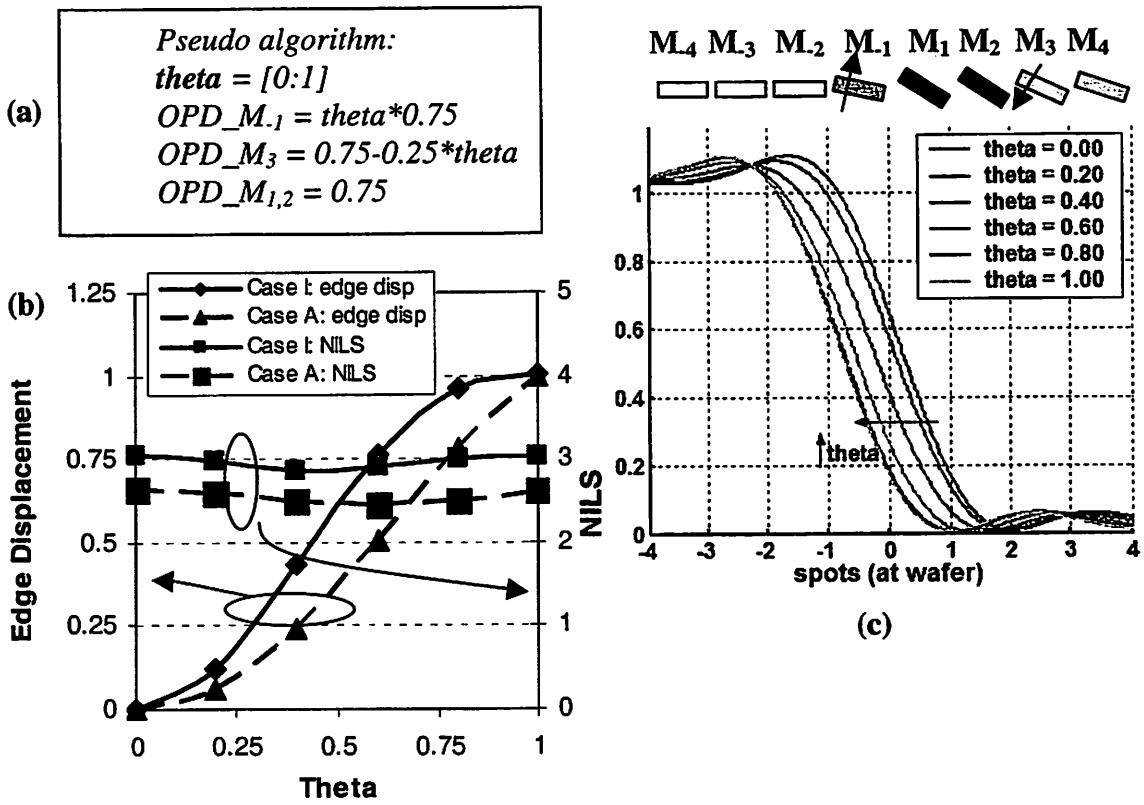

Figure 5-0: Moving optimized ILS knife-edge across grid. (a) Case I modified for across grid placement; (b) ILS and edge placement as a function of theta; (c) mirror arrangement and resulting aerial image sequences. NOTE: NILS is Image Log Slope normalized by using MFS linewidth of 2 spots.

$$k1_{annt} = 0.2,\ \sigma = 0.6$$

introduces around 10% intensity). As seen from the bar chart above, *case I* provides high ILS and limits the range of side lobe intensity to a few spots.

In the following example, we want to examine the effect on ILS of displacing the knife-edge across the grid. The normalized log slope and edge displacement as a function of new parameter *theta* are plotted in Figure 5-0 for case I. For comparison with the nominal case where mirrors are not overtilted, ILS and edge displacement data from case A is also plotted in Figure 5-0 (c). While we get ~20% improvement in edge slope (throughout the grid) as a result of overtilting, there is a cost in terms of reduced linearity between mirror position and edge location, as evident from the figure.

5.3.2 Knife-edge displacement: Double-piston mirrors

In this section, we propose another mirror design that combines the advantages of pure phase piston mirrors and the amplitude modulation of tilt mirrors. The double-piston mirror is a single piston mirror bisected in two, with each part operating as a piston mirror. We modulate the mirrors the same way tilt mirrors are modulated, but with each half-mirror pair working co dependently. *OPD* is measured as twice the path difference between the two halves of the mirror. Increasing the *OPD* for certain half-mirrors should provide similar advantages with double-piston mirrors as with tilting mirrors but the edge slope should be higher.

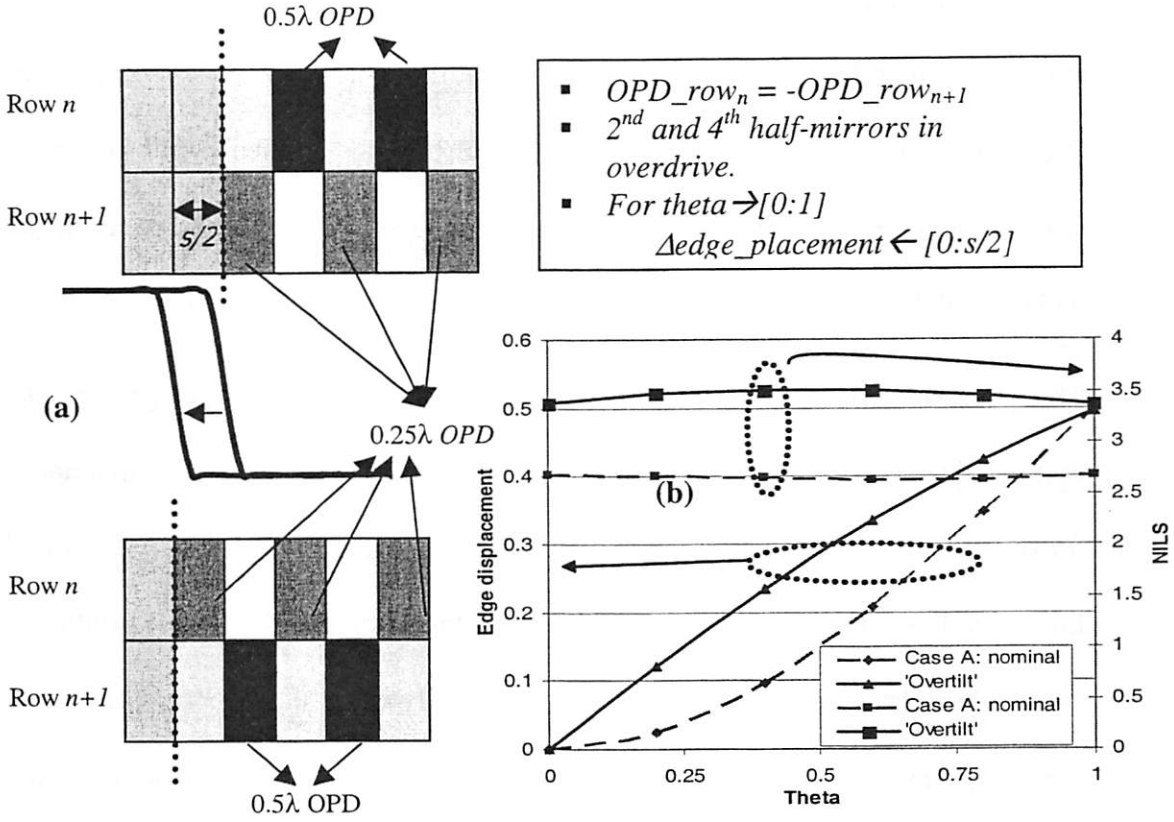

Figure 5-0: (a) phase maps of double piston mirror array for printing a knife-edge. Left of the dotted line in each case has mirrors with zero *OPD* for bright field area. Null intensity is created with alternating +/- 0.25λ *OPD* half-mirrors. Higher slope is achieved by 'overtilting' select mirrors (0.5λ *OPD*) as shown. (b) ILS and edge displacement for knife-edge displacement across grid. Dotted lines represent nominal case A of previous section (no mirror 'overtilt'). *$k1_{spot} = 0.2$, $\sigma = 0.6$ are used for this example.*

In Figure 5-0, the double-piston mirror concept is used to move a knife-edge across half-spot width. Compared to the nominal case of no "overtilt", there is a significant improvement in not only the image log slope but also the linearity of edge placement as a function of edge mirror *OPD*. Also, comparing edge slope and linearity results between Figures 5-2 and 5-3, we notice that there is about 20% gain in edge slope with dual-piston mirrors over tilting mirrors, across grid. A secondary advantage is the improvement in linearity of edge-displacement as a function of edge mirror *OPD*.

5.3.3 Isolated line and isolated space

As a first demonstration of the advantage of overtilt, an isolated space example is studied. We examine two cases: $\sigma = 0$ and $\sigma = 0.60$ to show the applicability of overtilt over a wide range of partial coherence. Specifically, spot-size resolution parameter, $k1_{spot} = 0.2$ and the isolated space width is chosen to be 2 spots.

The perceived advantages of overtilt and the double-piston mirror design are tested with optimized printing of an isolated minimum sized space. This feature is important to study for two reasons. One, it allows us to examine the concept of enhanced *OPD* for dark-field layout, and two, it provides us better understanding of optimized contact printing. A two-spot wide isolated space, with adjacent mirrors fully off at 0.5λ *OPD* is our nominal tilt case. If all the 'off' mirrors are overtilted to 0.75λ *OPD*, we expect and get undesired uniform background intensity. However, keeping only few nearest to edge 'off' mirrors overtilted gives us the dual advantage of increased slope and larger process window. This is demonstrated in Figure 5-0 which shows overtilted adjacent mirrors giving the highest peak intensity.

In order to determine which of the three mirror modulation techniques are best for printing isolated spaces, we need to plot an isolated space and obtain the exposure latitude-depth of focus for each method. Figure 5-0 shows the EL-DoF curves for a 100nm wide space patterned with piston, tilting and overtilting mirrors. The CD deviation tolerance is set to 10%. We find that patterns generated with dark pixels overtilted clearly provide a larger process window than piston mirrors.

As mentioned earlier, double-piston mirrors are like pseudo-tilt mirrors. Their main advantage is in allowing sharp phase edges, leading to higher NILS and process winodw for isolated lines (to be covered later). However, to understand how they far with isolated spaces, we need to look at Figure 5-0 (c) where we compare overtilt with two offsets in double piston (OPD=0.5lambda and OPD=0.6lambda). Higher offsets results in creating a minima at the center of the feature. It appears that double-piston mirrors match overtilted mirrors in the total depth of focus lithography requirement. The exposure latitude does increase marginally with double-piston mirrors. This is an important result because it shows that breaking up a piston mirror in two halves and have them operate as a pseudo-tilt mirror might be advantageous. The double-piston process window is much larger than simple piston process window for the isolated space case covered here.

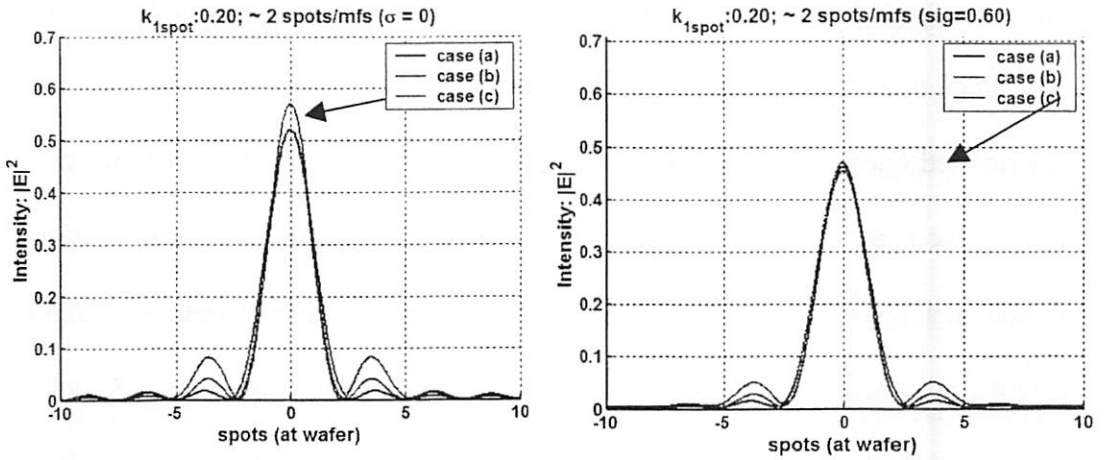

Case(a)	0.5λ	0.5λ	0.5λ	5λ	0.0λ	0.0λ	0.5λ	0.5λ	0.5λ	0.5λ
Case(b)	0.5λ	0.5λ	0.75λ	0.5λ	0.0λ	0.0λ	0.5λ	0.75λ	0.5λ	0.5λ
Case(c)	0.5λ	0.75λ	0.75λ	0.5λ	0.0λ	0.0λ	0.5λ	0.75λ	0.75λ	0.5λ

Figure 5-0: Overtilted mirrors (OPD=0.75lambda) are variously positioned to determine the location for highest ILS. Two overtilted mirrors positioned one away from the edge (case (c)) maximizes slope; the effect of overtilt for lower coherence is understandably mitigated.

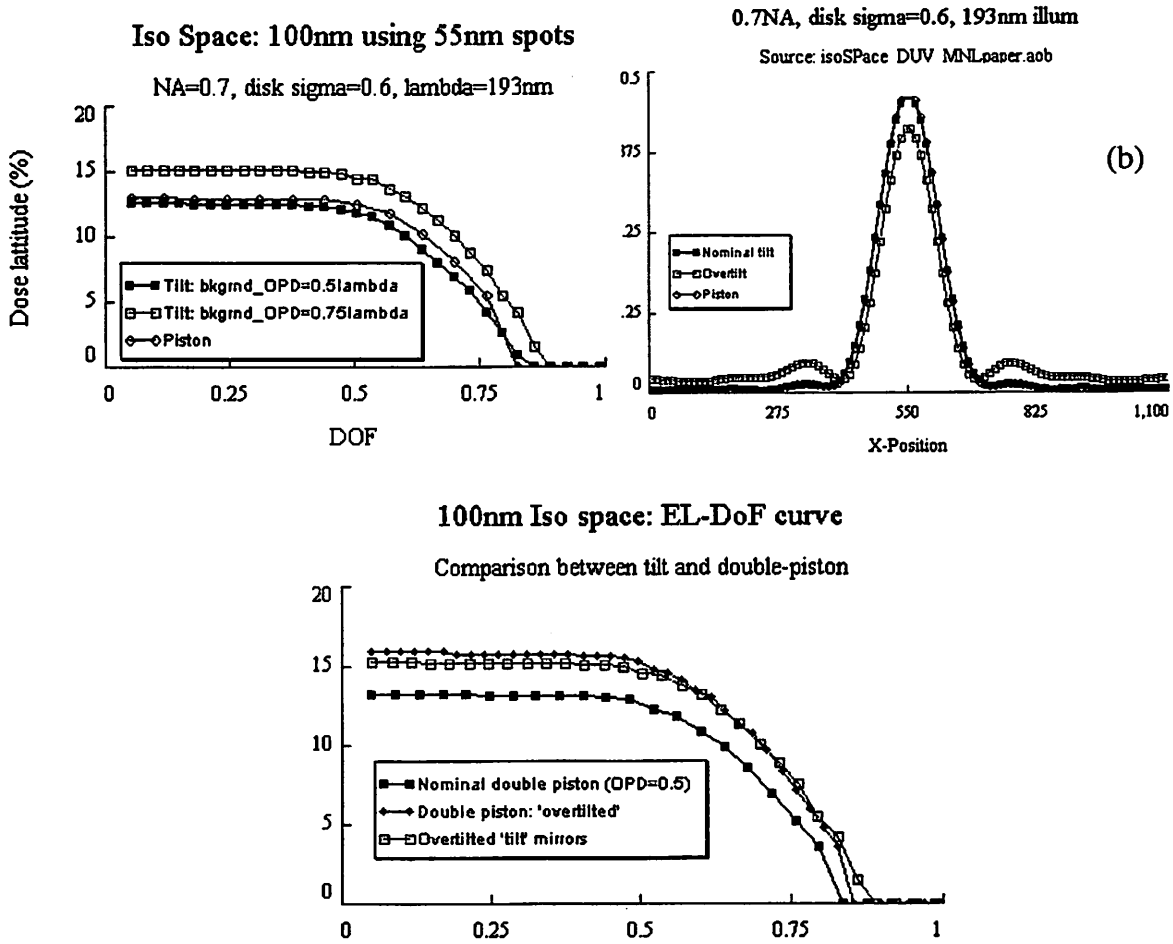

Figure 5-0: (a) Exposure latitude versus defocus process window for a nearly isolated space (dark field) using DUV exposure at *NA* of 0.7 and disk illumination. The 100nm feature is composed with 55nm spots at 193nm. (k1=0.4) Three mirror arrangements are simulated: simple piston motion with OPD in the range 0 to 0.5λ, simple tilt motion with OPD in the range 0 to 0.5 λ, and tilt motion with OPD in the range 0 to 0.75 λ ("overtilt") (b) The image intensity profiles for the three conditions above. (c) process latitude of "overtilted" versions of double-piston and tilt mirrors are compared.

In this section we would like to compare imaging results of conventional mask pattern with maskless lithography. Our emphasis is on printing the critical layers: poly-gate, metal, and contact. In general, metal layers have a tighter pitch while poly layer has the smallest CD. Contacts are special because they generally use a 'dark-field' mask and the

pitch of sets of contact arrays is optimized for illumination. Examples of isolated space imaging are precursors to a later discussion on printing contacts. Isolated line can use assist features to help with the depth of focus. Isolated lines would benefit from outriggers (assist features). Usually, they are about 60% of the size of the main feature with a center to center spacing about the same as the optimized pitch case. Assist features are used with isolated lines to help with depth of focus.

Alt. PSM can buy some process window, especially at very low CDs but it costs in terms of another exposure and is sensitive to coma aberrations. In terms of comparison with mask technologies, attenuated PSM can provide a sound basis for comparison. Atten PSM for production is almost always 6% transmission (6% intensity, 24.5% E-field). Higher transmission can help slightly but it also leads to printing of unwanted features. Also, mask inspection issues crop up since the mask is too transparent at the inspection wavelength.

Illumination can also be varied according to the pattern density. Annular illumination or its subsets dipole and quadrupole illumination are helpful in increasing the process window but there is always a concern of creating a large CD dependence on pitch.

- Simulation conditions:
- Choose: $k1_{spot} = 0.2$;
- Illumination: EUV (13.4nm) light;
- Spot size: 0.025nm,
- Magnification, M = 1;
- Numerical aperture: *NA*=0.11.
- Mirror array: 20mirrors wide. Off mirrors set to 0.5λ *OPD*.

- Two cases shown: sigma=0, sigma=0.6;

Observations: Ringing in the form of side lobe peak increases with overtilt of adjacent mirrors. The partially coherent case does not achieve improved process latitude due to overtilt. Mirrors right next to fully ON mirrors should not be overtilted; doing so results in lower peak intensity at the center of the space. Mirrors one over (next-to-nearest) are overtilted so that the side lobe e-field peak of overtilted mirrors reinforces the fully 'ON' central mirrors' peak. The negative intensity of the overtilted mirrors also combines with the edge to create a sharper slope. Thus, case (c) is best.

5.4 Isolated line

We study the important case of a minimum sized line, at an aggressive k_1 The optical system parameters are:

- Pupil $NA = 0.3$
- Disk illumination with partial coherence, $\sigma = 0.6$.
- CD = 20nm ➔ $k_1 = CD/(\lambda/NA) = 0.45$
- Assuming we want to use about 1.8 spots to print the minimum sized feature, set $k_{1spot} = 0.25$. Then, spot-size, s = 11nm.

To print an isolated line, we turn off about two pixels. Phase/magnitude map of several mask technologies is given in the following figure. The accompanying figure is an intensity cross section of the 1-D feature. The capability of printing the smallest isolated features is an important criterion for any technology. Of course, a dark line can be printed with a simple phase edge; however, line termination is a problem. In addition, since the

phase edge is created by offsetting adjacent mirrors, we cannot move the line incrementally off-grid.

Mirror over-tilt enhances the total window, making it comparable to the two-mirror piston case. Single mirror piston line is understandably better than the rest due to the strong phase edges but it is also a special on-grid case. In order to move the line, we need to take a mirror pair and move it up or down. Double-piston (pseudo-tilt) is similar to piston case.

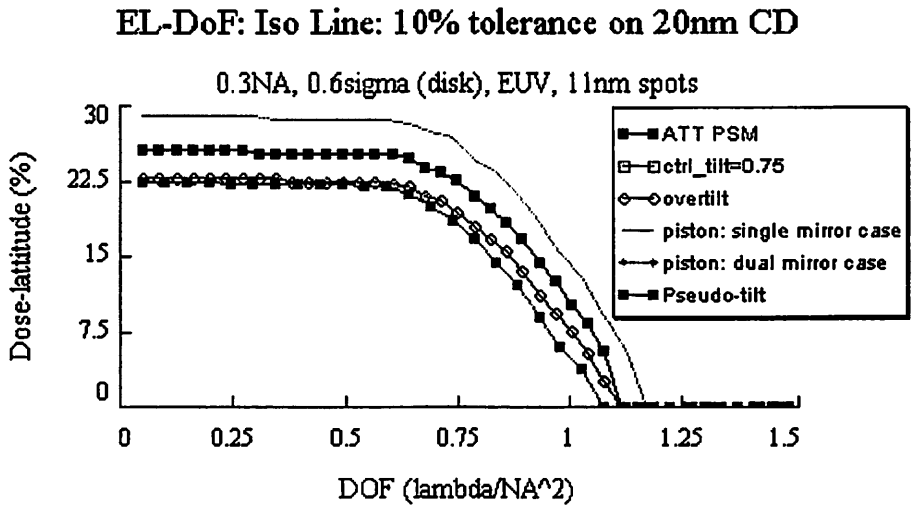

Figure 5-0: For 10% variation in desired CD=20nm, exposure lattitude is plotted as a function of depth of focus. DoF is in units of (λ/NA^2).

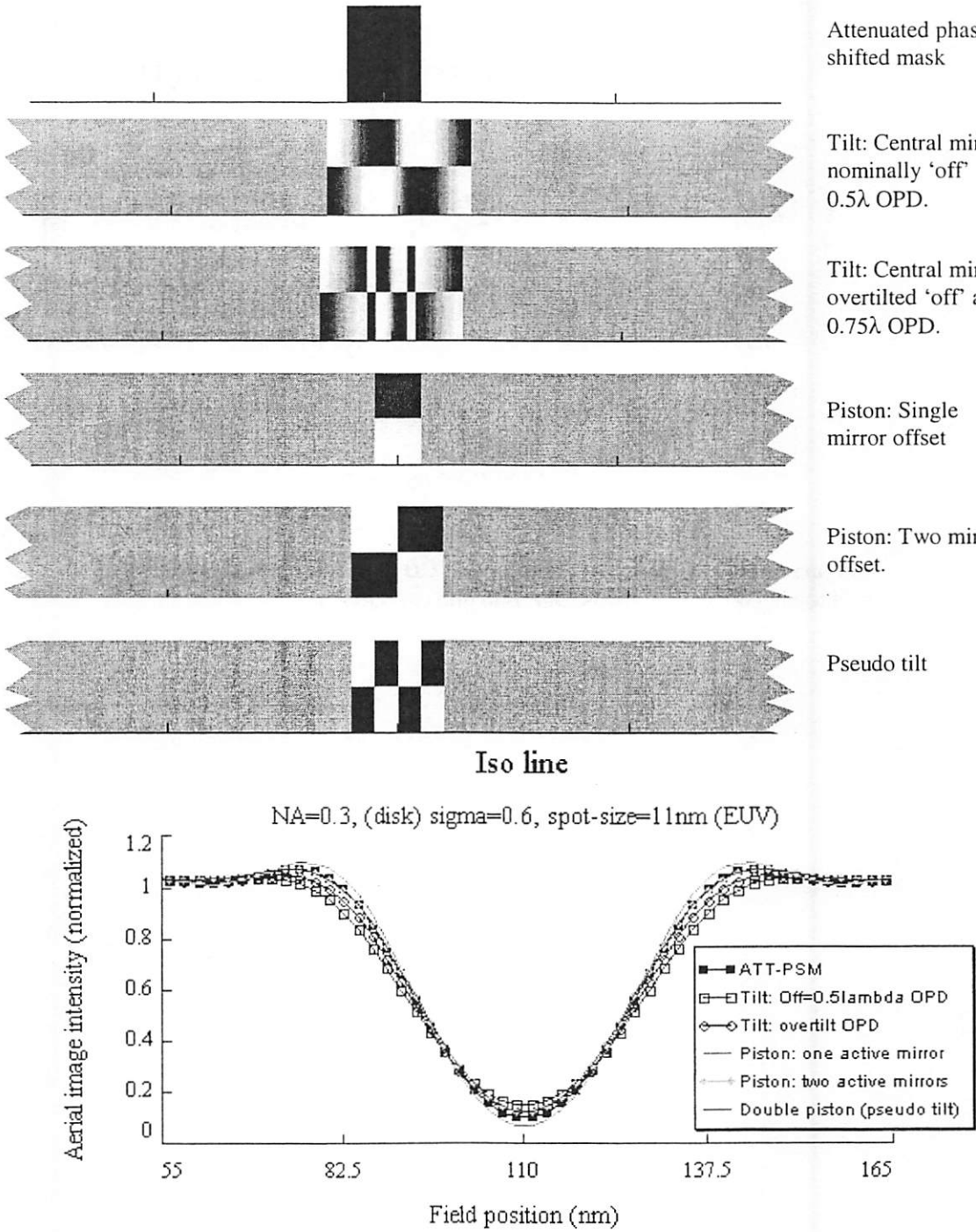

Figure 5-0: a) phase map of several mirror architectures used to print an isolated line; b) Aerial image cutline of the 1-D feature.

5.5 Tight pitch

Various mirror modulation methods (for both piston and tilt cases) were explored to print dense features as a way of comparing piston/tilt mirror with advanced conventional masks. For example, dense 100nm lines / 220nm pitch were printed using 55nm spots and quadrupole illuminator. Printing off-grid causes a drop in process-window latitude as was previously reported.

Process-window, measured as a degree of trade-off between exposure-latitude (EL) and depth-of-focus (DOF), is an important metric that informs us about the robustness of a given printing technique [2]. EL-DOF curves for iso and dense lines/spaces with tilt and piston mirrors compare favorably with ATT-PSM and Alt PSM, however, we note that process latitude for pixel based imaging decreases when printing off-grid feature edges without compensation. For example, asymmetry in the phase or amplitude of the reflected e-field results in serious image-drift with defocus. We have demonstrated that image drift can be eliminated without loss in fidelity by alternating mirror positions down a column. Figure 2 shows a dense array of contacts printed at $k_1=0.44$ (20nm diameter at EUV wavelength, NA=0.3 and disk illumination $\sigma = 0.8$). The resultant EL-DOF curve is based on a cumulative process-window for contacts printed across the grid. ATT-PSM and tilt mirrors are compared.

5.5.1 Evaluation across masks

Comparison: 100nm/220nm is 1.8spots/4spots. Spot is $0.2*\lambda/NA$ ($k1_{spot} = 0.2$)

- DUV: λ = 193nm, pitch = 100/220; Choose $NA = 0.7$ → k1 = 100/193*0.7 = 0.363

- EUV: λ = 13.4nm, pitch = 20/44; choose *NA* = 0.3 → k1 = 20/13.4*0.3 = 0.45;

EUV: max is around 0.4 to 0.5 depending on overtilt; min is around 0.2; contrast is low.

R = 0.625; θ = 45 degrees; σ_{out} = 0.125

Pitch = x * λ/NA = 0.44 = k1*0.0134/0.3 => k1 = 0.044/0.0134*0.3 ~ 1

ATT-PSM: Choose *NA* = 0.35 for 20nm line/40nm pitch; pitch = 1 λ/NA

Need to optimize contrast as well as get the right LW.

[0 th th 0]; th varying from 0.5 to 1 should have a LW going thru' 20nm.

Th=0.56 and 0.858 gives the required LW.

Pitch = 40 nm with 20nm lines. PW calculated based on <10% variation in linewidth. 4 spots/pitch used to create the pattern. Illumination is monopole with sigma = 0.6. The numerical aperture is 0.35 for 10nm spots and EUV illumination, leading to k1spot = 10/13.4*0.35 = 0.26. Since two spots are used to create the linewidth, k1 is 0.52. This is not aggressive on the density of pattern printed but serves as a good example to compare the various maskless designs with leading mask technology. From the exposure latitude – depth of focus comparison, it appears that the piston technologies are slightly better than att. PSM while att PSM and tilting mirrors are comparable.

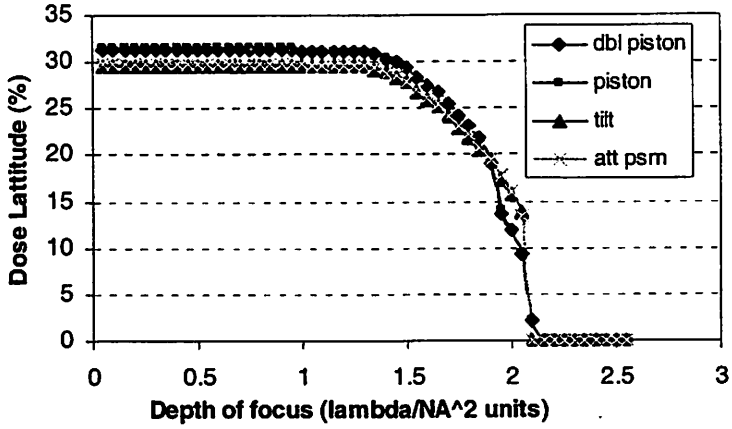

Figure 5-1: Process lattitude for a tight pitch case using monopole illumination (sigma = 0.6).

Optimized illumination

To image a one-dimensional pattern with pitch, P = $p*\lambda/NA$, the optimal off-axis point source is [8]:

$$J(f,g) = 0.5 * \{ \delta [(f-0.5*NA/\lambda * p, g) + \delta[(f+0.5*NA/\lambda * p, g)] \}$$

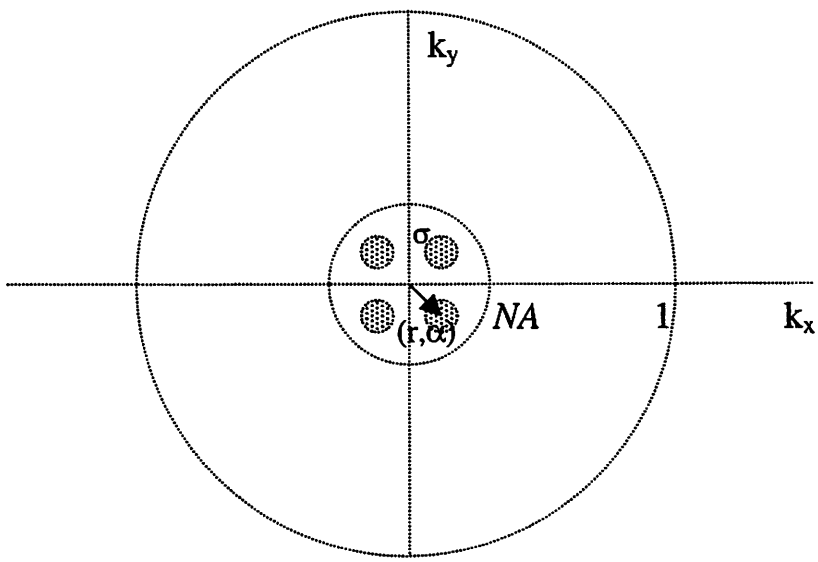

Figure 5-1: Propagating mode bounds in k-space. Outer circle is 2pi/lambda. Inner circle is the projection optic (size determined by *NA*). Quad illumination in the pupil plane set by (r,θ) for optimized printing for a given pitch.

The center of the poles is located at

$r = \lambda/(2*P*NA) = 0.5/p.$

Pitch optimized source condition:

Pitch, P = 44nm

NA: 0.3

Illumination wavelength, λ = 13.4nm

Illumination type: Dipole, σ = 0.125

Pole displacement radius (relative to the projection optic),

$$r = \frac{1}{2}\frac{\lambda}{P*NA} = \frac{1}{2}\cdot\frac{13.4}{40*0.35} = 0.625$$

Displacement angle, $\alpha = 45^{\circ}$

The tilting mirror pattern is generated using 4mirrors/pitch, each mirror representing a 10nm spot at the wafer plane. Two central mirrors are turned off, the precise analog position determined by *OPD* for which a 20nm linewidth at 0.3 intensity threshold is achieved at zero defocus. The attenuated phase-shift mask is 5% larger to allow a 20nm linewidth at focus and at the desired threshold. The choice of sigma_out (0.125) is reasonable, yet somewhat arbitrary. It does not have a direct bearing on the relationship we are attempting to show here.

The following figure compares the exposure latitude – depth of focus relationship for tilting mirror and attenuated phase-shift-mask (ATT-PSM) with a 6% chrome transmission. The process window is generated for less than 10% variation in the width of

the 20nm line. A nominal 10% dose latitude results in similar operating range of depth of focus for both cases.

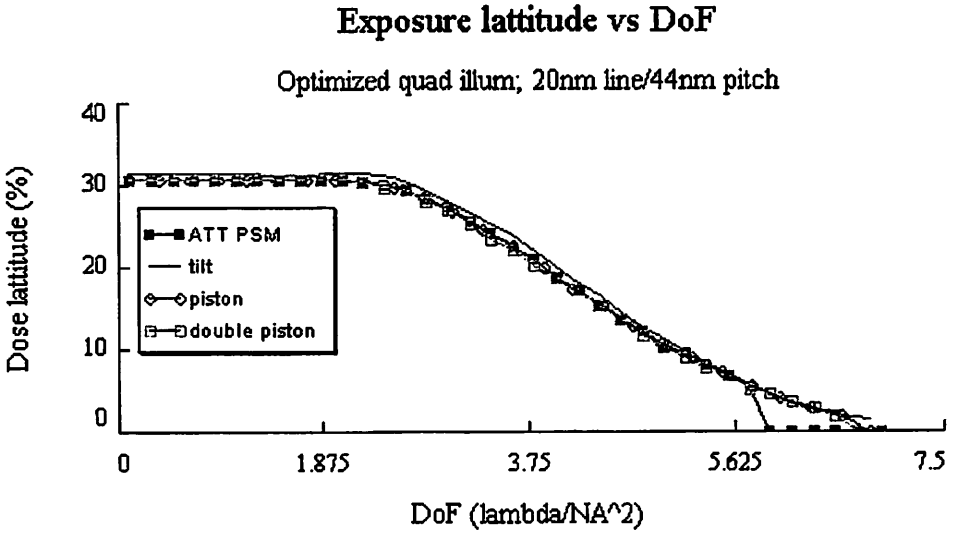

Figure 5-1: Exposure lattitude vs defocus of tight-pitch EUV example. Linewidth/pitch of 20/44nm printed using 11nm spots at *NA*=0.3 (k1=0.29).

This chart is given for pitch printed *on-grid*. A cumulative *across-grid* process-window is somewhat smaller.

In conclusion, it is easily seen that process window for mirror technologies are similar to or slightly better than conventional masks. Improvement in process latitude seen with pitch optimized illumination continues to play a significant role in the maskless world too.

5.6 Contacts

One of the four critical layers of lithography, contacts, are also the hardest features to print. In this section, we wish to print optimized contacts and provide a comparative summary of the printing capabilities of various technologies studied here. As with the previous cases, process window metric is used for comparison.

Significant issues are achieving contact scaling in sub-pixel units and across grid contact movement without loss of symmetry and with constant size.

Piston mirrors: A 2-D contact is generated by first creating a dark background of alternating on/off mirrors. Contacts are generated by removing 2 or more adjacent phase-edges.

The key question is: how do we size a contact in incremental units of CD/32, corresponding to 5 bits of positioning? Secondly, how do we take a nominally sized contact and move it across the grid (in horizontal, vertical, and diagonal directions) without, of course, altering its size? A final concern is related to defocus. We have seen in earlier examples of line-ends that defocus leads to image distortion because of uncompensated asymmetric mirror phase. Since very few mirrors are used to create minimally sized contacts, the edge effects leading to defocus dependence are significant for contacts. In a sense, printing low k1 contacts in a tight pitch is an ultimate test of a pixilated micromirror based imaging system.

We choose a central mirror and adjust the *OPD* of nearby mirrors in the following examples. Three modulation techniques are covered: overtilted mirrors, piston mirrors, and dual piston mirrors.

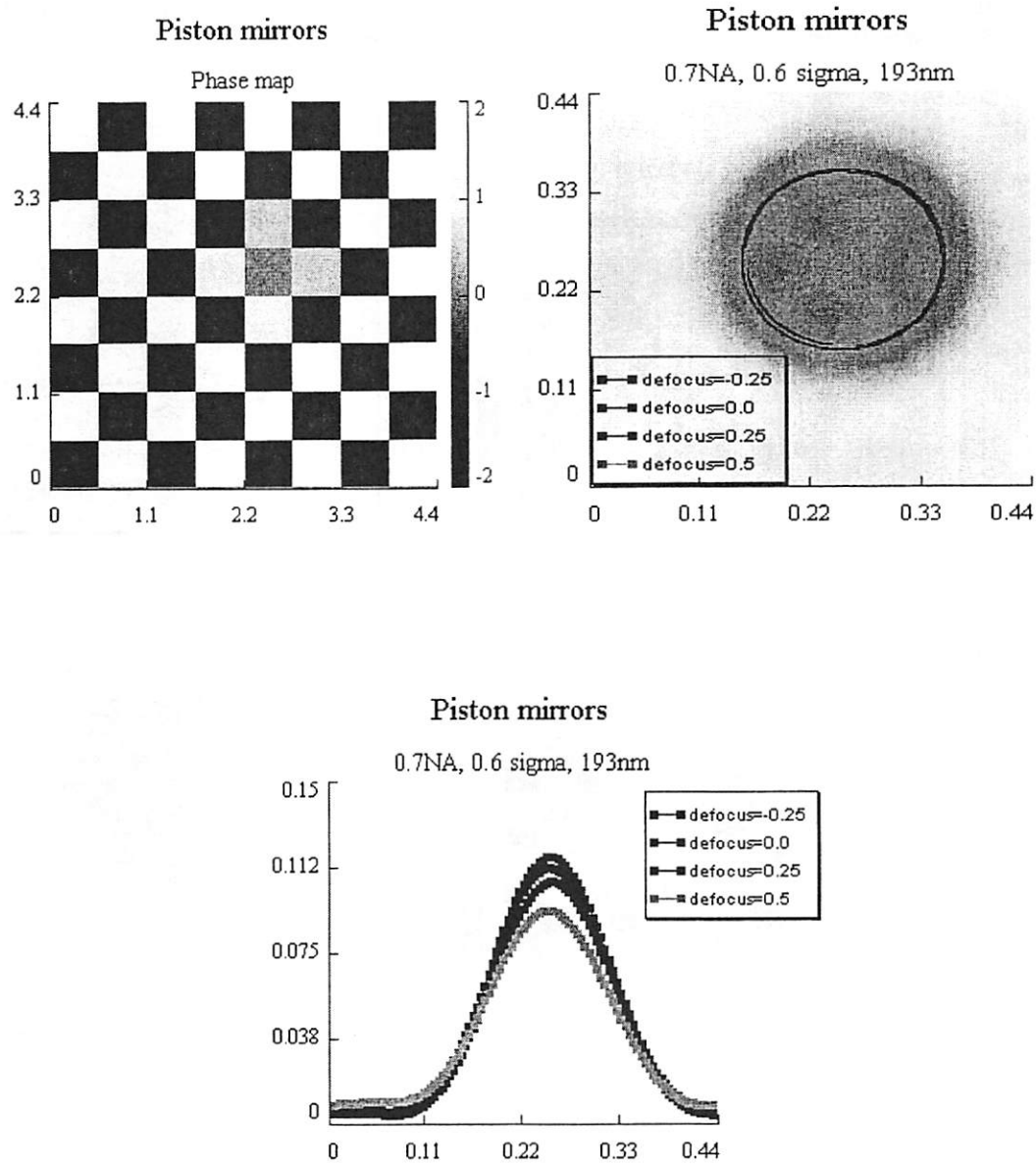

Figure 5-1: Printing a 100nm contact with piston mirrors (NA=0.7, sigma=0.6)

Figure 5-2: Phase maps, and image contours for an off-grid contact through focus composed with three mirror types. (a) Simple piston mirrors. (b) Tilt mirrors arranged in rows with alternating tilt directions. (c) Double piston mirrors operated as pseudo-tilt mirrors.

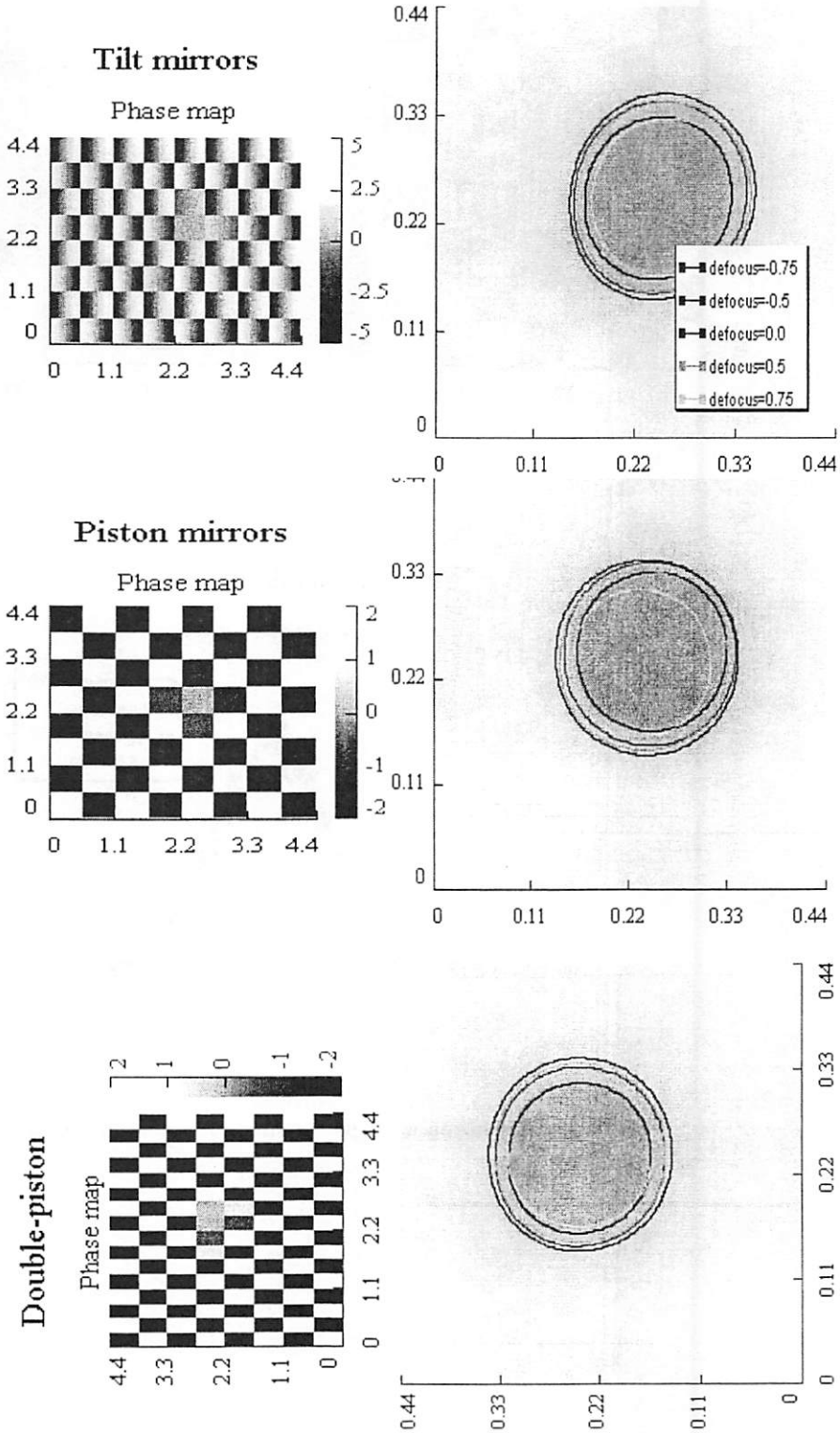

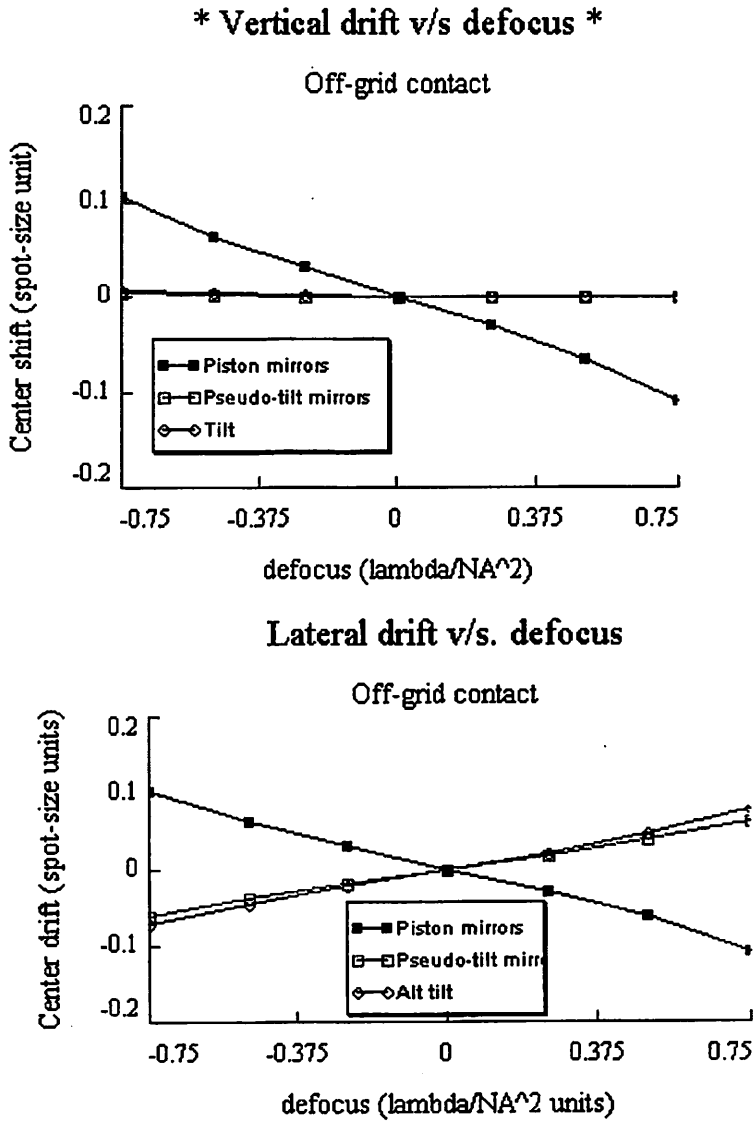

Figure 5-2: The drift of the contact center is plotted versus defocus.

In these figures, we show that the vertical and lateral drift of contacts due to defocus is best controlled with tilt mirrors. The dual-piston mirrors, which behave as tilting mirrors but are actually two piston halves accomplish both goals – they have the advantage of sharp phase drop of piston mirrors and the advantage of tilt in reduced defocus related

drift. The disadvantage, ofcourse, is that we need twice as many dual-piston mirrors than tilting mirrors.

5.7 Optical proximity correction (OPC) in conventional masks: Rule-based and model-based approaches

A partially coherent image is not linear in either amplitude or intensity. So there are fundamental differences in imaging isolated lines, spaces, contacts, and dense features. Mask biasing works well for 1-D features but the loss of high order terms leading to corner rounding for 2-D features requires a more complicated solution. If the optical degradation process is well understood, small features biases in the form of serifs can be inserted to account for the losses. There are three major components of OPC

a) Pattern dependent biases

b) Corner rounding

c) General loss of shape fidelity

These effects manifest in the form of line-end shortening, linewidth, and corner rounding. Image distortion in the form of linewidth variation can be due to proximity effect or due to nonlinearity. Proximity effect is variation in nominal linewidth due to environment while nonlinearity is variation in mask linewidth not reflected linearly in the printed image[1]. To counter these effects, the conventional arsenal consists of modifying the mask by using serifs and image size biasing. A major advantage with this approach is that it requires modification of only the mask, hence, it is a cost effective option.

[1] Nonlinearity is also represented in the Mask Error Enhancement Factor (MEEF) metric which progressively gets higher with shrinking CD.

Conventional mask biasing for simple shapes is accomplished with an iterative approach. Complex geometries require mainly two approaches: rules-based and model based correction. In a rule-based approach, the amount of correction applied to a feature or an edge of a feature is determined by a predefined table. On the other hand, model-based methods calculate the correction by mathematical models based on the pattern environment. Sometimes a combination of rule and model-based correction may be applied. For instance, model based OPC may not come up with a side-bar assist feature but a rule-based implementation can, so a subsequent model based method can be used to correctly size and place the assist feature.

5.8 Image optimization for maskless lithography

An algorithmic approach to pattern generation using micromirrors is needed to optimally arrange the position of each mirror in a large array. No CAD software designed especially for maskless lithography exists, and a number of algorithms still need to be developed to automate the design process. Micronics, a mask pattern generator company has shown [2-4] that mirrors can be calibrated using a test mask and adjusted for dose-focus effects. We would like to get an algorithmic approach to this problem. Simply using grayscaling values obtained by simultaneously tilting all mirrors across the 'on' to 'off' range may not provide the necessary data to correctly position a line edge since the interplay between adjacent mirrors needs to be considered. Image optimization is necessary to take advantage of dynamic pixel level control offered by the nanomirror array; however, it is also a challenging problem due to the large number of variables involved. Proximity effects, role of sigma (coherence), *NA*, number of spots per minimum feature are some of

the parameters that govern maskless based imaging and an optimization algorithm would need to account for these parameters.

The goal is to provide a tool that takes conventional mask layout and generates position of individual mirrors in a massive array. CAD tools coupled with numerical and aerial image simulators are employed to find optimal mirrors positions. Using a confluence of tools, such as *Cadence* (CAD layout software), MatLab, and the PanoramicTech aerial image simulator, we want to show that mirror positions can be optimized to create patterns with large process-window.

5.8.1 OPC algorithm

The OPC algorithm is based on multi-variable implementation of the Newton-Raphson method of convergence used for non-linear systems. The Newton-Raphson algorithm updates its solution estimate by using finite differences to build a matrix of partial derivatives. For instance, if we have 3 mirror tilts determining 3 edge locations, each step of the N-R algorithm requires building a 3x3 matrix containing partial derivatives of the discrepancies caused by finite differencing. Building the matrix requires 3 passes with each pass measuring the partial derivative of edge displacement due to perturbation of one mirror.

The Newton-Raphson algorithm will work only when the discrepancy vector varies smoothly in the neighborhood of the solution, and if the initial guess is close enough to the actual solution. In the vicinity of the root the method performs well, converging quadratically. To obtain the best guess of root, we simulate edge displacement due to gradual on->off modulation of an edge mirror.

Given an optical system, we first create a look-up table for a knife-edge pattern which is displaced by one spot by analog tilting of an edge mirror from a fully OFF to a fully ON position.

a) For each mirror position, measure the displacement of edge and store the 1-to-1 dependence in a look-up-table (LUT) that takes into consideration the optical system (*NA*, sigma, magnification). The generation of this table provides initial values for Newton-Raphson implementation.

b) Bitmap representation of layout is partitioned into spot units. Average of the ensemble bits comprising a spot gives us a grayscale value. Based on the layout, we have an initial 2-D representation of mirror position using the LUT. Transmission function is generated and aerial image simulated.

c) The layout is imported into the aerial image simulator scaled for comparison with the image generated by mirror array.

d) Mean difference across a spot between layout edge and 0.3 intensity threshold simulated edge is stored in an error matrix.

e) The error matrix is used to generate new *OPD* values for all mirrors according to the Newton-Raphson algorithm.

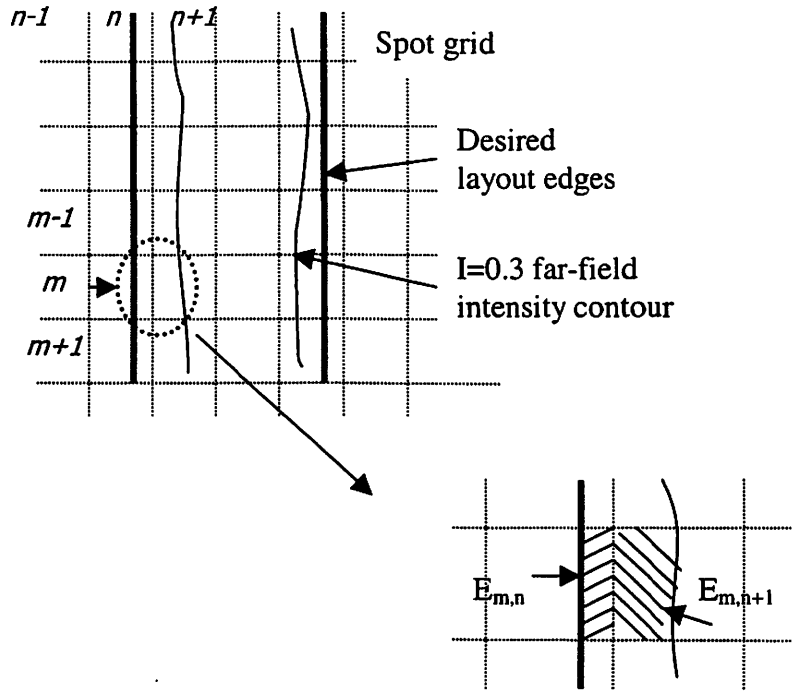

Figure 5-2: Error matrix, E, is a function of OPD of all the mirrors in the layout segment being optimized. If a layout edge or simulated image edge falls in a given spot, that spot has a non-zero error value.

Newton-Raphson is derived from Taylor expansion of a function in the neighborhood of a point.

$$f(x+\delta) \cong f(x) + f'(x)\delta + \frac{f''(x)}{2}\delta^2 + \ldots$$

The N-R algorithm takes a local estimate of the slope and projects to the root. If we require $f(x+\delta) = 0$ and use only the first two terms of the Taylor expansion series, we get

$$\delta = -\frac{f(x)}{f'(x)}$$

The new value for the independent variable is given as:

$$x_{n+1} = x_n - \frac{f(x_n)}{f'(x_n)}$$

If we have a multivariable problem where x is dependent on many dimension the following Jacobian matrix comes in useful. For our case, it specifically presents the relationship between the *OPD* of mirrors and edge displacements. For the case of two mirrors and two edges, we have:

$$J(\theta_1, \theta_2) = \begin{bmatrix} \frac{\partial E_1}{\partial \theta_1} & \frac{\partial E_1}{\partial \theta_2} \\ \frac{\partial E_2}{\partial \theta_1} & \frac{\partial E_2}{\partial \theta_2} \end{bmatrix}$$

The error matrix is stored by variables $E_n(\theta_1, \theta_2)$ and is used as follows to determine the next iterative values for the mirrors:

$$\begin{bmatrix} \theta_1' \\ \theta_2' \end{bmatrix} = \begin{bmatrix} \theta_1 \\ \theta_2 \end{bmatrix} - J(\theta_1, \theta_2)^{-1} * \begin{bmatrix} E_1(\theta_1, \theta_2) \\ E_2(\theta_1, \theta_2) \end{bmatrix}$$

We check for convergence after each iteration. We want to place the edges within ½ of least significant bit (LSB). For a 100nm CD and 5-bit grayscaling, the LSB corresponds to 3.125nm and placement error needs to be less than 1.56nm.

Other than N-R, there are several methods to help find roots of a polynomial given an initial guess. A simplest and slowest approach is to determine the root by trial and error – calculate the function at various points and look for a change in sign indicating a root. Convergence is slow as the error is halved in each step. In order to find complex roots of a function, Muller's method may come in handy [7]. It involves quadratic interpolation among three points instead of linear interpolation between two. The method finds

complex pairs of roots by solving for the zeros of the quadratic. N-R is a compromise between the speed of convergence (error decreases quadratically, as opposed to linearly with simple trial and error methods) and simplicity of implementation (compared to Muller's method, for instance). Also, it lends itself well for multidimensional solutions. The matrix inversion computation can potentially slow down the iterative calculations; however, the Jacobian in this case is mostly a diagonal matrix. The non-diagonal values representing the edge displacement due to minor perturbation in mirrors away from the edge are near zero. In the examples to follow, we start by solving a 2x2 matrix (2 mirror tilts, 2 edges). A large matrix involving 7 edges and 7 tilt variables is solved for the final example involving line-end and proximity effects. More complex geometries, with large number of mirror-edge dependencies can be solved faster with an automated approach.

Figure 5-2 shows an example of the method wherein a given layout is first represented by an approximate value of mirror positions to generate a first-pass aerial image that is iteratively refined to eventually approximate the desired pattern within a given tolerance.

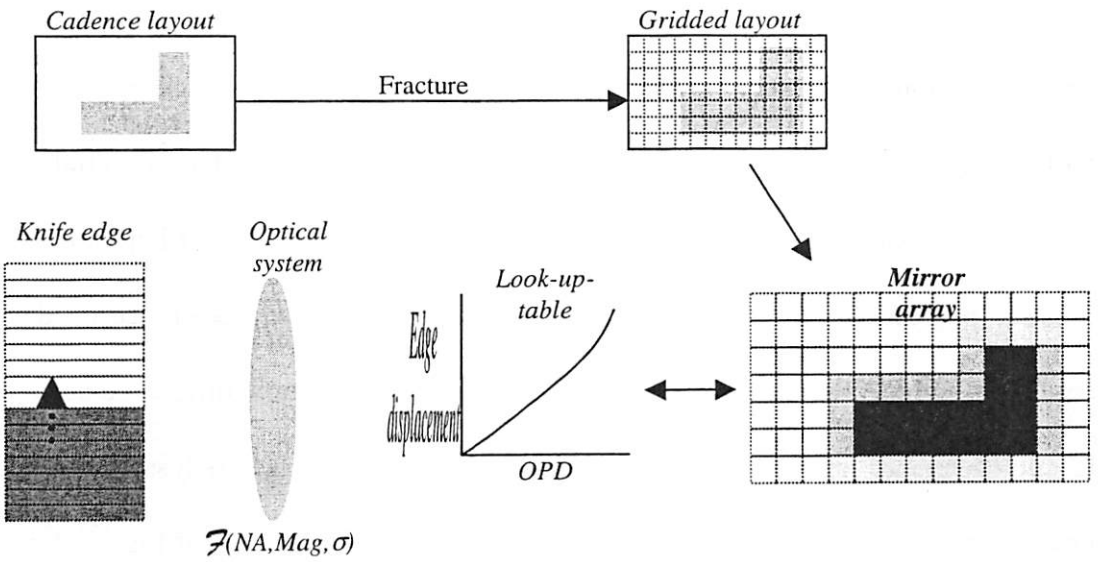

(a) Initial value generation (first guess of polynomial root).

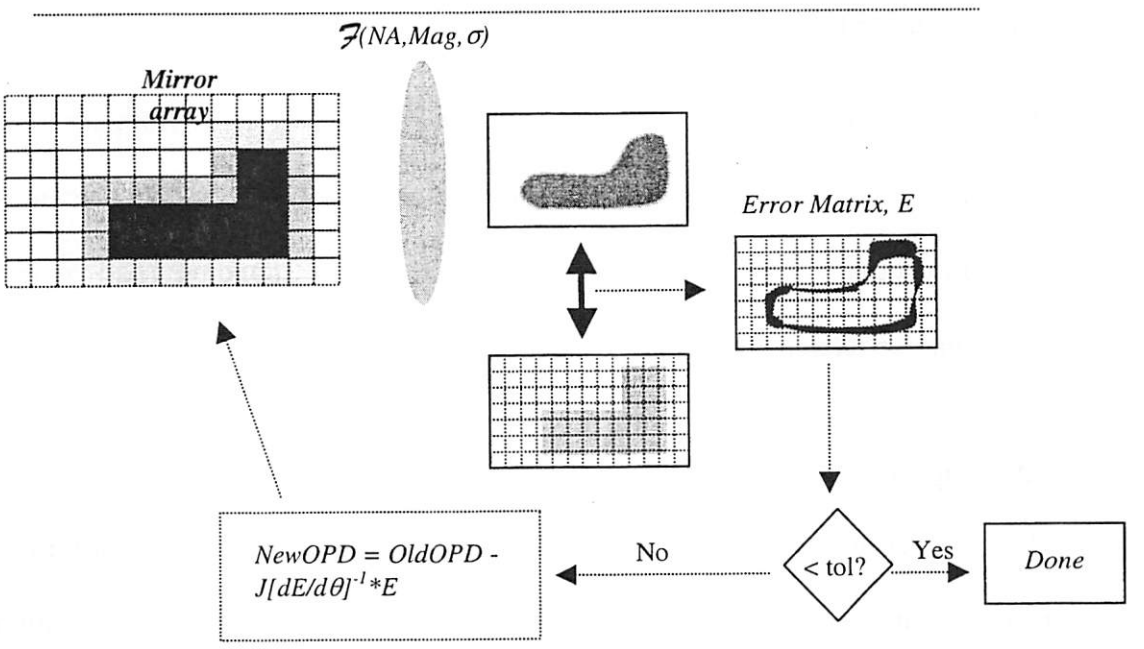

(b) Iterative loop to get optimized mirror array OPD.

Figure 5-2: Newton-Raphson algorithm implemented for maskless lithography pattern correction. A look-up-table gives initial guess values for mirror tilts.

5.8.2 Setting an Error minimization criteria

There are several questions that need to be answered before embarking on an implementation of the Newton-Raphson algorithm. It was stated that a knife-edge based look-up-table that takes into consideration the optical system is used as an initial guess of the unknown polynomial root. How close do we need to be to the root before halting the iterative process? In other words, we need to set the maximum tolerance on the error condition, E. For straight lines (edges), we choose to minimize the difference between the layout edge and simulated image 0.3 intensity threshold edge to less than ½ LSB[1]. Determining error conditions for a corner is tricky. Because of loss of high order terms, corner rounding is not avoidable. However, the degree to which we can "push" out the corner needs to be determined.

In the "line-end" and "poly-T" examples that follow, two spots from the line-end are chosen as "match-points" where the layout edge and aerial image edge difference needs to be less than tolerance. The routine ends when edges corresponding to all "match-points" are within the tolerance limits.

5.9 Optimization examples

Here we present results from the implementation of the optimization algorithm on several types of features. In general, larger patterns are decomposed to match a pre-built database. Using a combination of look-up table and Newton-Raphson method, we can find tilt mirror positions to generate aerial images and compare with the layout.

[1] Assuming 5-bit grayscaling, ½ LSB corresponds to 1/64 of minimum CD.

5.9.1 Minimum sized line

Here we implement 1-D features with off-grid edges. Two dark-line features with line widths, LW=3.24spots and LW=2.0 spots, are presented. We take this example because it is a simple case of two inputs and two output optimization. The inputs are tilt of mirrors on the left and right edges of the feature. The outputs are the difference in the left and right edge locations from the desired layout edges.

The next figure schematically shows the error variables in relation to the feature being sized.

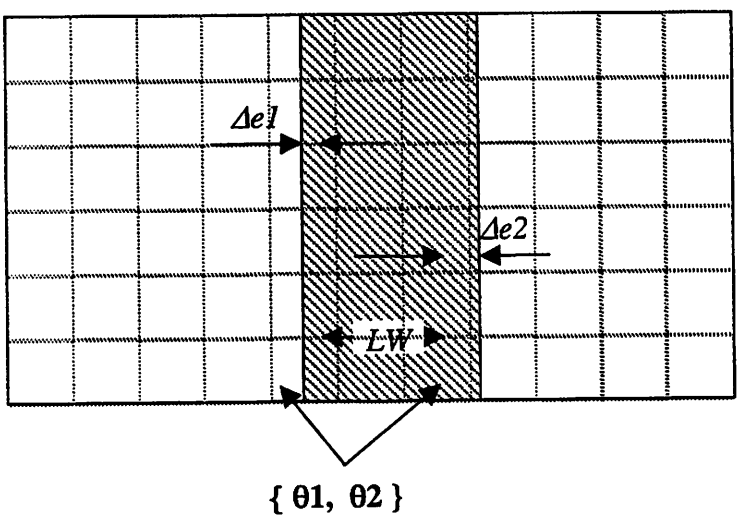

Figure 5-2: 1-D isolated feature placement.

For this example, the following values are used:

- Feature type: Isolated line
    - Target CD: 3.24, 2.48, and 2 spots
- $NA = 0.11$
    - k1spot = 0.2
    - $k_1 = 0.65, 0.4$
- $\lambda = 13.4$nm (EUV)
- Partial coherence: $\sigma = 0.6$

Figure 5-2 shows that the image edge placement can be brought within tolerance with few iterations for the simple cases.

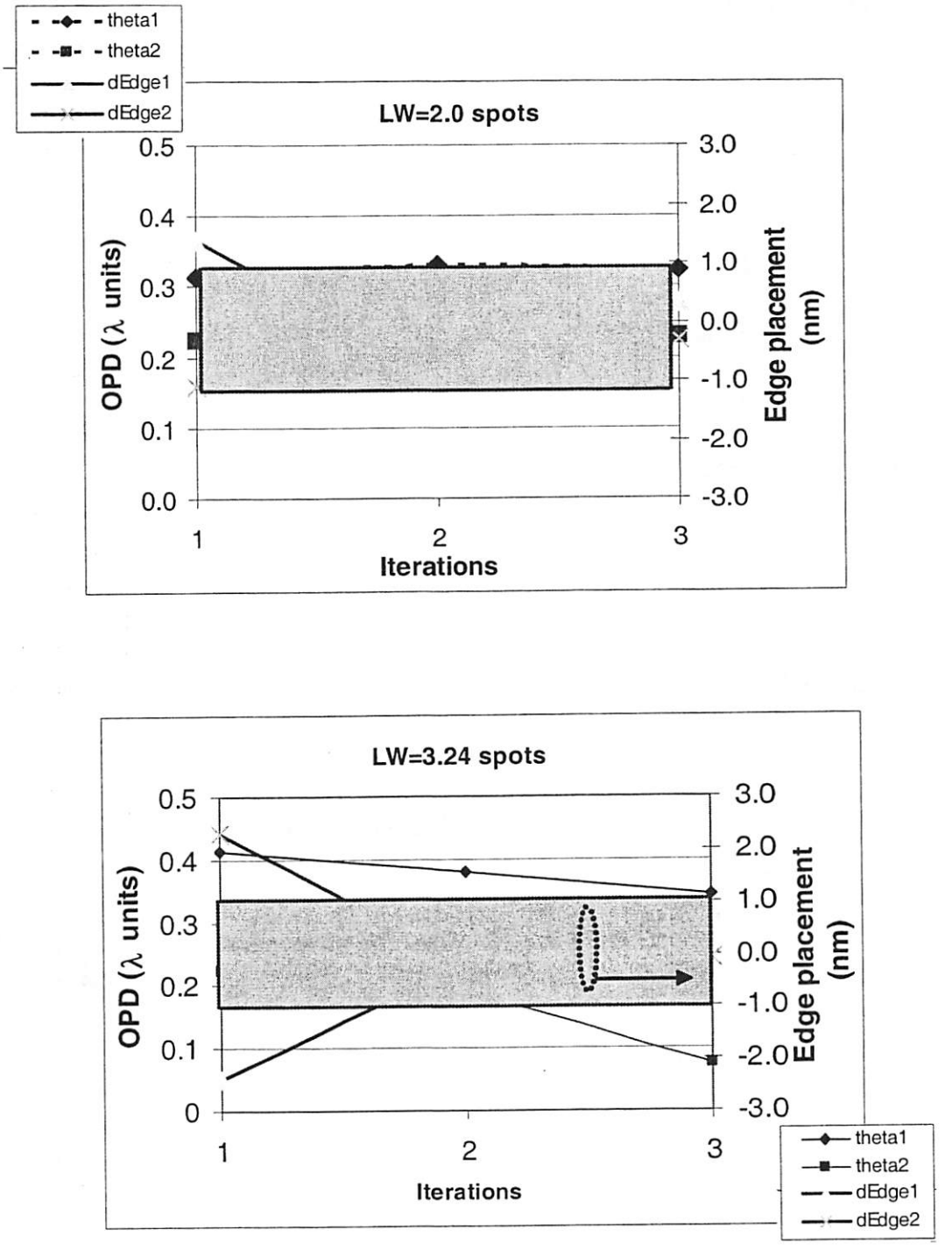

Figure 5-2: Optimization of the mirror tilts (measured as OPD) to bring the errors within bound. (a) LW = 2.0 spots (b)LW = 3.24 spots

5.9.2 OPC example 2: Line-end

- Feature type: Isolated line
    - Target CD: 2 spots (spot-size = 10nm)
    - Pitch: 8 spots
- $NA = 0.30$
    - $k_{1spot} = 0.22$
    - $k_1 = 0.45$
- Wavelength, $\lambda = 13.4$nm (EUV)
- Partial coherence: $\sigma = 0.6$

Line-end layout has high frequency terms which are filtered by the optic. We use three

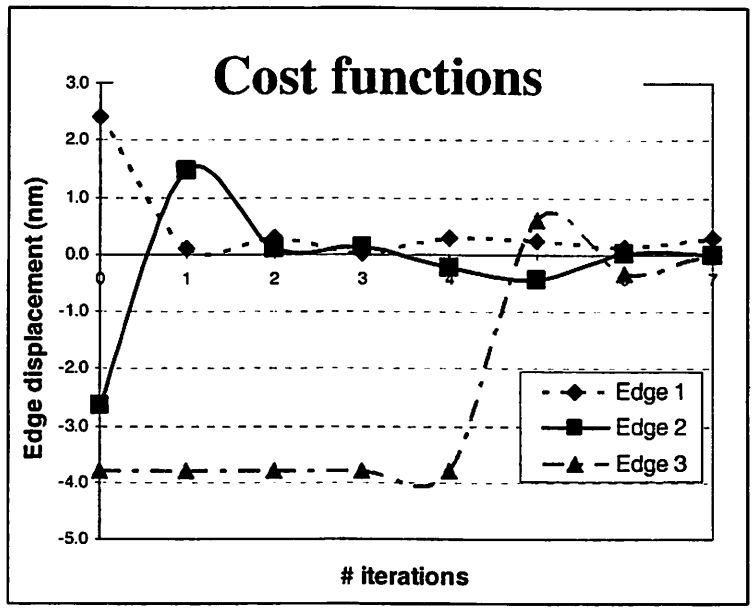

Figure 5-3: Deviation of three critical edges is lowered with successive iterations till tolerance bound is reached.

match-points (indicated in the next figure) which define the cost functions and input variables as follows:

dE1 = Eimage(P1) – Elayout(P1)

dE2 = Eimage(P2) – Elayout(P2)

dE3 = Eimage(P3) – Elayout(P3)

Variables: $\theta 1$ (at P1), $\theta 2$ (at P2), $\theta 3$ (at P3)

Using the vector form of Newton-Raphson described above, we get the following cost function.

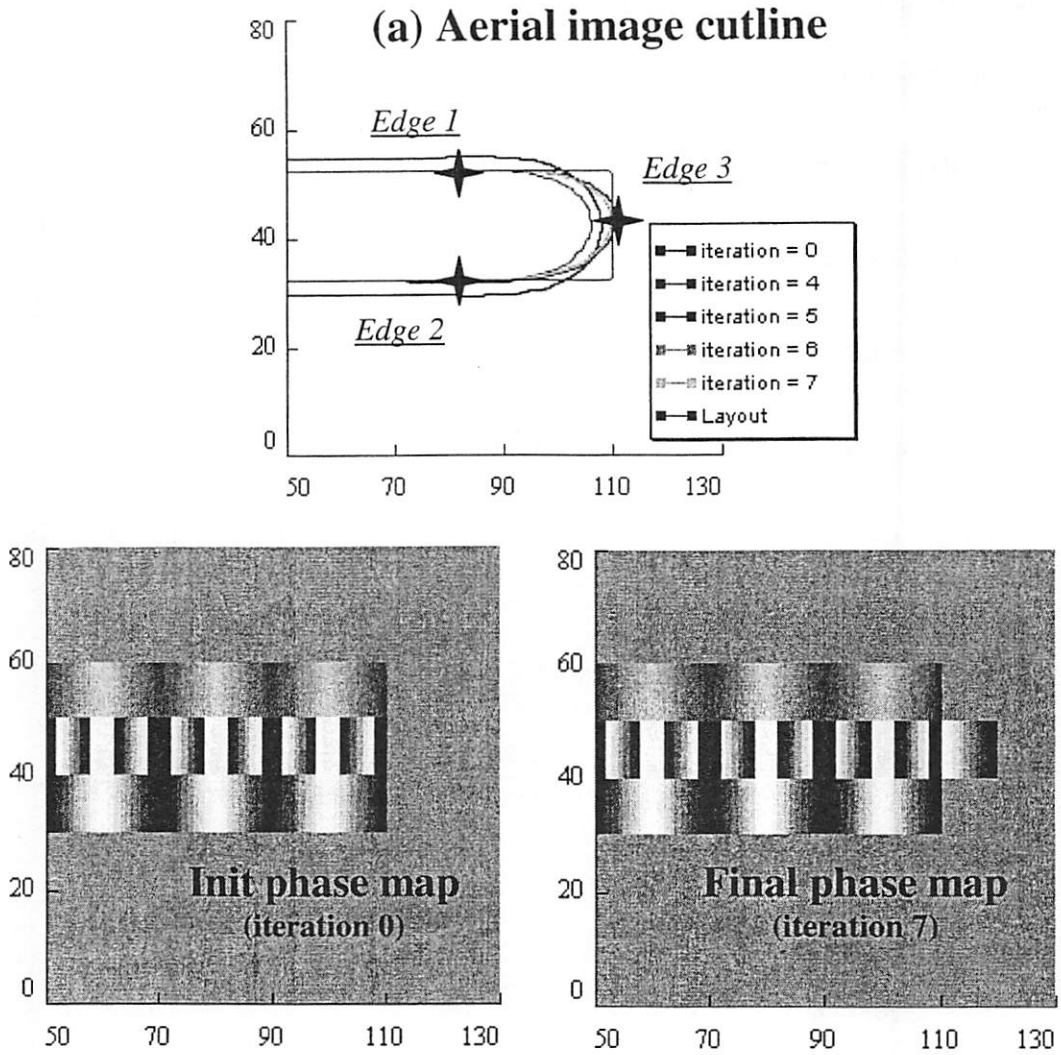

Figure 5-3: (a) Three match-points are chosen to determine the error conditions for a line-end feature. Image evolution through several iterations is shown in relation to the desired layout. (b) and (c) are the initial and final phase maps of the tilted mirror array.

5.9.3 Poly-T example

As a final example, we look at optimizing a line-end in the presence of proximity effects. The next figure shows two minimally sized lines (LW = 2spots) placed orthogonal to each other. The center of the vertical line bulges due to the tip of the horizontal line. The tip of the horizontal line recedes due to the vertical line. All points marked by 'X' in the next figure are the *match* points where the image and layout edges have to meet within 1nm tolerance.

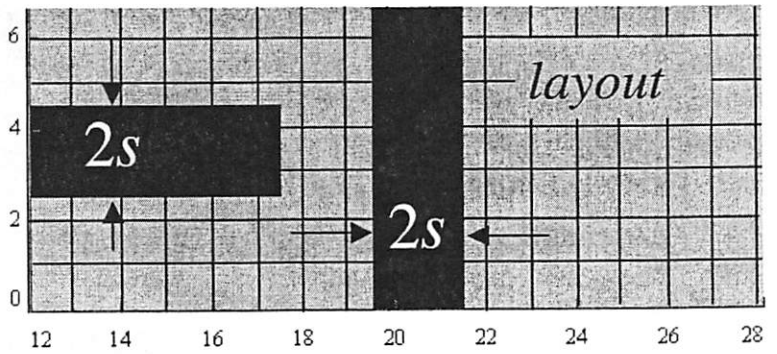

Figure 5-3: Poly-T feature layout with associated mirror grid

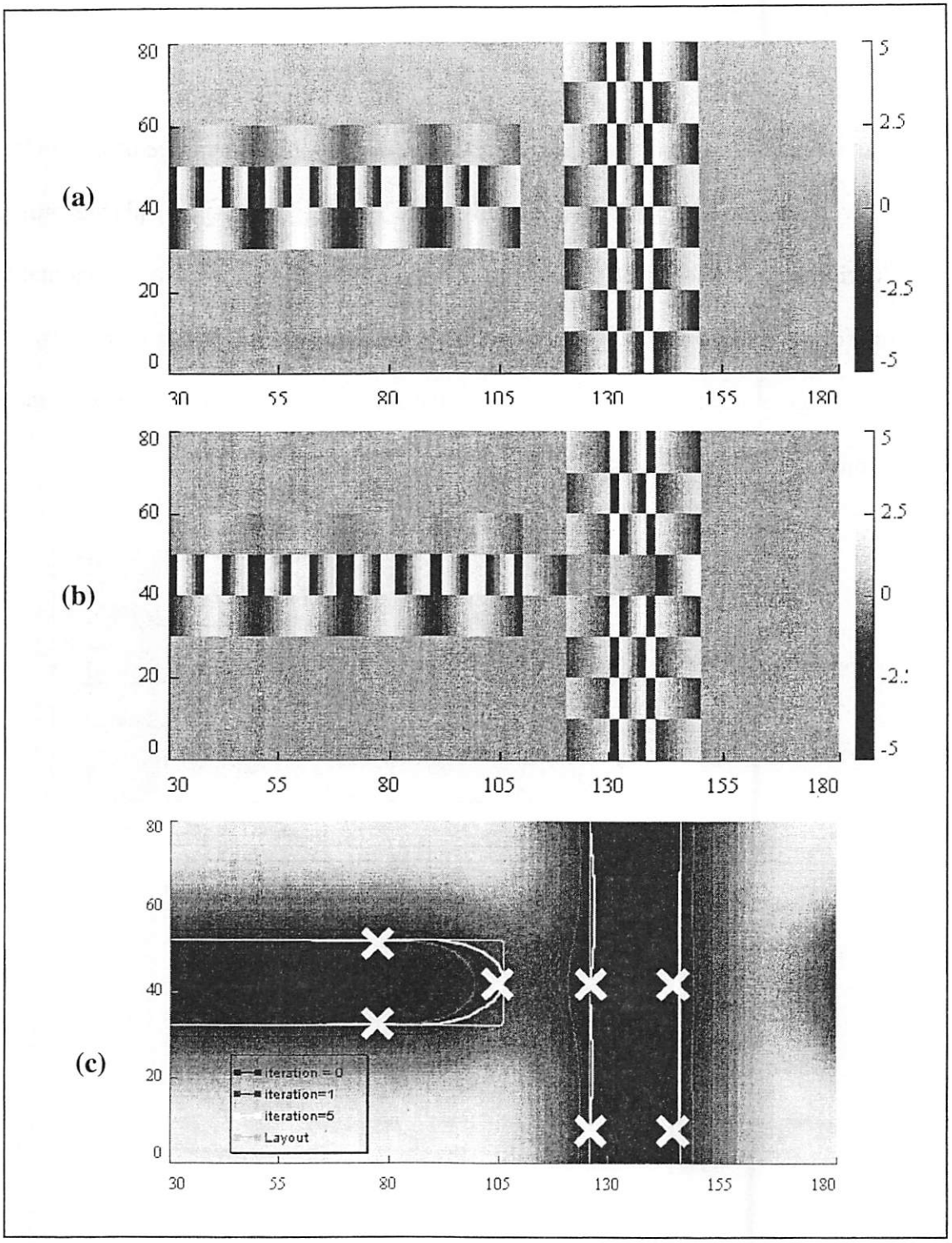

Figure 5-3: (a) Phase map of initial mirror tilt guess, (b) final phase map, (c) Aerial image of the poly-T feature with 0.3 threshold cutlines for various iterations and layout contour. The 'X's denote match-points where the edge displacement for the cost-function is measured.

5.10 Conclusion

In the composition of horizontal and vertical line patterns for integrated circuits, piston and tilt mirrors have generally equivalent performance, measured as the size of the exposure latitude versus defocus process window. But for some patterns, operation of tilt mirrors with overtilt has distinct advantages and produces higher contrast images with larger process windows. Piston mirror composition also suffers from a larger shift of image position with defocus for two-dimensional features such as contacts when printed off grid.

An image optimization routine is suggested which allows mirror based patterns to match the desired layout within set tolerances. It should be noted that while we used *NA*, sigma, and spot-size parameters for our demonstration examples, we can also take advantage of the dynamic pattern generation to incorporate parameters from an actual optical system with aberration values and resist related processing parameters.

5.11 References

[1]. Y. C. Pati, T. Kailath, "Phase-shifting masks for mirolithography: automated design and mask requirements," Journal of Optical Society of America A, vol. 11, no. 9, pp. 2438, 1994.

[2]. T. Sandstrom, T. Fillion, U. Ljungblad, M. Rosling, "*Sigma7100, a new architecture for laser pattern generators for 130 nm and beyond*", SPIE, vol. 4409, pp.270-6, 2001.

[3]. U. Ljungbald, T. Sandstrom, H. Buhre, P. Durr, H. Lakner, "*New architecture for laser pattern generators for 130nm and beyond*," 20th Annual BACUS sym. on Photomask Technology, SPIE vol. 4186, pp 16-21, 2001.

[4]. T. Sandstrom, N. Eriksson, "*Resolution extensions in the Sigma 7000 imaging pattern generator*", SPIE, vol.4889, pp.157-67, 2002.

[5]. Y. Shroff, Y. Chen, W. Oldham, "*Optical Analysis of Nanomirror based Pattern Generation*", SPIE vol. 5037, *Microlithography Conference,* Santa Clara, Feb. 28, 2003

[6]. Mikko Honkala, Ville Karanko, and Janne Roos,"*Improving the convergence of combined Newton-Raphson and Gauss-Newton multilevel iteration method*", in Proc. Intl. Symp. Circuits & Systems, ISCAS 2002, Scottsdale, AZ, USA, 2002.

[7]. Numerical Recipes in C: The art of scientific computing, pp347.

[8]. Alfred Wong, "Reticle Enhancement Techniques in optical lithography", SPIE press, pp. 84, 2000.

6 Conclusions

The motivation for maskless lithography has been the rising cost of mask sets. However, the fact that a nanomirror based direct-write system can provide a quick turn-around solution, especially in an initial circuit design phase is a significant advantage. In this thesis, the requirements of a maskless lithography are used to present top-down design of a practical system. An electronic light modulator with built-in DRAM and CMOS based logic is necessary to meet the throughput challenge. High speed digital to analog convertors for analog mirror modulation is necessary to meet the grayscale requirement. A flash architecture is necessary to account for the lack of a CW EUV light source.

A first order analysis of a flexure-hinge based parallel-plate nanomirror device is shown. We assume that bending occurs only in the hinge. We have decided to not use a hard-stop to avoid stiction related problems during operation. A mirror 1μm on an edge is required to tilt 6.7mrad for a full ON-OFF modulation. The gap is chosen to provide the necessary room for bending without causing snap-down. The designed mirror resonant frequency is 35Mrad/sec, but the operational frequency is limited by the EUV light source to 10kHz. We showed that a built-in resistor can be used for damping, however, to achieving near critical quality factor, a 40MΩ resistor is required.

Device specification for fabrication was changed to meet the tool capability of the EECS microlab. In lieu of 1sq. μm mirrors with 100nm flexure length, devices ranging in size from 3-5μm on an edge and 1μm flexure length were fabricated. The longer flexure

length was compensated by making it proportionately thicker to keep the spring stiffness constant. Because of low process temperature, we get non-conductive amorphous silicon. Conductive structural layers are obtained using Germane and diborane during deposition. Hence, the structural material is SiGe with <60% Ge while the sacrificial layer is fully Ge. A release process involving CO_2 based critical point drying is used. Electrical characterization of the mirrors remains to be completed.

Optical pattern generation methods have been explored using tilting and piston mirrors. Both designs allow analog modulation for grayscaling. Piston mirrors provide a sharp phase edge resulting in better NILS and larger process window. However, if overtilt is used, the tilting mirror process window is similar and in some cases (such as isolated lines) even better than piston mirrors. Both schemes compare favorably with attenuated phase-shift masks in use today.

Defocus related image drift was detected. Due to asymmetric wavefront reflected from off-grid printing by tilting and piston mirrors, the center of minimum sized features is seen to move. By electing to alternate mirror direction along rows and columns, drift in 1-D features is eliminated. Line-ends and especially contacts are prone to drift because the alternating mirror directions are not averaged out. Double-piston mirrors are introduced to mimic tilt mirrors, and also provide the sharp line slopes of piston mirrors. Overtilt of double-piston mirrors also gives us large process window.

An algorithm for image optimization is presented. We show that the aerial image generated by simple look-up of mirror grayscale values can deviate significantly from the design placement tolerance. The criteria for our iterative optimization algorithm involves

matching critical feature CD, edge-placement, line-end positioning, within a set tolerance. As demonstration of the algorithm, a poly-T layout with off-grid edge placement, proximity effects, minimally sized features, and line-end shortening is patterned within the set tolerance limits.

The image optimization routine has many applications, study of which can be the source of future work in this area. In the current work, only the NA and sigma of the imaging optic are utilized. We could also, in principle, embed specific stepper related information that can enable us to better "guess" the actual aerial image and, hence, have better mirror map. For instance, bundling aberration information in the mask image can be a potentially powerful tool in meeting the ever tightening tolerance requirements of lithography.

In this study, we have shown that mirrors meeting EUVL requirements can be fabricated at a low thermal budget. Future work in this area could involve integration of mirror arrays with memory and logic. Effect of fatigue in such a large cluster of mirrors bombarded with high energy radiation may also need to be studied.

Depending on continued industry interest in this area, maskless can take one of two routes. If high volume (>60WPH) maskless EUV lithography does not become a reality due to source limit, maskless lithography can be a serious contender for low throughput applications (~5WPH). At such volume, the cost of masks becomes prohibitive; with a dynamic pattern generator, maskless can provide an ideal solution for new chip design testing.

7 Appendix – A

7.1 Process Flow

The mirror structure is composed of $Si_{0.6}Ge_{0.4}$ and the sacrificial layer is Ge. The presence of <60% Ge in the structural layer prevents it from being etched in hot hydrogen peroxide used for Ge release. The presence of Ge makes the structural layer conductive. Therefore, we are able to have a low thermal budget mirror process.

STEP	PROCESS NAME	PROCESS SPECIFICATION	EQUIPMENT
1	Wafer	<100> Si wafers	
2	Isolation Oxide		
2.1	preclean	Piranha clean + 25:1 HF 20sec	sink9
2.2	initial oxidation	Low Thermal Oxide: 2500 A; 37' dep	Tylan8
3	Bottom electrode dep		
3.1	a-SiGe deposition	SiGeVar.019; 2-3kA 50GeH4, 100SiH4,60B2H6 @800mT, 450C for 50'	Tystar19
4	CMP		4" CMP
4.1	Wafer clean	5-7s 10:1 HF dip	sink9
4.2	Spin dry		Spindryer6
5	Mask1: POLY0 Litho		
5.1	Prime wafers	Recipe 1 on track	SVGcoat
5.2	PR coat		SVGcoat
5.3	Exposure	Bright field	GCA Wafer Stepper
5.4	120C,90s PEB,Develop		SVGdev
6	PolySi etch		
6.1	Polysilicon etch	Recipe 5003 – Chlorine based etch; End point detection (EPD) on dummy; ~30s	Lam4
6.2	Resist strip1	PRS3000 90C	Sink5
6.3	Resist strip2	Wafer dry	Spindryer3
6.4	Resist strip3	ASH	Technics-C
6.5	Piranha clean		
7	Germanium Dep		Tystar19
7.1	Wafer clean		
7.2	Ge deposition	Silicon nucleation layer required (450C,200Si2H6,300mT), (350C,88/0GeH4,600mT)	

8	Mask2: Trench litho			GCA WS
	8.1	Prime wafers	Recipe 1 on track	SVGcoat
	8.2	PR coat		SVGcoat
	8.3	Exposure		GCA WS
	8.4	120C,90s PEB,Develop		SVGdev
9	Germanium Etch			Lam5
	9.1	Ge etch	Recipe 5003; no EPD; ~20s	Lam5
	9.2	PR strip	ACETONE + 7' ash	Sink7/Tech-c
10	a-Si Deposition			Tystar19
	10.1	Wafer clean	No Piranha; just DI water clean	Sinks
	10.2	500A Si dep	no nucl nec; 450C; 100 Si2H6; 300mT, 15min?	
11	LTO deposition		*etch-stop layer*	Tystar11
	11.1	Wafer clean	(unless dep occurs right after hinge dep)	
	11.2	700A LTO dep	Std. undoped recipe	
12	Mask2: Trench litho		*Hinge to MIRR contact (dark field)*	GCA WS
13	LTO contact ETCH			LAM2
14	POLY dep (disilane)			Tystar19
15	Mask3: MIRROR Litho		*Pattern mirrors*	GCA WS
16	Mirror etch			Lam5
17	Mask 4: Hinge Litho			GCA WS
18	Poly etch		*Stop on LTO*	Lam5
19	Release			CPD2
	90 deg C H. Peroxide			